ADJOINT SENSITIVITY ANALYSIS OF TIME-DOMAIN RESPONSES EXPLOITING TIME-DOMAIN TRANSMISSION-LINE MODELING METHOD

By

PEIPEI ZHAO, B. ENG.

A Thesis
Submitted to the School of Graduate Studies
in Partial Fulfillment of the Requirements
for the Degree
Master of Applied Science

McMaster University

© Copyright by Peipei Zhao, April 2008

MASTER OF APPLIED SCIENCE (2008)
(Electrical and Computer Engineering)

McMaster University
Hamilton, Ontario

TITLE: **ADJOINT SENSITIVITY ANALYSIS OF TIME-DOMAIN RESPONSES EXPLOITING TIME-DOMAIN TRANSMISSION LINE MODELING METHOD**

AUTHOR: PEIPEI ZHAO
B. ENG.
(Electrical Engineering, McMaster University, Canada)

SUPERVISOR: Dr. Mohamed H. Bakr, Associate Professor
Department of Electrical and Computer Engineering
B. Sc. (Cario University, Egypt)
M. A. Sc. (Cario University, Egypt)
Ph. D. (McMaster University, Canada)
P. Eng. (Province of Ontario)

NUMBER OF PAGES xiii, 123

ABSTRACT

The traditional approach for estimating sensitivities utilizes finite difference (FD) approximations which are time-intensive even for simple problems. This involves perturbing each design parameter in the forward and/or backward directions and simulating the perturbed structures. For a problem with N optimizable parameters, this approach requires at least N+1 simulations. If N is large, this approach may easily become impractical due to the intensive simulation time.

The Adjoint Variable Method (AVM) aims at obtaining the response sensitivities using at most one extra simulation regardless of the number of designable parameters. The field information is stored at specific points related to each parameter in both the original and adjoint simulations. This approach was applied to sensitivity analysis of scalar objective functions and frequency domain responses.

This thesis addresses a new AVM algorithm for estimating time domain response sensitivities using time domain transmission-line modeling (TD-TLM) method. Our algorithm obtains the sensitivities of any electromagnetic time domain response over the whole simulation time with respect to all parameters using only one extra time domain simulation. A very good match is obtained between our sensitivity estimates and those obtained through the accurate and time-intensive central difference approximation.

One of the motivations for sensitivity analysis is gradient-based optimization. The optimization process speeds up by using our AVM algorithm for gradient estimation. In this literature, we will implement gradient-based optimization using our AVM through different applications including microwave imaging problem. The results show good match between the sensitivities obtained using our AVM approach and those obtained using the more expensive finite difference approximation.

ACKNOWLEDGMENTS

I would like to acknowledge to all who have contributed to my education at McMaster University. The person who I wish to express my greatest appreciation for is my supervisor, Dr. Mohamed Bakr. I really appreciate his expert supervision and constant understanding and support on both life and study through my Master program. I also wish to thank Dr. Natalia Nikolova for her helpful advice and constant encouragement.

I would like to express the appreciation to my colleagues Peter A. W. Basl, Xiaying Zhu, Yunpeng Song, Mohamed Swillam and everyone in the Computational Electromagnetics Laboratory and the Simulation Optimization Systems Research Laboratory of the Department of Electrical and Computer Engineering at McMaster University, for their useful comments and valuable discussions.

I wish to thank for the financial support provided by the Department of Electrical and Computer Engineering, McMaster University, for research assistantship and teaching assistantship. I also wish to thank all the staff members of the ECE Department for their assistance, especially, Cheryl Gies, Terry Greenlay, and Cosmin Coroiu.

Finally, special thanks to my family for their continuous understanding, encouragement and support.

CONTENTS

LIST OF FIGURES

LIST OF TABLES

CHAPTER 1

INTRODUCTION

1.1 MOTIVATION

The sensitivity analysis with respect to all designable parameters is essential in many problems such as gradient-based computer-aided design (CAD), inverse problems, tolerance analysis, and yield analysis. Traditional electromagnetic (EM) solvers, however, do not provide temporal or spacial sensitivity information. Classically, the sensitivities of the responses are computed using finite differences (FD). This involves perturbing each design parameter in the forward and/or backward directions and simulating the perturbed structures. For a problem with N optimizable parameters, this approach requires at least $N+1$ simulations. Utilizing the more accurate Central Finite Differences (CFD) required extra $2N$ simulations. This extensive simulation time calls for more efficient simulation approaches.

Recently, an Adjoint Variable Method (AVM) technique with time-domain transmission-line modeling (TLM) is developed to efficiently estimate the objective function sensitivities with respect to all designable parameters [1]-[10]. Regardless of the number of design parameters, the sensitivities with respect to all parameters are obtained using only two analyses of the original and adjoint systems. The AVM algorithm for 2-D time-domain TLM was first presented by Bakr *et al.* in [1] to compute the sensitivities with respect to dimensions of perfectly conducting discontinuities. The technique was then extended to compute the sensitivities of 2-D and 3-D dielectric discontinuities [2]-[4]. Several other techniques were developed in the past few years. Self-adjoint S-parameter sensitivity analysis algorithms for lossless homogeneous and nonhomogeneous TLM problems were developed in [5], [6]. The sensitivities of planar structures using first-order one-way wave equation boundaries were addressed in [7]. Recently, AVM for conformal TLM based on the rubber cell implementation is presented [8]. The sensitivities of the complete time response for 2-D and 3-D lossless homogeneous and lossy nonhomogeneous TLM problems were presented in [9], [10].

The AVM approach is not only limited to the time-domain TLM method but it was also applied to other numerical techniques such as the finite-element method (FEM) [11]-[16], the method of moments (MoM) [17]-[20], the finite-difference time-domain (FDTD) method [21]-[24], and the frequency-domain TLM (FDTLM) method [25]. This thesis mainly focuses on the recent developments and applications of the AVM algorithm for the time-domain TLM.

The target response represents the desired performance of the system. The physical dimensions and the material properties can be estimated using optimization techniques. In gradient-based optimization, the responses and the sensitivities are essential. Thus, the efficiency of the sensitivity analysis approach is crucial for the solution of typical gradient-based optimization problems such as microwave inverse problems.

The main contribution in this thesis is the development of novel adjoint based algorithm for estimating sensitivities of time-domain responses at any time step with respect to all designable parameters [9], [10]. The algorithm is achieved through modifying the objective function of the original AVM algorithm in [1]. The field information is stored at specific domains related to each parameter during the original and adjoint simulations. The equations expressing the original and the adjoint systems have different mathematical forms [10]. We illustrate the applications of the algorithm to microwave inverse problems such as breast cancer detection [9], [10].

1.2 CONTRIBUTIONS

The author contributed substantially to the following developments presented in this thesis:

1. Efficient estimation of sensitivities at specific time using AVM for 2-D TLM perfectly conducting discontinuities and dielectric discontinuities.
2. 2-D tumor detection using surrogate models and AVM.
3. 2-D tumor detection using direct optimization and AVM.
4. Efficient estimation of sensitivities at specific time using AVM for 3-D

TLM problems exploiting the symmetric condensed node.

1.3 Overview of the Thesis

The thesis has two major parts. The first part (chapters 2-3) provides the comprehensive reviews of previous research done in applying the AVM method. This research represents the base for the work reported in this thesis. The second part (chapters 4-5) presents the major contribution and examples.

Chapter 2 reviews the theory of the time-domain TLM method [26]-[30]. 2-D TLM technique is first discussed [26], [27]. We then explain the 3-D TLM technique with symmetric condensed nodes (SCN) [30]. For both approaches, we discuss how the variations of dielectric properties and lossy materials are modeled. The boundary modeling of the non-dispersive case and the dispersive case are briefly introduced.

Chapter 3 reviews up-to-date AVM algorithms for time-domain TLM. The AVM for the 2-D time-domain TLM is first discussed [1]-[3]. The sensitivity analysis for perfectly conducting discontinuities and dielectric discontinuities are demonstrated. The next section reviews the AVM for 3-D TLM with SCN [4]. The following few sections review further developments of the AVM, such as the self-adjont S-parameter sensitivity analysis for lossless homogeneous and nonhomogeneous TLM problems [5], [6], sensitivities of planar structures using first-order one-way wave equation boundaries [7], and AVM for conformal TLM based on the rubber cell implementation [8].

Chapter 4 discusses our novel AVM algorithm for estimating the sensitivities of time-domain responses with respect to all designable parameters [10]. The detailed mathematical derivations are presented. The approaches are illustrated through a number of examples.

In Chapter 5, the technique is applied for inverse problems. 2-D breast tumor detection using surrogate models is first demonstrated. In the next section, different structured 2-D breast tumor detection approaches are presented using direct optimization and AVM. In all these problems, the optimized parameters include dielectric properties, dimensions, and location.

Finally, we conclude with a summery of the research contributions and future work in Chapter 6.

REFERENCES

[1] M.H. Bakr and N.K. Nikolova, "An adjoint variable method for time-domain transmission-line modeling with fixed structured grids," *IEEE Trans. Microwave Theory Tech.*, vol. 52, NO. 2, pp554-559, Feb. 2004.

[2] M.H. Bakr and N.K. Nikolova, "An adjoint variable method for time-domain TLM with wide-band Johns matrix boundaries," *IEEE Transactions on Microwave Theory and Techniques*, vol. 52, pp. 678-685, 2004.

[3] P.A.W. Basl, M.H. Bakr, and N.K. Nikolova, "Efficient estimation of sensitivities in TLM with dielectric discontinuities," *IEEE Trans. Microwave Wireless Comp.*, vol. 15, pp.89-91, Feb. 2005.

[4] P.A.W. Basl, M.H. Bakr, and N.K. Nikolova, "An AVM technique for 3-D TLM with Symmetric Condensed Nodes," *IEEE Trans. Microwave Wireless Componnets letters.*, vol. 15, pp.618-620, 2005.

[5] M.H. Bakr, N.K. Nikolova, and P.A.W. Basl, "Self-adjoint S-parameter sensitivities for lossless homogeneous TLM problems,"*International Journal of Numerical Modelling: Electric Networks, Devices and Fields,* vol. 18, pp. 441-455, 2005.

[6] P.A.W. Basl, M.H. Bakr, and N.K. Nikolova, "The theory of self-adjoint S-parameter sensitivities for lossless nonhomogeneous TLM problems," *IEEE Transactions on Microwave Theory and Techniques*, 2006.

[7] P.A.W. Basl, M.H. Bakr, and N.K. Nikolova, "Time-domain sensitivity analysis of planar structures using first-order one-way wave equation boundaries," in *International Journal of Numerical Modelling: Electric Networks, Devices and Fields:* John Wiley and Sons Ltd, Chichester, West Sussex, PO 19 8SQ, United Kingdom, 2006.

[8] P.A.W. Basl, M.H. Bakr, and N.K. Nikolova, "Efficient TLM sensitivity analysis exploiting rubber cells," *Computational Electromagnetics Research Laboratory*, McMaster University., Canada, 2008.

[9] M.H. Bakr, P. Zhao, and N.K. Nikolova, "Microwave imaging exploiting adjoint based surrogate models," *ACES International Conference on Wireless Communications and Applied Computational Electromagnetics*, Niagara Falls, ON, Canada, 2008.

[10] M.H. Bakr, P. Zhao, and N.K. Nikolova, "Adjoint first order sensitivities of time domain responses and their applications in the solution of inverse problems," *IEEE Trans. AP*, submitted.

[11] P. Garcia and J.P. Webb, "Optimization of planar devices by the finite element method," *IEEE Trans. Microwave Theory Tech.*, vol. 38, pp. 48-53, Jan. 1990.

[12] H. Akel and J.P. Webb, "Design sensitivities for scattering-matrix calculation with tetrahedral edge elements," *IEEE Trans. Magn.*, vol. 36, pp. 1043-1046, July 2000.

[13] J.P. Webb, "Design sensitivities using high-order tetrahedral vector elements," *IEEE Trans. Magn.*, vol. 37, pp. 3600-3603, Sept. 2001.

[14] J.P. Webb, "Design sensitivity of frequency response in 3-D finite-element analysis of microwave devices," *IEEE Trans. Magn.*, vol. 38, pp. 1109-1112, Mar. 2002.

[15] M.M. Gavrilovic and J.P. Webb, "Accuracy control in the optimization of microwave devices by finite-element methods," *IEEE Trans. Microwave Theory Tech.*, vol. 55, pp. 1901-1911, Aug. 2002.

[16] Y.S. Chung, C. Cheon, I.H. Park, and S.Y. Hahn, "Optimal design method for microwave device using time domain method and design sensitivity analysis Part I: FETD case," *IEEE Trans. Magn.*, vol. 37, pp. 3289-3293, Sept. 2001.

[17] H. Lee and T. Itoh, "A systematic optimum design of waveguide-to-microstrip transition," *IEEE Trans. Microwave Theory Tech.*, vol. 45, pp. 803-809, May 1997.

[18] S. Amari, "Numerical cost of gradient computation within the method of moments and its reduction by means of a novel boundary-layer concept," *in IEEE MTT-S Int. Microwave Symp. Dig.*, vol. 3, pp. 1945-1948, 2001.

[19] N.K. Georgieva, S. Glavic, M.H. Bakr, and J.W. Bandler, "Feasible adjoint sensitivity technique for EM design optimization," *IEEE Trans. Microwave Theory Tech.*, vol. 50, pp. 2751-2758, Dec. 2002.

[20] A.S. Soliman, M.H. Bakr, and N.K. Nikolova, "An adjoint variable method for sensitivity calculations of multiport devices," *IEEE Trans. Microwave Theory Tech.*, vol. 52, no. 2, pp. 589-599, Feb. 2004.

[21] Y.S. Chung, C. Cheon, I. Park, and S. Hahn, "Optimal shape design of microwave device using FDTD and design sensitivity analysis," *IEEE Trans. Microwave Theory Tech.*, vol. 48, pp. 2289-2296, Dec. 2000.

[22] Y.S. Chung, C. Cheon, I. Park, and S. Hahn, "Optimal design method for microwave device using time domain method and design sensitivity analysis-Part II: FDTD case," *IEEE Trans. Magn.*, vol. 37, pp. 3255-3259, Sept. 2001.

[23] G. Shen, H.W.W. Tam, N.K. Nikolova, and M.H. Bakr, "Adjoint sensitivity technique for FDTD methods on structured grids," in *Proc. IEEE/URSI Int. Antennas Propagation Symp.*, Columbus, OH, pp. 746-749, June 2003.

[24] Y.S. Richard, N.K. Georgieva, and H.W. Tam, "Absorbing boundary conditions for adjoint problems in the design sensitivity analysis with the FDTD method," *IEEE Trans. Microwave Theory Tech.*, vol. 51, pp. 526-529, Feb. 2003.

[25] M.H. Bakr and N.K. Georgieva, "An adjoint variable method for frequency domain TLM problems with conducting boundaries," *IEEE Microwave and Wireless Components Lett.*, pp. 408-410, Sept. 2003.

[26] P.B. Johns and R.L. Beurle, "Numerical modeling of 2-dimensional scattering problems using a transmission line matrix," *Proceedings of IEE*, vol. 118, no. 9, pp. 1203-1208, Sept. 1971.

[27] W.J.R. Hoefer, "The transmission-line matrix method-theory and applications," *IEEE Trans. Microwave Theory Tech.*, vol. MTT-33, pp.882-893, Oct. 1985.

[28] W.J. Heofer, "The discrete time domain green's function or Johns' matrix- a new powerful concept in transmission line modeling (TLM),"*Int. Journal of Numerical Modeling: Electric Networks, Devices and Fields*, vol. 2, pp.215-225, Dec. 1989.

[29] E.G. Costache and W.J. Hoefer, "TLM modeling of dispersive wide-band absorbing boundaries with time domain diakoptics for S-parameter extraction," *IEEE Trans. Microwave Theory Tech.,*vol. 38, no. 4, pp.379-385, April 1990.

[30] P.B. Johns, "A symmetrical condensed node for the TLM method," *IEEE Trans. Microwaves Theory Tech.*, vol. 35, no. 4, pp. 370-377, April 1987.

CHAPTER 2

THE TRANSMISSION- LINE MODELING (TLM) METHOD

2.1 INTRODUCTION

The TLM method, which was initially proposed by P. B. Johns [1], is an efficient numerical technique for solving Electromagnetic (EM) problems. The EM fields are simulated by a network of transmission lines with a discretized model in both space and time. MEFiSTO-2D and MEFiSTO Nova [2] are two powerful EM field modeling softwares that utilize the time-domain TLM in 2-D and 3-D, respectively.

This chapter reviews the time-domain TLM method to model 2-D and 3-D electromagnetic problems in both homogeneous and nonhomogeneous structures [1], [3]-[6]. For 3-D TLM, the mostly commonly used structure, the symmetric condensed node SCN [4], is presented. Modeling of lossy materials and boundary conditions is also introduced for both 2-D and 3-D.

2.2 BASIC THEORY

The TLM method is a powerful numerical technique for solving EM problems. The main idea is to model the wave propagation in a discretized space-time framework. The computation domain is discretized into a network of transmission lines that are usually referred to as "link-lines". The intersections of the link-lines are the TLM nodes. The structure of each node and its parameters are chosen based on the local material properties and the modeled EM phenomena. The voltages and currents on the link-lines are used to calculate the different EM field components at the center of the node. In TLM, a sequence of scattering and connection is steps carried out [1]. The desired excitation is usually added as a soft source to designated link-lines of the excited nodes. The excited incident impulses are partially reflected and partially transmitted. The scattered impulses then become the incident impulses on the neighbouring nodes at the next time step. The boundary conditions are applied if the scattered impulses have interface with the external boundaries.

For the i^{th} node, the scattering relation is given by

$$\boldsymbol{V}_{k+1}^{R,\,i} = \boldsymbol{S}^{i}\boldsymbol{V}_{k}^{i} \tag{2.1}$$

where $\boldsymbol{V}_{k}^{i}$ is the vector of incident impulses on the i^{th} node at the k^{th} time step, $\boldsymbol{V}_{k+1}^{R,\,i}$ is the vector of reflected impulses of the i^{th} node at the next time step, and $\boldsymbol{S}^{i}$ is the scattering matrix of the i^{th} node. The scattering matrices are different in 2-D TLM and 3-D TLM. The reflected impulses from each node become incident on neighbouring nodes. It follows that for the case of non dispersive boundaries [3], one TLM step is given by

$$\boldsymbol{V}_{k+1} = \boldsymbol{CSV}_k + \boldsymbol{V}_k^s \tag{2.2}$$

where $\boldsymbol{V}_k$ is the vector of incident impulses for all nodes at the k^{th} time step. In most problems, the initial conditions are all zeros ($\boldsymbol{V}_{k=0} = \boldsymbol{0}$). This means that the incident impulses on all link-lines are initially set to zero. The computational domain is discretized into a total of N nodes with node size Δl. The matrix $\boldsymbol{S}$ is a block diagonal matrix whose i^{th} diagonal block is $\boldsymbol{S}^i$. $\boldsymbol{C}$ is the connection matrix describing how reflected impulses connect to neighbouring nodes/boundaries. The vector $\boldsymbol{V}_k^s$ is the vector of source excitation at the k^{th} time step.

The connection matrix is a symmetric matrix with the following properties:

$$C_{ij} = \begin{cases} 1 = C_{ji}, & \text{if link } i \text{ is connected to link } j,\ i \neq j \\ \tau, & \text{if link } i \text{ is connected to a non dispersive boundary, } i = j \\ 0, & \text{otherwise} \end{cases} \tag{2.3}$$

where τ is the boundary impulse reflection coefficient for non dispersive boundaries, for examples, $\tau = 1$ for magnetic boundaries and $\tau = -1$ for electric boundaries.

2.3 TWO-DIMENSIONAL TLM METHOD

Many electromagectic problems can be solved using the 2-D TLM method. The 2-D problems are more suited for numerical computations compared to 3-D TLM in terms of simulation time and memory storage. For the TLM node, there are two types of discretization nodes, the series and shunt nodes. The 2-D shunt node is utilized more often because it is used to model the dominant mode in waveguide problems.

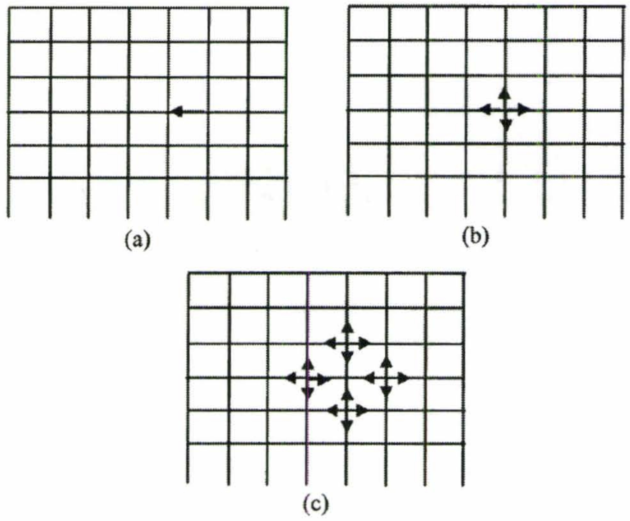

Figure 2.1: Illustration of the scattering and connection steps in a 2-D TLM algorithm. (a) An impulse is incident on the i^{th} node at a given time step. (b) The incident impulse is scattered into four reflected impulses. (c) The reflected impulses propagate to neighboring nodes where they get scattered at the next time step [9].

Figure 2.1 shows an illustration of the scattering and connection steps in a 2-D TLM algorithm. The impulse propagation on link-lines at the first and second iterations is illustrated. The scattering matrices of homogeneous and non homogeneous mediums are different. In the next two sections, the modeling of homogeneous lossless materials and non homogeneous lossy materials are discussed separately.

2.3.1 Modeling of Homogeneous Lossless Materials

An equivalent structure of a shunt node in a lossless and homogenous medium is shown in Figure 2.2. The parameter Δl is the length of each transmission line segment, L is the inductance per unit length, and C is the capacitance per unit length. We utilize basic

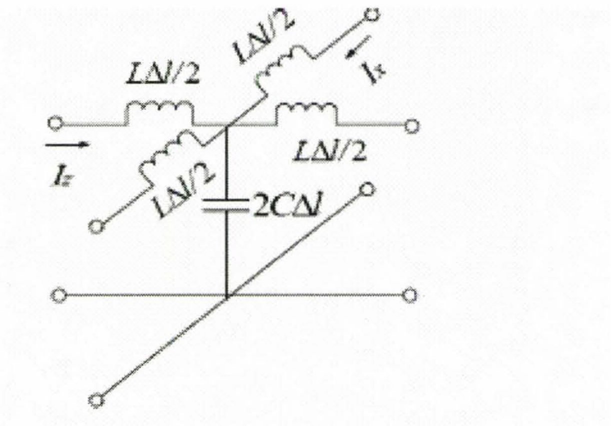

Figure 2.2: A 2-D shunt node structure of Lumped-element model where L is the inductance per unit length and C is the capacitance per unit length..

circuit analysis to obtain an expression for the voltages and currents over the transmission lines. Using KVL and KCL, we have [8]

$$\begin{cases} V_y(x+\Delta x) = V_y(x) - L\Delta x \dfrac{\partial I_x}{\partial t} \\ V_y(z+\Delta z) = V_y(z) - L\Delta z \dfrac{\partial I_z}{\partial t} \\ I_z(z) + I_x(x) = I_z(z+\Delta z) + I_x(x+\Delta x) + 2C\Delta l \dfrac{\partial V_y}{\partial t} \end{cases} \Rightarrow \frac{\partial^2 V_y}{\partial x^2} + \frac{\partial^2 V_y}{\partial z^2} = 2LC \frac{\partial^2 V_y}{\partial t^2} \tag{2.4}$$

Maxwell's equations is reduced to the following set for TM-modes [8],

$$\begin{aligned} \frac{\partial E_y}{\partial x} &= -\mu \frac{\partial H_z}{\partial t} \\ \frac{\partial E_y}{\partial z} &= \mu \frac{\partial H_x}{\partial t} \\ \frac{\partial H_x}{\partial z} - \frac{\partial H_z}{\partial x} &= \varepsilon \frac{\partial E_y}{\partial t} \end{aligned} \tag{2.5}$$

The following equation (2.6) is obtained if we combine the equations in (2.5)

$$\frac{\partial^2 E_y}{\partial x^2} + \frac{\partial^2 E_y}{\partial z^2} = \mu\varepsilon \frac{\partial^2 E_y}{\partial t^2} \tag{2.6}$$

where ε and μ are the local permittivity and permeability, respectively. We can thus establish a 1-to-1 mapping between circuit and field quantities [8],

$$E_y \leftrightarrow V_y, H_z \leftrightarrow I_x, H_x \leftrightarrow -I_z, \mu \leftrightarrow L, \varepsilon \leftrightarrow 2C. \tag{2.7}$$

Now, the voltage at any node can be obtained using the incident impulses.

$$\begin{aligned} V_y &= \frac{V_1^i + V_2^i + V_3^i + V_4^i}{2}, \\ I_x &= \frac{V_2^i - V_4^i}{Z_{TL}}, \\ I_z &= \frac{V_3^i - V_1^i}{Z_{TL}}. \end{aligned} \tag{2.8}$$

where Z_{TL} is the characteristic impedance of each line. Combining with the mapping given above, the electric field is given by

$$E_y = \frac{V_y}{\Delta l} = \frac{V_1^i + V_2^i + V_3^i + V_4^i}{2\Delta l} \tag{2.9}$$

The scattering matrix for this node is given by [3]

$$\boldsymbol{S} = 0.5 \begin{bmatrix} -1 & 1 & 1 & 1 \\ 1 & -1 & 1 & 1 \\ 1 & 1 & -1 & 1 \\ 1 & 1 & 1 & -1 \end{bmatrix} \tag{2.10}$$

The incident voltages of neighbouring nodes at the next time step are obtained from the connection process:

$$\begin{aligned} {}_{k+1}V_1^i(x,y) &= {}_kV_3^r(x,y-1), \\ {}_{k+1}V_2^i(x,y) &= {}_kV_4^r(x-1,y), \\ {}_{k+1}V_3^i(x,y) &= {}_kV_1^r(x,y+1), \\ {}_{k+1}V_4^i(x,y) &= {}_kV_2^r(x+1,y). \end{aligned} \tag{2.11}$$

For boundary nodes, the algorithm in (2.11) should be modified to model different boundary conditions.

2.3.2 Modeling of Non Homogeneous Lossy Materials

For a non homogeneous media, extra capacitance in the form of open-ended shunt stubs is necessary to model the extra permittivity. Synchronism of incident impulses is maintained by choosing the length of the capacitive stub to be equal to $\Delta l/2$ [8]. The losses can be modeled by matched loss shunt stubs. The capacitive and loss stubs have normalized admittance y_0 and g_0, respectively. In this case, the following 1-to-1 mapping between the field components and the transmission line quantities is given by [8]

$$\begin{aligned} &E_y \leftrightarrow V_y, H_z \leftrightarrow I_x, H_x \leftrightarrow -I_z, \\ &\mu \leftrightarrow L, \varepsilon \leftrightarrow 2C(1+\frac{y_0}{4}), \sigma \leftrightarrow \frac{g_0\sqrt{C/L}}{\Delta l} \end{aligned} \tag{2.12}$$

Free space is usually taken as the background medium for nonhomogeneous medium modeling. It follows that we have

$$L = \mu_0, C = \frac{\varepsilon_0}{2} \tag{2.13}$$

Combining (2.12) and (2.13), we get

$$\begin{aligned} y_0 &= 4.0(\varepsilon_r - 1) \\ g_0 &= \frac{\Delta l \sigma}{\sqrt{C/L}} \end{aligned} \tag{2.14}$$

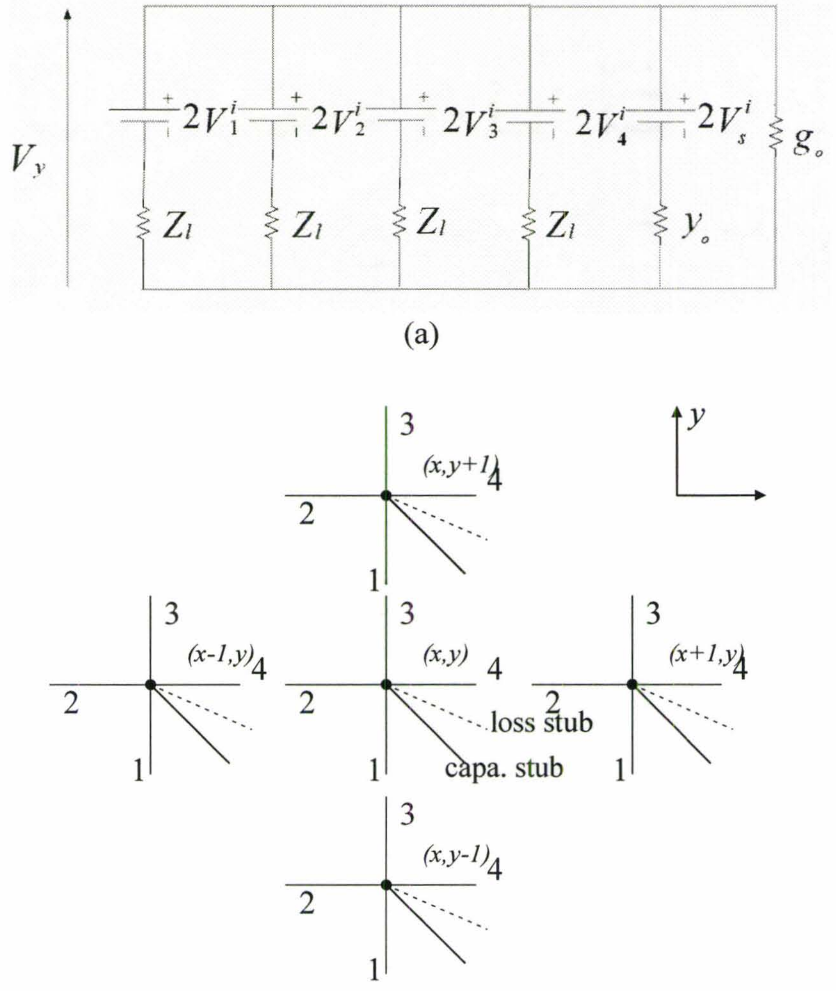

(a)

(b)

Figure 2.3: A 2-D shunt node with capacitive and loss stubs (a)Thevenin equivalent circuit. (b) Connection in 2-D shunt nodes.

Figure 2.3(a) illustrates the equivalent circuit of the 2-D shunt node in a nonhomogeneous lossy media. In this case, the electric field is given by

$$E_y = \frac{2(V_1^i + V_2^i + V_3^i + V_4^i + y_o V_s^i)}{y} \tag{2.15}$$

where $y = 4 + y_0 + g_0$. The scattering matrix of the lossy shunt node with both a capacitance stub and a loss stub is thus given by [3]

$$S = \frac{1}{y}\begin{bmatrix} 2-y & 2 & 2 & 2 & 2y_o \\ 2 & 2-y & 2 & 2 & 2y_o \\ 2 & 2 & 2-y & 2 & 2y_o \\ 2 & 2 & 2 & 2-y & 2y_o \\ 2 & 2 & 2 & 2 & 2y_o - y \end{bmatrix}. \tag{2.16}$$

The connection process of four impulses is exactly the same as it in the homogeneous case. The difference is the connection of the stubs (Figure 2.3(b)). The incident voltage of the open-ended capacitive stub at the k+1th time step is equal to its reflected voltage at the kth time step. For the loss stub, the energy is simply extracted from the domain and no incident impulses appear on this loss stub. It follows that we have the following connection steps:

$$\begin{aligned} {}_{k+1}V_1^i(x,y) &= {}_kV_3^r(x,y-1), \\ {}_{k+1}V_2^i(x,y) &= {}_kV_4^r(x-1,y), \\ {}_{k+1}V_3^i(x,y) &= {}_kV_1^r(x,y+1), \\ {}_{k+1}V_4^i(x,y) &= {}_kV_2^r(x+1,y), \\ {}_{k+1}V_s^i(x,y) &= {}_kV_s^r(x,y). \end{aligned} \tag{2.17}$$

For the boundary nodes, the steps in (2.17) should be modified properly to model different boundary conditions.

2.4 THREE-DIMENSIONAL TLM METHOD

Many practical electromagnetic problems are three-dimensional. Therefore, the 3-D TLM is thus essential for general 3-D problems. In this section, the symmetrical

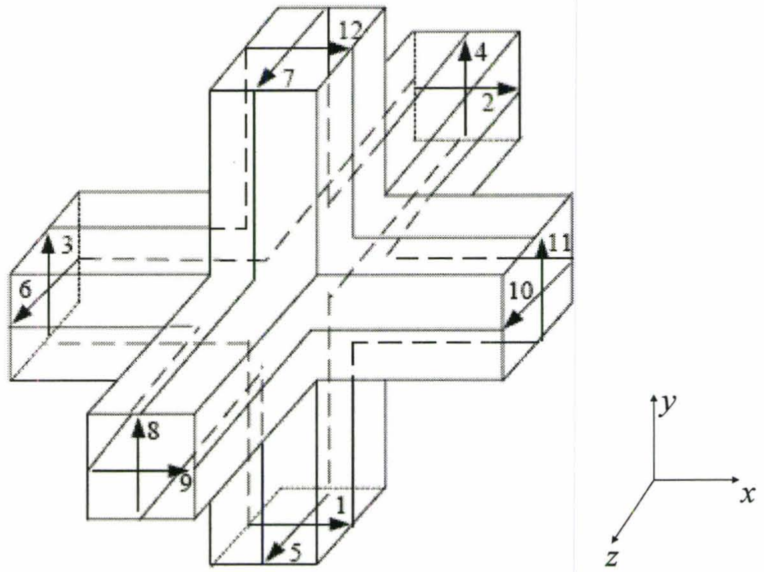

Figure 2.4: The three-dimensional symmetrical condensed node (SCN).

condensed node (SCN), which was initially proposed by Johns [4], is discussed. It is the most commonly used structure for TLM simulation because of its simplicity. It also enjoys the property that all field components are modeled at the node center. More advanced algorithms based on the SCN have been developed, including hybrid SCN and the generalized SCN [9]-[13].

The SCN has six branches with two transmission lines in each branch (Figure 2.4). Each transmission line has a length of $\Delta l/2$ and a characteristic impedance Z_0. The scattering properties are obtained from conservation of energy and charge [4]. The following mapping between the circuit and field components is utilized [8]:

$$\begin{aligned}&E_x \leftrightarrow -V_x, E_y \leftrightarrow -V_y, E_z \leftrightarrow -V_z,\\&H_x \leftrightarrow I_x, H_y \leftrightarrow I_y, H_z \leftrightarrow I_z.\end{aligned} \tag{2.18}$$

The 3-D TLM analyses of homogeneous and nonhomogeneous media are different. In the next two sections, the 3-D modeling of homogeneous lossless materials and nonhomogeneous lossy materials are discussed separately.

2.4.1 Modeling of Homogeneous Lossless Materials

For a homogeneous lossless medium, the scattering matrix has twelve rows and twelve columns. Only few of the matrix components are non-zero. The components of the scattering matrix are derived by applying the unitary conditions [4]. The conditions exploit the energy and charge conservation principals. In this case, we have [4]

$$\boldsymbol{S}^T \boldsymbol{S} = \boldsymbol{I} \tag{2.19}$$

$$\boldsymbol{S} = 0.5\begin{bmatrix}
0 & 1 & 1 & 0 & 0 & 0 & 0 & 0 & 1 & 0 & -1 & 0 \\
1 & 0 & 0 & 0 & 0 & 1 & 0 & 0 & 0 & -1 & 0 & 1 \\
1 & 0 & 0 & 1 & 0 & 0 & 0 & 1 & 0 & 0 & 0 & -1 \\
0 & 0 & 1 & 0 & 1 & 0 & -1 & 0 & 0 & 0 & 1 & 0 \\
0 & 0 & 0 & 1 & 0 & 1 & 0 & -1 & 0 & 1 & 0 & 0 \\
0 & 1 & 0 & 0 & 1 & 0 & 1 & 0 & -1 & 0 & 0 & 0 \\
0 & 0 & 0 & -1 & 0 & 1 & 0 & 1 & 0 & 1 & 0 & 0 \\
0 & 0 & 1 & 0 & -1 & 0 & 1 & 0 & 0 & 0 & 1 & 0 \\
1 & 0 & 0 & 0 & 0 & -1 & 0 & 0 & 0 & 1 & 0 & 1 \\
0 & -1 & 0 & 0 & 1 & 0 & 1 & 0 & 1 & 0 & 0 & 0 \\
-1 & 0 & 0 & 1 & 0 & 0 & 0 & 1 & 0 & 0 & 0 & 1 \\
0 & 1 & -1 & 0 & 0 & 0 & 0 & 0 & 1 & 0 & 1 & 0
\end{bmatrix}. \tag{2.20}$$

The incident voltages of neighbouring nodes at the next time step are obtained from the connection process. Here, the reflected impulses are exchanged between the neighbouring nodes (Figure 2.5):

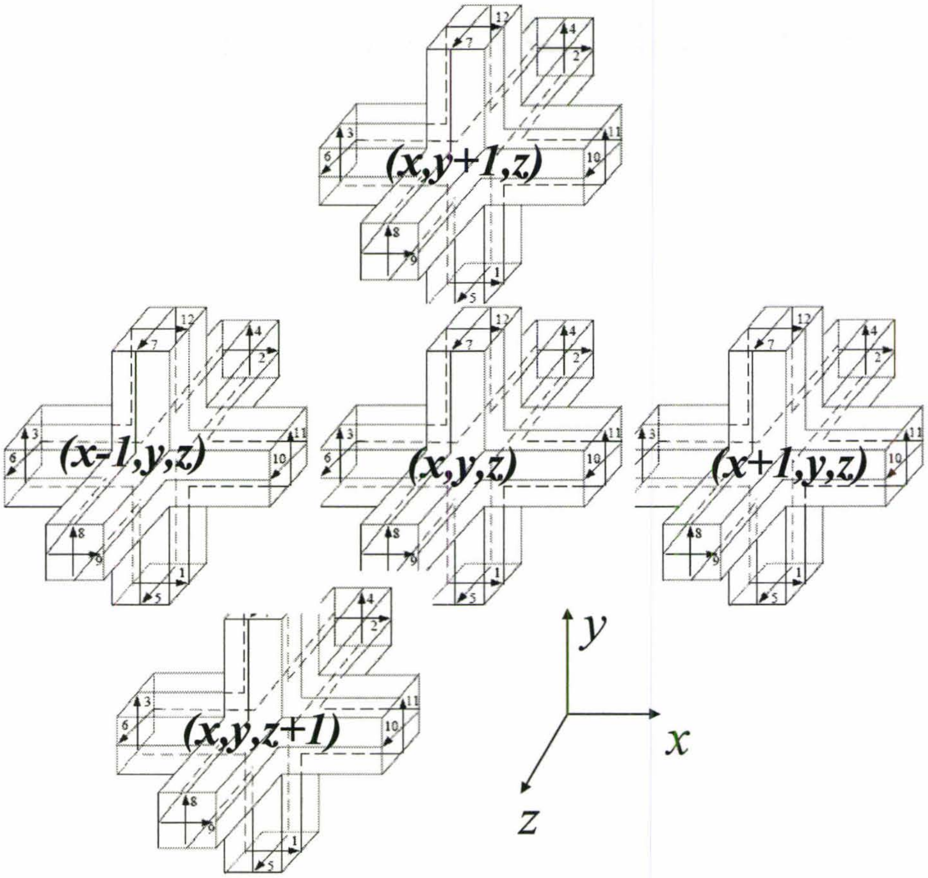

Figure 2.5: Connection of SCN nodes.

$$\begin{aligned}
{}_{k+1}V_1^i(x,y,z) &= {}_kV_{12}^r(x,y-1,z),\\
{}_{k+1}V_5^i(x,y,z) &= {}_kV_7^r(x,y-1,z),\\
{}_{k+1}V_4^i(x,y,z) &= {}_kV_8^r(x,y,z-1),\\
{}_{k+1}V_2^i(x,y,z) &= {}_kV_9^r(x,y,z-1),\\
{}_{k+1}V_8^i(x,y,z) &= {}_kV_4^r(x,y,z+1),\\
{}_{k+1}V_9^i(x,y,z) &= {}_kV_2^r(x,y,z+1),\\
{}_{k+1}V_{12}^i(x,y,z) &= {}_kV_1^r(x,y+1,z),\\
{}_{k+1}V_7^i(x,y,z) &= {}_kV_5^r(x,y+1,z),\\
{}_{k+1}V_3^i(x,y,z) &= {}_kV_{11}^r(x-1,y,z),\\
{}_{k+1}V_6^i(x,y,z) &= {}_kV_{10}^r(x-1,y,z),\\
{}_{k+1}V_{10}^i(x,y,z) &= {}_kV_6^r(x+1,y,z),\\
{}_{k+1}V_{11}^i(x,y,z) &= {}_kV_3^r(x+1,y,z).
\end{aligned} \tag{2.21}$$

For the boundary nodes, the equation (2.21) is modified to model different boundary conditions.

All the electromagnetic field components are obtained at any point using the values of the incident voltage impulses. The field components may be calculated as follows [4]

$$\begin{aligned}
E_x &= -\frac{V_1^i + V_2^i + V_9^i + V_{12}^i}{2\Delta l},\\
E_y &= -\frac{V_3^i + V_4^i + V_{11}^i + V_8^i}{2\Delta l},\\
E_z &= -\frac{V_5^i + V_6^i + V_7^i + V_{10}^i}{2\Delta l},\\
H_x &= \frac{V_4^i + V_7^i - V_5^i - V_8^i}{2Z_o\Delta l},\\
H_y &= \frac{-V_2^i + V_6^i + V_9^i - V_{10}^i}{2Z_o\Delta l},\\
H_z &= \frac{V_1^i - V_3^i + V_{11}^i - V_{12}^i}{2Z_o\Delta l}.
\end{aligned} \tag{2.22}$$

where Z_0 is the characteristic impedance.

2.4.2 Modeling of Non Homogeneous Lossy Materials

In a non homogeneous medium, a host TLM mesh is employed to model a background medium. Free space is usually taken as this background medium. Extra stubs are added to model the extra permittivity, permeability, and conductivity. Three open-circuit stubs are used for a material with relative permittivity greater than one. Three short-circuit stubs are also added to model permeability values greater than that of air. The scattering matrix has eighteen rows and eighteen columns [4]:

$$\boldsymbol{S}=\begin{bmatrix}
a & b & d & 0 & 0 & 0 & 0 & 0 & b & 0 & -d & c & g & 0 & 0 & 0 & 0 & i \\
b & a & 0 & 0 & 0 & d & 0 & 0 & c & -d & 0 & b & g & 0 & 0 & 0 & -i & 0 \\
d & 0 & a & b & 0 & 0 & 0 & b & 0 & 0 & c & -d & 0 & g & 0 & 0 & 0 & -i \\
0 & 0 & b & a & d & 0 & -d & c & 0 & 0 & b & 0 & 0 & g & 0 & i & 0 & 0 \\
0 & 0 & 0 & d & a & b & c & -d & 0 & b & 0 & 0 & 0 & 0 & g & -i & 0 & 0 \\
0 & d & 0 & 0 & b & a & b & 0 & -d & c & 0 & 0 & 0 & 0 & g & 0 & i & 0 \\
0 & 0 & 0 & -d & c & b & a & d & 0 & b & 0 & 0 & 0 & 0 & g & i & 0 & 0 \\
0 & 0 & b & c & -d & 0 & d & a & 0 & 0 & b & 0 & 0 & g & 0 & -i & 0 & 0 \\
b & c & 0 & 0 & 0 & -d & 0 & 0 & a & d & 0 & b & g & 0 & 0 & 0 & i & 0 \\
0 & -d & 0 & 0 & b & c & b & 0 & d & a & 0 & 0 & 0 & 0 & g & 0 & -i & 0 \\
-d & 0 & c & b & 0 & 0 & 0 & b & 0 & 0 & a & d & 0 & g & 0 & 0 & 0 & i \\
c & b & -d & 0 & 0 & 0 & 0 & 0 & b & 0 & d & a & g & 0 & 0 & 0 & 0 & -i \\
e & e & 0 & 0 & 0 & 0 & 0 & 0 & e & 0 & 0 & e & h & 0 & 0 & 0 & 0 & 0 \\
0 & 0 & e & e & 0 & 0 & 0 & e & 0 & 0 & e & 0 & 0 & h & 0 & 0 & 0 & 0 \\
0 & 0 & 0 & 0 & e & e & e & 0 & 0 & e & 0 & 0 & 0 & 0 & h & 0 & 0 & 0 \\
0 & 0 & 0 & f & -f & 0 & f & -f & 0 & 0 & 0 & 0 & 0 & 0 & 0 & j & 0 & 0 \\
0 & -f & 0 & 0 & 0 & f & 0 & 0 & f & -f & 0 & 0 & 0 & 0 & 0 & 0 & j & 0 \\
f & 0 & -f & 0 & 0 & 0 & 0 & 0 & 0 & 0 & f & -f & 0 & 0 & 0 & 0 & 0 & j
\end{bmatrix}. \tag{2.23}$$

Each element of the scattering matrix is expressed in terms of the normalized characteristic impedances of the capacitive stubs $\hat{Y}$ and the inductive stubs $\hat{Z}$.

$$
\begin{aligned}
& a=\frac{-\hat{Y}}{2(4+\hat{Y})}+\frac{\hat{Z}}{2(4+\hat{Z})}, && \hat{Y}_x=\frac{2\varepsilon_r}{u_0\Delta t}\frac{\Delta y\Delta z}{\Delta x}-4, \\
& b=\frac{4}{2(4+\hat{Y})}, && \hat{Y}_y=\frac{2\varepsilon_r}{u_0\Delta t}\frac{\Delta x\Delta z}{\Delta y}-4, \\
& c=\frac{-\hat{Y}}{2(4+\hat{Y})}-\frac{\hat{Z}}{2(4+\hat{Z})}, && \hat{Y}_z=\frac{2\varepsilon_r}{u_0\Delta t}\frac{\Delta x\Delta y}{\Delta z}-4, \\
& d=\frac{4}{2(4+\hat{Z})}, && \hat{Z}_x=\frac{2\mu_r}{u_0\Delta t}\frac{\Delta y\Delta z}{\Delta x}-4, \\
& e=b, && \hat{Z}_y=\frac{2\mu_r}{u_0\Delta t}\frac{\Delta x\Delta z}{\Delta y}-4, \\
& f=\hat{Z}d, && \hat{Z}_z=\frac{2\mu_r}{u_0\Delta t}\frac{\Delta x\Delta y}{\Delta z}-4, \\
& g=\hat{Y}b, && u_0=\frac{1}{\sqrt{\mu_o\varepsilon_o}}. \\
& h=\frac{\hat{Y}-4}{\hat{Y}+4}, && \\
& i=d, && \\
& j=\frac{4-\hat{Z}}{4+\hat{Z}}. &&
\end{aligned}
\tag{2.24}
$$

For lossy materials, six more stubs are included to model electric and magnetic losses in all directions. The structure of scattering matrix is the same as (2.23), but the elements are modified. Each element is expressed not only in terms of $\hat{Y}$ and $\hat{Z}$ but also in terms of the normalized admittances $\hat{G}$ and the normalized impedances $\hat{R}$ of the loss stubs. Assuming that $\Delta x=\Delta y=\Delta z=\Delta l$, we have [4]

$$
\begin{aligned}
& a=-\frac{\hat{Y}+\hat{G}}{2(4+\hat{Y}+\hat{G})}+\frac{\hat{Z}+\hat{R}}{2(4+\hat{Z}+\hat{R})}, && \hat{G}_x=\sigma_{ex}\frac{\Delta l}{Y_0}, \\
& b=\frac{4}{2(4+\hat{Y}+\hat{G})}, && \hat{G}_y=\sigma_{ey}\frac{\Delta l}{Y_0}, \\
& c=-\frac{\hat{Y}+\hat{G}}{2(4+\hat{Y}+\hat{G})}-\frac{\hat{Z}+\hat{R}}{2(4+\hat{Z}+\hat{R})}, && \hat{G}_z=\sigma_{ez}\frac{\Delta l}{Y_0}, \\
& d=\frac{4}{2(4+\hat{Z}+\hat{R})}, && Y_0=\sqrt{\frac{\varepsilon_o}{\mu_o}}, \\
& e=b, && \hat{R}_x=\sigma_{mx}\frac{\Delta l}{Z_0}, \\
& f=\hat{Z}d, && \\
& g=\hat{Y}b, && \hat{R}_y=\sigma_{my}\frac{\Delta l}{Z_0}, \\
& h=\frac{\hat{Y}-\hat{G}-4}{\hat{Y}+\hat{G}+4}, && \hat{R}_z=\sigma_{mz}\frac{\Delta l}{Z_0}, \\
& i=d, && \\
& j=\frac{4-\hat{R}-\hat{Z}}{4+\hat{R}+\hat{Z}}. && Z_0=\frac{1}{Y_0}.
\end{aligned}
\tag{2.25}
$$

The connection process in a nonhomogeneous lossy medium is implemented by exchanging the reflected impulse between the neighbouring nodes, which is the same as all the TLM problems. Because the capacitive stubs are modeled by an open circuit, the incident impulses in the next time step are equal to the current reflected impulses with a reflection coefficient +1. For the inductive stubs, the reflection coefficient is -1. For the loss stub, the energy is extracted out of the domain and no incident impulses appear on it.

The field components at each direction are given by [4]

$$
\begin{aligned}
E_x &= -\frac{2\left(V_1^i + V_2^i + V_9^i + V_{12}^i + \hat{Y}V_{13}^i\right)}{\Delta l(4+\hat{Y})}, \\
E_y &= -\frac{2\left(V_3^i + V_4^i + V_{11}^i + V_8^i + \hat{Y}V_{14}^i\right)}{\Delta l(4+\hat{Y})}, \\
E_z &= -\frac{2\left(V_5^i + V_6^i + V_7^i + V_{10}^i + \hat{Y}V_{15}^i\right)}{\Delta l(4+\hat{Y})}, \\
H_x &= \frac{2\left(V_4^i - V_5^i + V_7^i - V_8^i - V_{16}^i\right)}{\Delta l(4Z_o + Z_o\hat{Z})}, \\
H_y &= \frac{2\left(-V_2^i + V_6^i + V_9^i - V_{10}^i - V_{17}^i\right)}{\Delta l(4Z_o + Z_o\hat{Z})}, \\
H_z &= \frac{2\left(V_1^i - V_3^i + V_{11}^i - V_{12}^i - V_{18}^i\right)}{\Delta l(4Z_o + Z_o\hat{Z})}.
\end{aligned}
\tag{2.26}
$$

2.5 MODELING OF BOUNDARIES

In different electromagnetic problems, different boundary conditions may be required. In TLM, different boundaries are modeled for accurate simulation results. There are two main categories of boundary conditions: non dispersive boundaries and dispersive boundaries.

2.5.1 Non Dispersive Boundaries

For TLM problems with non dispersive boundaries, these boundaries are simply modeled by a reflection coefficient τ (2.27)

$$V_{k+1}^i = \tau V_{k+1}^r \tag{2.27}$$

Perfectly conducting boundaries (electric wall) is described by a short circuit. The connection process for such a boundary is given by

$$V_{k+1}^{i} = -V_{k+1}^{r} \text{ and } \tau = -1. \tag{2.28}$$

For magnetic wall, the connection process is given by

$$V_{k+1}^{i} = V_{k+1}^{r} \text{ and } \tau = 1. \tag{2.29}$$

For a non dispersive boundary with load impedance R_L, the reflection coefficient of each link-line is given by

$$\tau = \frac{R_L - Z_0}{R_L - Z_0}. \tag{2.30}$$

2.5.2 Dispersive Boundaries

2.5.2.1 Johns Matrix [5]

In TLM problems with dispersive boundaries, the response of the boundary can not be expressed by a single reflection coefficient τ. In many cases, the computational domain is truncated by absorbing boundaries which simulates perfect transmission of the wave with no reflections from the boundary into the computation domain. The most popular boundary condition for this case is Johns' matrix boundary [5], [6]. The idea is to determine the time domain impulse response of the boundary (the Johns matrix) beforehand. In order to model the absorbing boundary of a waveguide, a long enough waveguide section must be used to ensure that no reflections reach the input port before the simulation stops. To reduce the computation cost of Johns matrix, the implementation of gradually increasing losses in the waveguide section is introduced [15]. The wave is attenuated by the losses gradually within a much shorter waveguide section. Once the Johns matrix of a specific waveguide is calculated, it can be reused as long as the same waveguide is simulated. The response of arbitrary excitations to the waveguide can be obtained by convolving it with the Johns matrix. The TLM expression for a problem with Johns' matrix absorbing boundaries is [5]

$$\boldsymbol{V}_{k+1} = \boldsymbol{CSV}_k + \sum_{k'=0}^{k} \boldsymbol{J}(k-k')\boldsymbol{V}_{k'}^{r} + \boldsymbol{V}_k^{s} \tag{2.31}$$

where $\boldsymbol{J}(k)$ is the k^{th} time layer of the Johns matrix.

2.5.2.2 One-way Wave Equations [14]

In this technique, a boundary operator is used to guarantee the wave at the boundaries is travelling in the outgoing direction only. The fields of neighboring nodes at current and previous time step are used by the operator to calculate the fields at boundaries. The higher the operator order is; the more the absorption is. For the first-order boundary operator, the E-field at the m^{th} space step and the k^{th} time step is given by [14]

$$E^k(m,n,l) = \alpha_1 E^{k-1}(m,n,l) + \beta_1 E^k(m-1,n,l) + \gamma_1 E^{k-1}(m-1,n,l) \tag{2.32}$$

where α_1, β_1, and γ_1 are interpolation coefficients which depends on the wave angle of incident wave at the boundary. Reference [14] also presents higher-order boundary operators.

2.6 CONCLUSION

In this chapter, we briefly reviewed some of the basic concepts in the time-domain TLM method. We presented how to model different EM problems using time-domain TLM. Detailed algorithms for lossless homogeneous and lossy nonhomogeneous mediums in both 2-D and 3-D cases were shown. The 2-D shunt node was utilized for the 2-D TLM and the symmetrical condensed node (SCN) was utilized for the 3-D TLM. We also discussed different boundary conditions: dispersive and nondispersive. For dispersive boundary, both the techniques of Johns matrix and one-way wave equation were discussed.

REFERENCES

[1] P.B. Johns and R.L. Beurle, "Numerical modeling of 2-dimensional scattering problems using a transmission line matrix," *Proceedings of IEE*, vol. 118, no. 9, pp. 1203-1208, Sept. 1971.

[2] MEFiSTO-2D and MEFiSTO Nova, Faustus Scientific Corporation, 1998-2001.

[3] W.J.R. Hoefer, "The transmission-line matrix method-theory and applications," *IEEE Trans. Microwave Theory Tech.*, vol. MTT-33, pp.882-893, Oct. 1985.

[4] P.B. Johns, "A symmetrical condensed node for the TLM method," *IEEE Trans. Microwaves Theory Tech.*, vol. 35, no. 4, pp. 370-377, April 1987.

[5] W.J. Heofer, "The discrete time domain green's function or Johns' matrix- a new powerful concept in transmission line modeling (TLM),"*Int. Journal of Numerical Modeling: Electric Networks, Devices and Fields*, vol. 2, pp.215-225, Dec. 1989.

[6] E.G. Costache and W.J. Hoefer, "TLM modeling of dispersive wide-band absorbing boundaries with time domain diakoptics for S-parameter extraction," *IEEE Trans. Microwave Theory Tech.,*vol. 38, no. 4, pp.379-385, April 1990.

[7] M.H. Bakr and N.K. Nikolova, "An adjoint variable method for time-domain transmission-line modeling with fixed structured grids," *IEEE Trans. Microwave Theory Tech.*, vol. 52, NO. 2, pp554-559, Feb. 2004.

[8] C. Christopoulos, *The Transmission-Line Modeling Method TLM.* IEEE PRESS. 1955.

[9] R.A. Scaramuzza and A.J. Lowery, "Hybrid symmetrical condensed node for TLM method," *Electronics Lett.*, vol. 26, no. 23, pp. 1947-1949, Nov. 1990.

[10] P. Berini and K. Wu, "A pair of hybrid symmetrical condensed node," *IEEE Microwave and guided wave letters*, vol. 4, no. 7, pp. 244-246, July 1994.

[11] V. Trenkic, C. Christopoulos, and T.M. Benson, "New symmetrical super condensed node for TLM method," *Electronics lett.*, vol. 30, no. 4, pp. 329-330, Feb. 1994.

[12] V. Trenkic, C. Christopoulos, and T.M. Benson, "Development of a general symmetrical condensed node for the TLM method," *IEEE Trans. Microwaves Theory Tech.*, vol. 44, no. 12, pp. 2129-2135, Dec. 1996.

[13] V. Trenkic, C. Christopoulos, and T.M. Benson, "Generally graded mesh using the symmetrical super condensed node," *Electronics Lett.*, vol. 30, no. 10, pp. 795-797, May 1994.

[14] C. Eswarappa and W.J.R. Hoefer, "One-way equation absorbing boundary conditions for 3-D TLM analysis of planar and quasi-planar structures," *IEEE Trans. Microw. Theory and Tech.*, vol. 42, pp. 1669-1677, 1994.

[15] C. Eswarappa and W.J.R. Hoefer, "Diakoptics and wideband dispersive absorbing boundaries in the 3-D TLM method with symmetrical condensed nodes," *IEICE Transactions*, vol. E74, pp. 1242-1250, 1991.

CHAPTER 3

THE ADJOINT-VARIABLE METHOD FOR TIME-DOMAIN TLM

3.1 INTRODUCTION

Sensitivity analysis is essential to many electromagnetic (EM) problems including gradient-based optimization, tolerance analysis, and yield analysis. For an EM structure, the optimization problem can be expressed as

$$\boldsymbol{x}^* = \arg\left\{\min_{\boldsymbol{x}} F(\boldsymbol{x}, \boldsymbol{R}(\boldsymbol{x}))\right\} \tag{3.1}$$

where $\boldsymbol{x}^*$ is the vector of optimal parameters, $\boldsymbol{x}$ is the vector of optimizable parameters, $\boldsymbol{R}(\boldsymbol{x})$ is the vector of responses, and F is the objective function to be optimized. The problem in (3.1) is usually solved using gradient-based optimizers. In this case, the optimizers need not only the structure response but also its derivatives with respect to all designable parameters. The traditional approach to estimate sensitivities utilizes Finite

Difference (FD) approximations. These approximations are time-intensive even for simple problems. The Adjoint Variable Method (AVM), on the other hand, efficiently estimates the sensitivities analysis using at most two simulations of the original and adjoint systems.

This chapter reviews the mathematical derivation of the sensitivity analysis of time-domain TLM problems using the AVM. The algorithm is first derived for 2-D time-domain TLM problems including metallic discontinuities, dielectric discontinuities, and waveguides with wide-band Johns matrix boundaries [1]-[3]. The AVM algorithm is then derived for 3-D metallic and dielectric discontinuities [4]. The last section discusses the further developments of the AVM including self-adjoint *S*-parameter sensitivities for lossless homogeneous and nonhomogeneous TLM problems [5], [6], sensitivities of planar structures using first-order one-way wave equation boundaries [7], and AVM for conformal TLM based on the rubber cell implementation [8].

3.2 AVM FOR 2-D TIME-DOMAIN TLM METHOD [1]-[3]

In this section we discuss how the sensitivities of 2-D time-domain TLM problems can be estimated using the AVM. The objective function as a function of the vector of optimizable parameters $\boldsymbol{x}$ has the form [1]

$$F = \int_{0}^{T_m} \int_{\Omega} g(\boldsymbol{x}, \boldsymbol{V}) d\Omega dt = \int_{0}^{T_m} G(\boldsymbol{x}, \boldsymbol{V}) dt \tag{3.2}$$

where $G(\boldsymbol{x},\boldsymbol{V})$ is the objective function's kernel, Ω is the observation domain, $\boldsymbol{V}$ is the continuous vector of $\boldsymbol{V}_k$, the vector of incident impulses for all nodes at the k^{th} time step, and T_m is the maximum simulation time. The analytic derivative of this objective function with respect to the i^{th} parameter is given by

$$\frac{\partial F}{\partial x_i} = \int_{0}^{T_m} \frac{\partial^e G}{\partial x_i} dt + \int_{0}^{T_m} \left(\frac{\partial G}{\partial \boldsymbol{V}}\right)^T \frac{\partial \boldsymbol{V}}{\partial x_i} dt \tag{3.3}$$

where $\partial^e / \partial x_i$ denotes the explicit dependence of the objective function on the i^{th} design parameter which is equal to zero in most practical cases.

To solve (3.3), $\partial \boldsymbol{V}/\partial x_i$ should be computed. The derivative $\partial G / \partial \boldsymbol{V}$ can be easily obtained analytically by taking the derivatives of $G(\boldsymbol{x},\boldsymbol{V})$ with respect to $\boldsymbol{V}$. There are two possible approaches to estimate $\partial \boldsymbol{V}/\partial x_i$ in (3.3). The first one involves using FD approximations which may be time intensive. The alternative approach is the AVM which efficiently estimates the sensitivities using at most one extra adjoint simulation.

Assuming that a band-limited excitation is applied and a sufficiently small time step Δt is utilized, the vector of incident impulses at the $k+1^{\text{th}}$ time step can be approximated using first order Taylor's series [1]

$$\begin{aligned} \boldsymbol{V}_{k+1} &= \boldsymbol{V}\ (k\Delta t + \Delta t) \\ &\approx \boldsymbol{V}_k + \left(\frac{\partial \boldsymbol{V}}{\partial t}\right)_k \Delta t. \end{aligned} \tag{3.4}$$

Comparing (2.2) and (3.4), we get

$$\boldsymbol{V}_k + \left(\frac{\partial \boldsymbol{V}}{\partial t}\right)_k \Delta t \approx \boldsymbol{CSV}_k + \boldsymbol{V}_k^s. \tag{3.5}$$

Rearranging (3.5), we get

$$\frac{\partial \boldsymbol{V}}{\partial t} = \boldsymbol{A}(x)\boldsymbol{V} + \frac{\boldsymbol{V}^s}{\Delta t} \tag{3.6}$$

where $\boldsymbol{A}(\boldsymbol{x}) = (\boldsymbol{C}(\boldsymbol{x})\boldsymbol{S}(\boldsymbol{x}) - \boldsymbol{I}) / \Delta t$ and $\boldsymbol{I}$ is the identity matrix. The matrix $\boldsymbol{A}$ is the system matrix which contains all the information about the material properties and the connections of all nodes.

Perturbing one of the designable parameters x_i by Δx_i causes a perturbation of $\Delta \boldsymbol{A}_i$ in the system matrix $\boldsymbol{A}$. It also causes a perturbation of $\Delta \boldsymbol{V}_i$ of the vector of incident impulses. For the perturbed system, (3.6) can be written as

$$\frac{\partial (\boldsymbol{V} + \Delta \boldsymbol{V}_i)}{\partial t} = \left(\boldsymbol{A}(x) + \Delta \boldsymbol{A}_i\right)\left(\boldsymbol{V} + \Delta \boldsymbol{V}_i\right) + \frac{\boldsymbol{V}^s}{\Delta t}. \tag{3.7}$$

Simplifying (3.6) and (3.7), we get

$$\frac{\partial \Delta \boldsymbol{V}_i}{\partial t} = \Delta \boldsymbol{A}_i \boldsymbol{V} + \boldsymbol{A}(x)\Delta \boldsymbol{V} + \Delta \boldsymbol{A}_i \Delta \boldsymbol{V}_i. \tag{3.8}$$

Dividing both sides of (3.8) by Δx_i, we obtain the second order derivative expression

$$\frac{\partial^2 \boldsymbol{V}}{\partial t \partial x_i} \approx \frac{\Delta \boldsymbol{A}_i}{\Delta x_i} \boldsymbol{V} + \boldsymbol{A} \frac{\partial \boldsymbol{V}}{\partial x_i} + \Delta \boldsymbol{A}_i \frac{\partial \boldsymbol{V}}{\partial x_i}. \tag{3.9}$$

The adjoint vector $\boldsymbol{\lambda}$ is defined by [9]:

$$\int_0^{T_m} \boldsymbol{\lambda}^T \left(\frac{\partial^2 \boldsymbol{V}}{\partial t \partial x_i} - \frac{\Delta \boldsymbol{A}_i}{\Delta x_i} \boldsymbol{V} - \boldsymbol{A} \frac{\partial \boldsymbol{V}}{\partial x_i} - \Delta \boldsymbol{A}_i \frac{\partial \boldsymbol{V}}{\partial x_i} \right) dt = 0. \tag{3.10}$$

Integrating the first term in the bracket by parts, we get

$$\boldsymbol{\lambda}^T \frac{\partial \boldsymbol{V}}{\partial x_i} \bigg|_0^{T_m} - \int_0^{T_m} \left(\frac{\partial \boldsymbol{\lambda}^T}{\partial t} + \boldsymbol{\lambda}^T (\boldsymbol{A} + \Delta \boldsymbol{A}_i) \right) \frac{\partial \boldsymbol{V}}{\partial x_i} dt = - \int_0^{T_m} \boldsymbol{\lambda}^T \frac{\Delta \boldsymbol{A}_i}{\Delta x_i} \boldsymbol{V} dt. \tag{3.11}$$

The first term in (3.11) is equal to zero because $\boldsymbol{\lambda}(T_m) = \boldsymbol{0}$ and $\boldsymbol{V}(0) = \boldsymbol{0}$. Comparing (3.11) with (3.3), we set [1]

$$\frac{\partial \boldsymbol{\lambda}^T}{\partial t} + \boldsymbol{\lambda}^T (\boldsymbol{A} + \Delta \boldsymbol{A}_i) = \left(\frac{\partial G}{\partial \boldsymbol{V}} \right)^T. \tag{3.12}$$

Expanding the matrix $\boldsymbol{A}$, (3.12) results in the discrete time form:

$$\boldsymbol{\lambda}_{k-1} = \boldsymbol{S}^T (\boldsymbol{x} + \Delta x_i \boldsymbol{e}_i) \boldsymbol{C}^T (\boldsymbol{x} + \Delta x_i \boldsymbol{e}_i) \boldsymbol{\lambda}_k - \boldsymbol{V}_k^{s,\lambda}, \ \boldsymbol{\lambda}(T_m) = \boldsymbol{0} \tag{3.13}$$

where $\boldsymbol{V}_k^{s,\lambda} = \Delta t (\partial G / \partial \boldsymbol{V})_{k\Delta t}$ is the adjoint excitation. The system (3.13) is the adjoint system.

Because (3.13) is a parameter dependent system, it has to be solved for each parameter. This is not efficient, so an assumption is used to overcome this problem. Since the perturbation of each parameter is very small and does not affect the incident impulses significantly, the adjoint impulses are approximated by the values of the corresponding incident impulses for the unperturbed adjoint problem (3.14) [1]

$$\boldsymbol{\lambda}_{k-1} = \boldsymbol{S}^T (\boldsymbol{x}) \boldsymbol{C}^T (\boldsymbol{x}) \boldsymbol{\lambda}_k - \boldsymbol{V}_k^{s,\lambda}, \ \boldsymbol{\lambda}(T_m) = \boldsymbol{0} \tag{3.14}$$

Combining (3.3), (3.11), and (3.12), the sensitivity of F with respect to i^{th}

parameter can be expressed as

$$\begin{aligned}\frac{\partial F}{\partial x_i} &= \frac{\partial^e F}{\partial x_i} - \int_0^{T_m} \lambda^T \frac{\Delta \boldsymbol{A}_i}{\Delta x_i} \boldsymbol{V} dt \\ &\approx \frac{\partial^e F}{\partial x_i} - \Delta t \sum_k \boldsymbol{\lambda}_k^T \frac{\Delta \boldsymbol{A}_i}{\Delta x_i} \boldsymbol{V}_k \\ &= \frac{\partial^e F}{\partial x_i} - \Delta t \sum_k \boldsymbol{\lambda}_k^T \boldsymbol{\eta}_k^i\end{aligned} \tag{3.15}$$

where the vector $\boldsymbol{\eta}_k^i = (\Delta \boldsymbol{A}_i / \Delta x_i) \boldsymbol{V}_k$ is a linear combination of the original impulses. The vector $\boldsymbol{\lambda}$ is obtained from the backward running adjoint system (3.14).

To calculate (3.15), $\boldsymbol{\lambda}$, $\boldsymbol{V}_k$ and $\Delta \boldsymbol{A}_i$ must be determined. $\boldsymbol{\lambda}$ is obtained from adjoint system, and $\boldsymbol{V}_k$ is from the original system. The $\Delta \boldsymbol{A}_i$ is the change of system matrix due to the perturbation of optimizable parameter $\boldsymbol{x}_i$, so only the links affected by the perturbation of the i^{th} parameter have non-zero values of $\Delta \boldsymbol{A}_i$. Accordingly, only a few of impulses are stored in both the original system and the adjoint system. The parameter perturbation causes different perturbations for both metallic discontinuities and dielectric discontinuities. Different implementation is utilized in each case. The perturbation in metallic discontinuity causes only the connection matrix to change. On the other hand, only the scattering matrix changes for dielectric discontinuities. The implementation of metallic discontinuity and dielectric discontinuity is discussed separately.

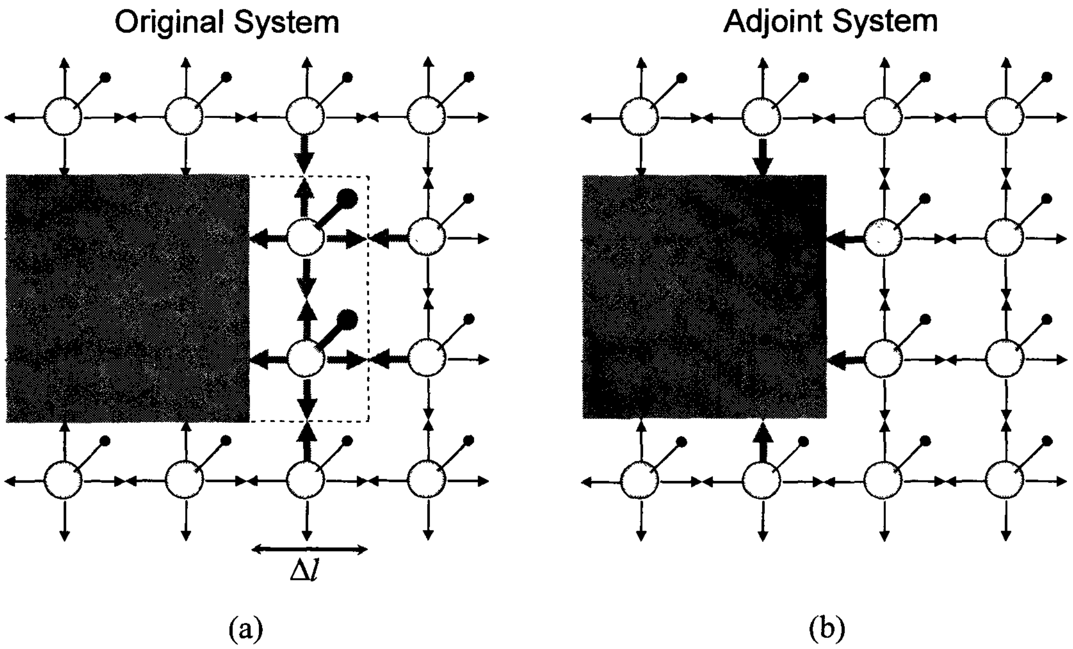

Original System

Adjoint System

(a)

(b)

Figure 3.1: Illustration of the links storage. (a) The red arrowed bold links are the ones for which the matrix ΔA has nonzero components for a perturbation of $1\Delta l$ of the parameter L. (b) The adjoint impulses are approximated by their corresponding ones for the unperturbed structure. [1]

3.2.1 Metallic Discontinuities

A perturbation in a metallic discontinuity causes a change of the system matrix. This change is due to the perturbation of the connection matrix of the links around the discontinuity:

$$\Delta \boldsymbol{A}_i = \frac{\Delta \boldsymbol{C}_i \boldsymbol{S}(\boldsymbol{x})}{\Delta t} = \frac{\boldsymbol{C}(\boldsymbol{x}+\Delta x_i)\boldsymbol{S}(\boldsymbol{x}) - \boldsymbol{C}(\boldsymbol{x})\boldsymbol{S}(\boldsymbol{x})}{\Delta t}. \tag{3.16}$$

The evaluation of the components of the vector η_k^i depends on the way nodes are metallized or demetallized with a perturbation of Δx_i. We consider the case where the n^{th}

link-line is metallized after the perturbation and the m^{th} link-line is connected to the n^{th} link in the nominal structure. The m^{th} component of the vector η_k^i is thus given by:

$$\begin{aligned}\eta_{k,m}^i &= \frac{1}{\Delta x_i}\left(\left(\boldsymbol{A}(\boldsymbol{x}+\Delta x_i\boldsymbol{e}_i)-\boldsymbol{A}(\boldsymbol{x})\right)\boldsymbol{V}_k\right)_m \\ &= \frac{1}{\Delta x_i \Delta t}\left(\boldsymbol{C}(\boldsymbol{x}+\Delta x_i)\boldsymbol{S}(\boldsymbol{x})\boldsymbol{V}_k - \boldsymbol{C}(\boldsymbol{x})\boldsymbol{S}(\boldsymbol{x})\boldsymbol{V}_k\right)_m.\end{aligned} \tag{3.17}$$

After the perturbation, the m^{th} link is connected to the metallic boundary. The first term in (3.17) changes to [1]

$$\left(\boldsymbol{C}(\boldsymbol{x}+\Delta x_i)\boldsymbol{S}(\boldsymbol{x})\boldsymbol{V}_k\right)_m = \boldsymbol{V}_{k+1,m} = -\boldsymbol{V}_{k,m}^r, \tag{3.18}$$

The second term in (3.17) refers to the unperturbed problem and is equal to

$$\left(\boldsymbol{C}(\boldsymbol{x})\boldsymbol{S}(\boldsymbol{x})\boldsymbol{V}_k\right)_m = \boldsymbol{V}_{k+1,m} = \boldsymbol{V}_{k,n}^r. \tag{3.19}$$

Substituting (3.18) and (3.19) into (3.17), the m^{th} component of the vector η_k^i is obtained

$$\eta_{k,m}^i = -\frac{1}{\Delta x_i \Delta t}(\boldsymbol{V}_{k,m}^r + \boldsymbol{V}_{k,n}^r). \tag{3.20}$$

Figure 3.1 illustrates the links in metallic discontinuities which have nonzero $\Delta\boldsymbol{A}$ components and should be stored during the simulation.

3.2.2 Dielectric Discontinuities

The variation of the system matrix due to a perturbation in a dielectric discontinuity is caused by corresponding change in the scattering matrix. The connection matrix remains the same. In this case, the vector η_k^i is given by

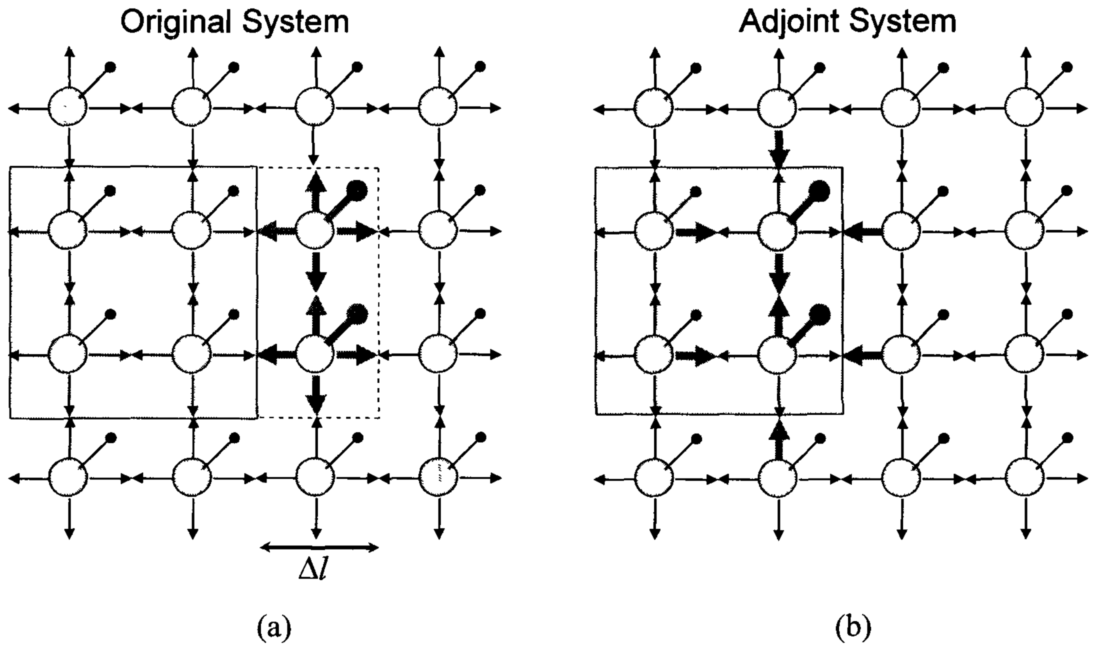

Figure 3.2: Illustration of the links storage. (a) The red arrowed bold links are the ones for which the matrix ΔS_i has nonzero components for a perturbation of $1\Delta l$ of the parameter L. (b) The adjoint impulses are approximated by their corresponding ones for the unperturbed structure. [3]

$$\eta_k^i = \frac{C(x)\Delta S_i}{\Delta x_i \Delta t} = \frac{1}{\Delta x_i \Delta t} C(x)\big(S(x+\Delta x_i) - S(x)\big)V_k. \tag{3.21}$$

The element of ΔS_i is zero everywhere except for the nodes which are affected by the perturbation Δx_i. Figure 3.2 illustrates that the links in dielectric discontinuities which have nonzero ΔS_i components and should be stored during the simulation.

There is another approach for estimating the sensitivities related to dielectric discontinuities [3]. If perturbing a parameter x_i results in changing the dielectric constant of a certain number of nodes with index $n \in \{l, l+1, ..., l+m\}$, then the analytical expression of (3.15) is given by [4]

$$\begin{aligned}\frac{\partial F}{\partial x_i} &= \frac{\partial^e F}{\partial x_i} + \sum_{n=l}^{l+m}\left(\frac{\partial F}{\partial \varepsilon_{r,n}} \cdot \frac{\partial \varepsilon_{r,n}}{\partial x_i}\right) \\ &\approx \frac{\partial^e F}{\partial x_i} + \sum_{n=l}^{l+m}\left(\frac{\partial F}{\partial \varepsilon_{r,n}} \cdot \frac{\Delta \varepsilon_{r,n}}{\Delta x_i}\right)\end{aligned} \qquad (3.22)$$

where $\varepsilon_{r,n}$ is the relative dielectric constant of the n^{th} “dielectrified” node. $\partial F / \partial \varepsilon_{r,n}$ is given by [3]

$$\frac{\partial F}{\partial \varepsilon_{r,n}} = \frac{\partial^e F}{\partial \varepsilon_{r,n}} - \Delta t \sum_k \lambda_k^T \frac{\partial A_i}{\partial \varepsilon_{r,n}} V_k \qquad (3.23)$$

where $\partial A_i / \partial \varepsilon_{r,n}$ is the analytical derivative of the system matrix with respect to the relative dielectric constant of the n^{th} node. Thus, (3.22) is given by

$$\frac{\partial F}{\partial x_i} \approx \frac{\partial^e F}{\partial x_i} - \Delta t \sum_{n=l}^{l+m} \sum_k \left(\lambda_k^T \frac{\partial A_i}{\partial \varepsilon_{r,n}} V_k \cdot \frac{\Delta \varepsilon_{r,n}}{\Delta x_i}\right). \qquad (3.24)$$

The sensitivities estimated using this approach are more accurate because there is no approximation introduced in the procedure. This approach makes use of the analytic dependence on the local material properties. However, perfectly conducting discontinuities do not have such dependence.

3.2.3 Practical Implementation

The AVM algorithm is implemented in an efficient way. In the implementation, the summation term in (3.15) is simplified as [1]

$$\sum_k \lambda_k^T \eta_k^i = \sum_k \sum_p \lambda_{k,p} \eta_{k,p}^i \tag{3.25}$$

where the subscript p denotes the p^{th} component with $p \in L_i$. L_i is the set of indexes whose corresponding connection and scattering matrix changed by the perturbation Δx_i, 1, 2,…, n.

The AVM algorithm can thus be summarized in the following steps.

Step 1) *Parameterization*: Determine the sets of link indexes L_i whose connection and scattering matrices are affected by the perturbations Δx_i, 1, 2,…, n.

Step 2) *Original Analysis*: Carry out the original TLM analysis (2.2) and store the set of corresponding η values $\forall m \in L_i,\ i = 1,\ 2, ..., n$ at each time step. The values of the incident impulses in the observation domain are also stored to determine the adjoint excitation in (3.13).

Step 3) *Adjoint Analysis*: Carry out the backward adjoint analysis (3.13). The adjoint excitation is determined from step 2). Store the adjoint impulses for the links with indexes $L_i,\ i = 1,\ 2, ..., n$ in the unperturbed structure for all time steps.

Step 4) *Sensitivities Estimation*: Evaluate (3.15) for all parameters.

3.3 AVM FOR 3-D TIME-DOMAIN TLM METHOD [4]

In this section we discuss how the sensitivities of 3-D TLM problems are estimated using the AVM. The node type utilized in the 3-D time-domain TLM is the

Symmetric Condensed Node (SCN). The derivation of mathematical formulation is exactly the same as the 2-D time-domain TLM problem, so the practical implementation follows exactly the same steps as those in the previous section. The only difference is that the number of stored impulses is different between 2-D and 3-D TLM problems. The required memory space for 3-D problems is much larger than it for 2-D problems.

Again the implementation of the metallic discontinuity is different from it of dielectric discontinuity. Figure 3.3 illustrates the links in metallic discontinuities that should be stored during the simulation. Assume the perturbation is $1\Delta l$ in the x direction, the metalized nodes are $a \times b \times c$ nodes in the perturbed region. According to (3.20), only the links around the discontinuity of the perturbed structure should be stored in the original system, so the total number of stored links is $2T_m\left(b \times c + 2a \times c + 2a \times b\right)$.

For the dielectric discontinuity, all the 18 links of each node at perturbed region should be stored (Figure 3.4). If there are $a \times b \times c$ nodes with non-zero ΔA_i, then $18a \times b \times c$ impulses should be stored at each time step. The total number of stored links through whole simulation is $18T_m \times a \times b \times c$.

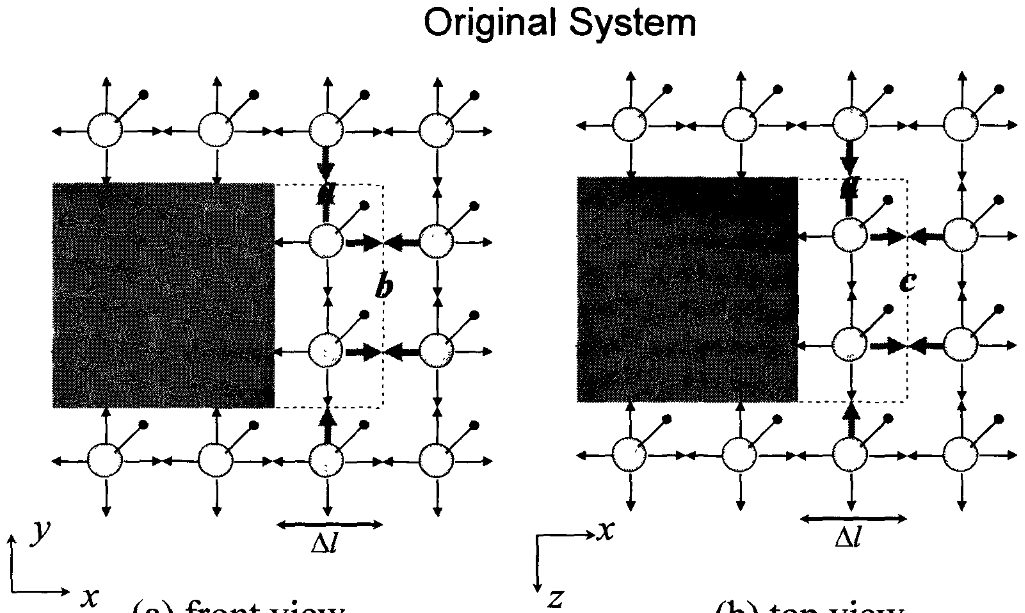
Original System

(a) front view (b) top view

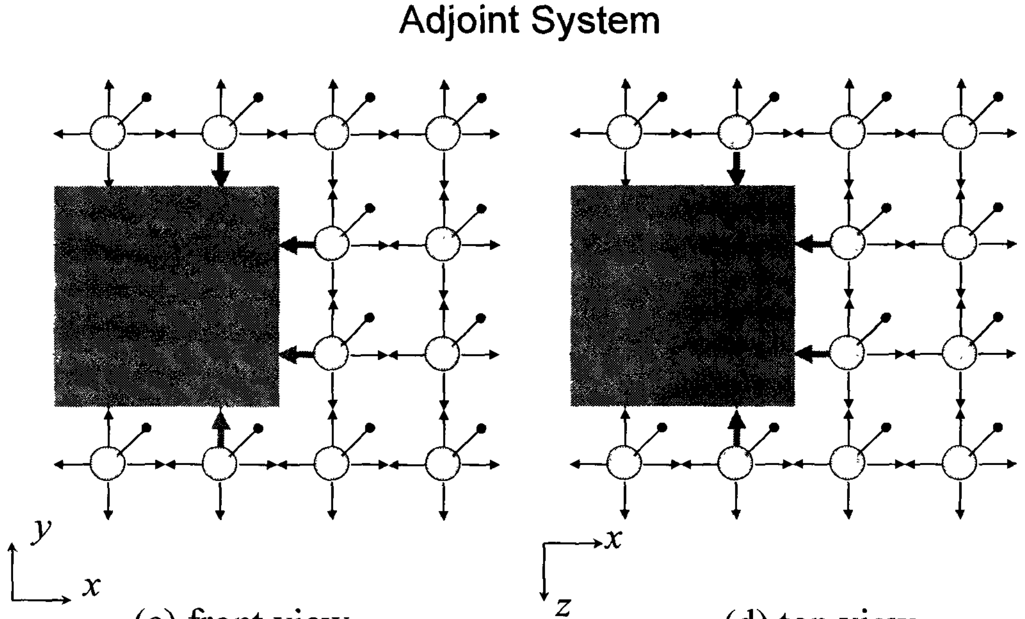
Adjoint System

(c) front view (d) top view

Figure 3.3: Illustration of the links storage for the 3-D metallic discontinuity parameters. a, b, and c are number of nodes in each direction. The red arrowed bold links are the ones should be stored for perturbation of1Δl [4].

Original System

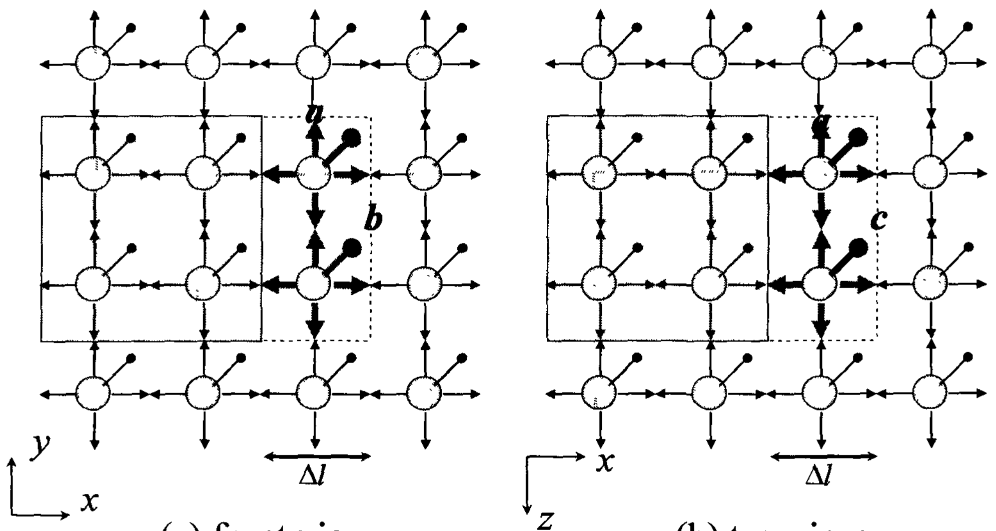

(a) front view (b) top view

Adjoint System

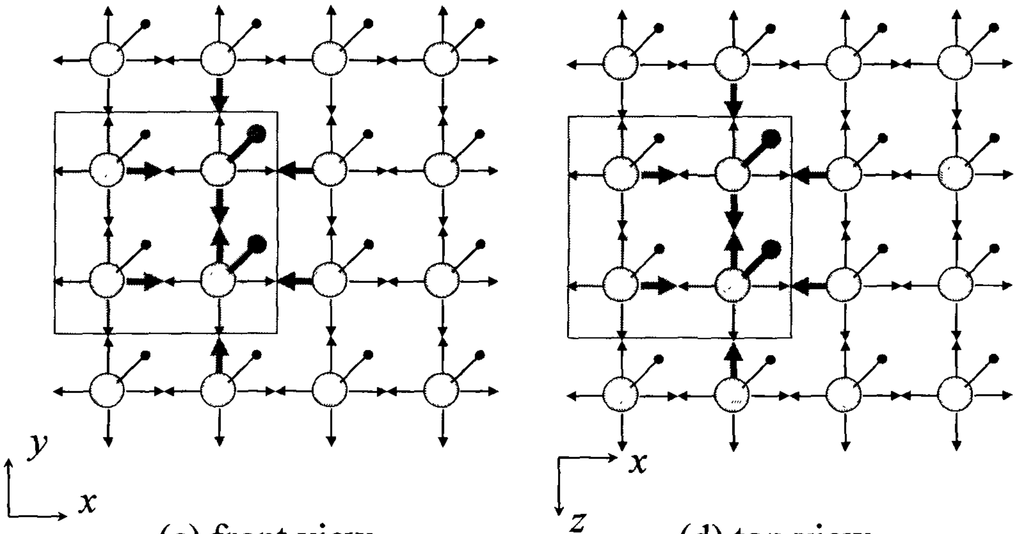

(c) front view (d) top view

Figure 3.4: Illustration of the links storage for 3-D dielectric discontinuity parameters. a, b, and c are number of nodes in each direction. The red arrowed bold links are the ones should be stored for perturbation of1Δ*l* [4].

3.4 AVM FOR TIME-DOMAIN TLM WITH WIDE-BAND JOHNS MATRIX BOUNDARY [2]

The previous sections discussed the case of the AVM for the time-domain TLM with non dispersive boundaries. In this section, the implementation of the AVM for TLM with wide-band Johns matrix is presented. As explained in Chapter 2, the TLM expression for a problem with Johns matrix absorbing boundaries is [2]

$$\boldsymbol{V}_{k+1} = \boldsymbol{CSV}_k + \boldsymbol{V}_k^s + \sum_{k'=0}^{k} \boldsymbol{J}(k-k')\boldsymbol{V}_{k'}^r \tag{3.26}$$

where $\boldsymbol{J}(k)$ is the k^{th} time layer of the 3-D Johns matrix [10], $\boldsymbol{V}_k^s$ is the vector of source excitation at the k^{th} time step, $\boldsymbol{V}_k$ is the vector of incidents for all the nodes at the k^{th} time step, and $\boldsymbol{V}_k^r$ is the corresponding vector of reflected impulses. The summation in (3.26) is actually the time-domain convolution of the reflected impulses toward boundaries and the time-discrete Johns matrix [10].

For the simplification, the following vector expression is used [2]:

$$\begin{aligned}
\boldsymbol{V}_k &= \begin{bmatrix} \boldsymbol{V}_k^N \\ \boldsymbol{V}_k^D \end{bmatrix} \\
\boldsymbol{V}_k^R &= \begin{bmatrix} \boldsymbol{V}_k^{R,N} \\ \boldsymbol{V}_k^{R,D} \end{bmatrix} \\
\boldsymbol{C} &= \begin{bmatrix} \boldsymbol{C}^N & \boldsymbol{0} \\ \boldsymbol{0} & \boldsymbol{0} \end{bmatrix} \\
\boldsymbol{S} &= \begin{bmatrix} \boldsymbol{S}^{NN} & \boldsymbol{S}^{ND} \\ \boldsymbol{S}^{DN} & \boldsymbol{S}^{DD} \end{bmatrix}
\end{aligned} \tag{3.27}$$

where the superscript D represents links ending on the Johns matrix boundaries, and N

represents links connected to everywhere else except the dispersive boundaries.

If we consider the Johns matrix, (3.5) is rewritten as follows [2].

$$\boldsymbol{V}_k + \left(\frac{\partial \boldsymbol{V}}{\partial t}\right)_k \Delta t \approx \boldsymbol{CSV}_k + \boldsymbol{V}_k^s + \sum_{k'=0}^{k} \boldsymbol{J}(k-k')\boldsymbol{SV}_{k'}. \tag{3.28}$$

Equation (3.28) can be simplified to (3.29) if we use $\boldsymbol{A}(\boldsymbol{x}) = (\boldsymbol{CS}-\boldsymbol{I})/\Delta t$ [2],

$$\frac{\partial \boldsymbol{V}}{\partial t} = \boldsymbol{A}(\boldsymbol{x})\boldsymbol{V} + \frac{\boldsymbol{V}^s}{\Delta t} + \frac{1}{\Delta t^2}\int_0^{T_m} \boldsymbol{J}(t-\tau)\boldsymbol{SV}(\tau)d\tau. \tag{3.29}$$

A perturbation of x_i causes perturbations $\Delta \boldsymbol{A}_i$ of system matrix $\boldsymbol{A}$ and $\Delta \boldsymbol{V}_i$ of the vector $\boldsymbol{V}$. Therefore, the perturbed system has the following expression:

$$\begin{aligned} \frac{\partial(\boldsymbol{V}+\Delta \boldsymbol{V}_i)}{\partial t} &= \left(\boldsymbol{A}(\boldsymbol{x})+\Delta \boldsymbol{A}_i\right)(\boldsymbol{V}+\Delta \boldsymbol{V}_i) + \frac{\boldsymbol{V}^s}{\Delta t}\ldots \\ &+ \frac{1}{\Delta t^2}\int_0^{T_m} \boldsymbol{J}(t-\tau)\left(\boldsymbol{S}+\Delta \boldsymbol{S}_i\right)\left(\boldsymbol{V}(\tau)+\Delta \boldsymbol{V}_i(\tau)\right)d\tau. \end{aligned} \tag{3.30}$$

Combining (3.29) and (3.30), we get

$$\begin{aligned} \frac{\partial \Delta \boldsymbol{V}_i}{\partial t} &= \Delta \boldsymbol{A}_i \boldsymbol{V} + \boldsymbol{A}(\boldsymbol{x})\Delta \boldsymbol{V}_i + \Delta \boldsymbol{A}_i \Delta \boldsymbol{V}\ldots \\ &+ \frac{1}{\Delta t^2}\int_0^{T_m} \boldsymbol{J}(t-\tau)\left[\Delta \boldsymbol{S}_i\left(\boldsymbol{V}(\tau)+\Delta \boldsymbol{V}_i(\tau)\right)+\boldsymbol{S}\Delta \boldsymbol{V}_i(\tau)\right]d\tau. \end{aligned} \tag{3.31}$$

Because the optimizable parameters are normally the geometrical dimensions or the dielectric properties of the discontinuities which are located far way from the boundary, the boundary nodes are not affected by the perturbation [2]. It implies that $\Delta \boldsymbol{S}^{DD} = \boldsymbol{0}$ and (3.31) is simplified to

$$\frac{\partial \Delta \boldsymbol{V}_i}{\partial t} = \Delta \boldsymbol{A}_i \boldsymbol{V} + \boldsymbol{A}(\boldsymbol{x})\Delta \boldsymbol{V}_i + \Delta \boldsymbol{A}_i \Delta \boldsymbol{V} + \frac{1}{\Delta t^2}\int_0^{T_m} \boldsymbol{J}(t-\tau)\boldsymbol{S}\Delta \boldsymbol{V}_i(\tau)d\tau. \tag{3.32}$$

Dividing both sides by Δx_i, we get

$$\frac{\partial^2 \boldsymbol{V}}{\partial t \partial x_i} \approx \frac{\Delta \boldsymbol{A}_i}{\Delta x_i}\boldsymbol{V} + \boldsymbol{A}\frac{\partial \boldsymbol{V}}{\partial x_i} + \Delta \boldsymbol{A}_i \frac{\partial \boldsymbol{V}}{\partial x_i} + \frac{1}{\Delta t^2}\int_0^{T_m} \boldsymbol{J}(t-\tau)\boldsymbol{S}\frac{\partial \boldsymbol{V}(\tau)}{\partial x_i}d\tau. \tag{3.33}$$

Now we follow the same step as (3.10)-(3.12), introducing the adjoint vector $\boldsymbol{\lambda}$, integration by parts and solving the equations, we get the adjoint system [2]

$$\boldsymbol{\lambda}_{k-1} = \boldsymbol{S}^T(\boldsymbol{x}+\Delta x_i e_i)\boldsymbol{C}^T(\boldsymbol{x}+\Delta x_i e_i)\boldsymbol{\lambda}_k + \boldsymbol{S}^T\sum_{k'=k}^{N_t}\boldsymbol{J}^T(k'-k)\boldsymbol{\lambda}_{k'} - \boldsymbol{V}_k^{s,\lambda},\ \boldsymbol{\lambda}(T_m)=\boldsymbol{0}. \tag{3.34}$$

Again we use the mapping approximation for the adjoint system, (3.34) can be rewritten as

$$\boldsymbol{\lambda}_{k-1} = \boldsymbol{S}^T(\boldsymbol{x})\left(\boldsymbol{C}^T(\boldsymbol{x})\boldsymbol{\lambda}_k + \sum_{k'=k}^{N_t}\boldsymbol{J}^T(k'-k)\boldsymbol{\lambda}_{k'}\right) - \boldsymbol{V}_k^{s,\lambda},\ \boldsymbol{\lambda}(T_m)=\boldsymbol{0}. \tag{3.35}$$

The original impulses and the adjoint impulses are stored from the simulation of (3.28) and (3.35), respectively. Then, the sensitivities can be calculated as follows:

$$\begin{aligned} \frac{\partial F}{\partial x_i} &= \frac{\partial^e F}{\partial x_i} - \int_0^{T_m} \boldsymbol{\lambda}^T \frac{\Delta \boldsymbol{A}_i}{\Delta x_i}\boldsymbol{V}dt \\ &\approx \frac{\partial^e F}{\partial x_i} - \Delta t \sum_k \boldsymbol{\lambda}_k^T \frac{\Delta \boldsymbol{A}_i}{\Delta x_i}\boldsymbol{V}_k \\ &= \frac{\partial^e F}{\partial x_i} - \Delta t \sum_k \boldsymbol{\lambda}_k^T \boldsymbol{\eta}_k^i. \end{aligned} \tag{3.36}$$

It should be noted that the Johns matrix of the adjoint system at each time step is the transpose of the corresponding Johns matrix for the original system. Once the Johns matrix of the original structure is obtained, the sensitivities can be computed following the same steps as the AVM for the TLM problem with non dispersive boundaries.

3.5 AVM FOR PLANAR STRUCTURES USING FIRST-ORDER ONE-WAY WAVE EQUATION BOUNDARIES [7]

In the previous section, we discussed the AVM for structures with Johns matrix boundary. In this section, another kind of dispersive boundary, one-way wave equation absorbing boundary condition is presented [7]. The first-order one-way wave equation boundary is utilized because of its simplicity compared with other higher order boundaries. The original system and adjoint system are derived.

A first-order one-way wave equation absorbing boundary condition is derived in [13]. The E-field at the m^{th} space step and the k^{th} time step is given by [13]

$$E^{k+1}(m,n,l)=\alpha_1 E^k(m,n,l)+\beta_1 E^{k+1}(m-1,n,l)+\gamma_1 E^k(m-1,n,l) \tag{3.37}$$

where α_1, β_1, and γ_1 are interpolation coefficients which depends on the wave angle of incident wave at the boundary. Only the fields at neighbouring nodes and the previous time step are used to compute current fields. A TLM step with a first-order one-way wave equation boundary is given by [13]

$$\boldsymbol{V}_{k+1}=\boldsymbol{CSV}_k+\boldsymbol{V}_k^s+\boldsymbol{\alpha V}_k+\boldsymbol{\beta V}_{k+1}^{'}+\boldsymbol{\gamma V}_k \tag{3.38}$$

where $\boldsymbol{V}_{k+1}^{'}$ is the vector of incident impulses at selected nodes adjacent to the boundaries at the next time step. Only few components corresponding to the field $E^{k+1}(m-1,n,l)$ is stored for $\boldsymbol{V}_{k+1}^{'}$.

A simplified notation is utilized to make the links connected to the absorbing boundaries indexed last [7]

$$\boldsymbol{V}_k=\begin{bmatrix}\boldsymbol{V}_k^N\\ \boldsymbol{V}_k^D\end{bmatrix},\ \boldsymbol{C}=\begin{bmatrix}\boldsymbol{C}^N & 0\\ 0 & 0\end{bmatrix},\ \boldsymbol{S}=\begin{bmatrix}\boldsymbol{S}^{NN} & \boldsymbol{S}^{ND}\\ \boldsymbol{S}^{DN} & \boldsymbol{S}^{DD}\end{bmatrix},$$
$$\boldsymbol{\alpha}=\begin{bmatrix}0 & 0\\ 0 & \alpha_1\end{bmatrix},\ \boldsymbol{\beta}=\begin{bmatrix}0 & 0\\ \beta_1 & 0\end{bmatrix},\ \boldsymbol{\gamma}=\begin{bmatrix}0 & 0\\ \gamma_1 & 0\end{bmatrix}. \tag{3.39}$$

where the superscript D represents links ending on dispersive boundaries, and N represents links connected to everywhere else except the dispersive boundaries. Assuming that there is no excitation on the one-way wave equation boundaries, (3.38) is rewritten by substituting $\boldsymbol{V}_{k+1}^{'}=\boldsymbol{CSV}_k$,

$$\begin{aligned}\boldsymbol{V}_{k+1}&=\boldsymbol{CSV}_k+\boldsymbol{V}_k^s+\boldsymbol{\alpha V}_k+\boldsymbol{\beta CSV}_k+\boldsymbol{\gamma V}_k\\ &=\boldsymbol{CSV}_k+\boldsymbol{V}_k^s+\boldsymbol{KV}_k\end{aligned} \tag{3.40}$$

where $\boldsymbol{K}=\boldsymbol{\alpha}+\boldsymbol{\beta CS}+\boldsymbol{\gamma}$.

Following the same derivation in Section 3.2, the adjoint system is given by [7]

$$\boldsymbol{\lambda}_{k-1}=\boldsymbol{S}^T(\boldsymbol{x})\boldsymbol{C}^T(\boldsymbol{x})\boldsymbol{\lambda}_k+\boldsymbol{K}^T\boldsymbol{\lambda}_k-\boldsymbol{V}_k^{s,\lambda},\ \boldsymbol{\lambda}(T_m)=\boldsymbol{0} \tag{3.41}$$

where $\boldsymbol{V}_k^{s,\lambda}=\Delta t(\partial f/\partial \boldsymbol{V})_{k\Delta t}$ is the adjoint excitation. The one-way wave equation boundary operator is transposed and the expanded form of (3.41) is [7]

$$\begin{aligned}\boldsymbol{\lambda}_{k-1}&=\boldsymbol{S}^T\boldsymbol{C}^T\boldsymbol{\lambda}_k+\left(\boldsymbol{\alpha}^T+\boldsymbol{S}^T\boldsymbol{C}^T\boldsymbol{\beta}^T+\boldsymbol{\gamma}^T\right)\boldsymbol{\lambda}_k-\boldsymbol{V}_k^{s,\lambda}\\ &=\boldsymbol{S}^T\boldsymbol{C}^T\left(\boldsymbol{I}+\boldsymbol{\beta}^T\right)\boldsymbol{\lambda}_k+\left(\boldsymbol{\alpha}^T+\boldsymbol{\gamma}^T\right)\boldsymbol{\lambda}_k-\boldsymbol{V}_k^{s,\lambda}\\ &=\boldsymbol{S}^T\boldsymbol{C}^T\begin{bmatrix}\boldsymbol{I} & \beta_1^T\\ \boldsymbol{0} & \boldsymbol{0}\end{bmatrix}\begin{bmatrix}\boldsymbol{\lambda}_k^N\\ \boldsymbol{\lambda}_k^D\end{bmatrix}+\begin{bmatrix}\boldsymbol{0} & \gamma_1^T\\ \boldsymbol{0} & \alpha_1^T\end{bmatrix}\begin{bmatrix}\boldsymbol{\lambda}_k^N\\ \boldsymbol{\lambda}_k^D\end{bmatrix}-\boldsymbol{V}_k^{s,\lambda}.\end{aligned} \tag{3.42}$$

The original impulses and adjoint impulses are obtained using (3.38) and (3.42), respectively. Then, the sensitivity of the objective function (3.2) is obtained using (3.36).

3.6 SELF-ADJOINT *S*-PARAMETER SENSITIVITIES [5], [6]

For a structure with N_p ports, the traditional AVM requires N_p original simulations and additional N_p adjoint simulations to calculate derivatives of the *S*-parameter with respect to all optimizable parameters [14]. A self-adjoint method was developed in [5], [6] to estimate the *S*-parameter sensitivities with respect to all design parameters using only the original N_p simulations to calculating the *S*-parameters. In this section, self-adjoint *S*-parameter sensitivities of both lossless homogeneous and lossless nonhomogeneous structures are discussed.

3.6.1 Self-adjoint *S*-paramter Sensitivity for Lossless Homogeneous Structure [5]

We first discuss the self-adjoint *S*-parameter sensitivities for lossless, homogeneous, and isotropic problem. The excitation of the q^{th} port at the k^{th} time step is given by [14]

$$V_k^{s,j} = \frac{w}{\|w\|^2} E_q(j)\sin(2\pi f_o k\Delta t), q = 1,2,3,\ldots,N_p \tag{3.43}$$

where $E_q(j)$ is the transversal mode distribution at the j^{th} node of the q^{th} port, and j is the index of nodes in the cross-section of the q^{th} port. The excitation of each link at the j^{th}

node is determined by the vector $\boldsymbol{w}$.

The nodal scattering matrix of this problem is [5]

$$\boldsymbol{S}^{(j)T} = \boldsymbol{S}^{(j)} = \boldsymbol{S}^{(j)^{-1}} \tag{3.44}$$

Equation (3.44) implies that the eigenvectors of $\boldsymbol{S}^{(j)}$ have only real eigenvalues with absolute value of 1.0. The property of (3.44) applies also to the global scattering matrix:

$$\boldsymbol{S}^{T} = \boldsymbol{S} = \boldsymbol{S}^{-1}. \tag{3.45}$$

If we utilize the property of (3.45) and the symmetry of Johns matrix, the adjoint system of the AVM for TLM with Johns matrix (3.35) can be rewritten as [5]

$$\boldsymbol{\lambda}_{k-1} = \boldsymbol{S}\boldsymbol{C}\boldsymbol{\lambda}_k + \boldsymbol{S}\sum_{k'=k}^{N_t} \boldsymbol{J}(k'-k)\boldsymbol{\lambda}_{k'} - \boldsymbol{V}_k^{s,\lambda},\ \boldsymbol{\lambda}(T_m) = \boldsymbol{0}. \tag{3.46}$$

The original TLM simulation (3.26) of this case is then multiplied by the scattering matrix $\boldsymbol{S}$, [5]

$$\boldsymbol{S}\boldsymbol{V}_{k+1} = \boldsymbol{S}\boldsymbol{C}\boldsymbol{S}\boldsymbol{V}_k + \boldsymbol{S}\boldsymbol{V}_k^s + \boldsymbol{S}\sum_{k'=0}^{k} \boldsymbol{J}(k-k')\boldsymbol{V}_{k'}^r. \tag{3.47}$$

Then, (3.47) can be rewritten by substituting $\boldsymbol{V}_k^r = \boldsymbol{S}\boldsymbol{V}_k$,

$$\boldsymbol{V}_{k+1}^r = \boldsymbol{S}\boldsymbol{C}\boldsymbol{V}_k^r + \boldsymbol{V}_k^{s,r} + \boldsymbol{S}\sum_{k'=0}^{k} \boldsymbol{J}(k-k')\boldsymbol{V}_{k'}^r \tag{3.48}$$

where $\boldsymbol{V}_k^{s,r} = \boldsymbol{S}\boldsymbol{V}_k^s$. Equation (3.48) is the original system of lossless, homogeneous, and isotropic structure.

We notice that (3.46) and (3.48) have the same form except that (3.46) is running backward in time while (3.48) is running forward. If the adjoint excitation $\boldsymbol{V}_k^{s,\lambda}$ and $\boldsymbol{V}_k^{s,r}$ can be related, then the adjoint impulses $\boldsymbol{\lambda}_k$ can be predicted from original impulses $\boldsymbol{V}_k^r$.

The excited transversal electric field at the j^{th} node of the q^{th} port at the k^{th} time step is [14]

$$E_k^{s,j} = \boldsymbol{a}^T \boldsymbol{V}_k^{s,j} \tag{3.49}$$

where the vector $\boldsymbol{a}$ relates the incident impulses to the observed electric field component. For a lossless homogeneous medium, the vector $\boldsymbol{w}$ and the vector $\boldsymbol{a}$ are equal. The field components are obtained from incident impulses as follows [14]:

$$\begin{array}{l} E_x = \boldsymbol{a}_{ex}^T \boldsymbol{V},\ \ E_y = \boldsymbol{a}_{ey}^T \boldsymbol{V},\ \ E_z = \boldsymbol{a}_{ez}^T \boldsymbol{V}, \\ H_x = \boldsymbol{a}_{hx}^T \boldsymbol{V},\ \ H_y = \boldsymbol{a}_{hy}^T \boldsymbol{V},\ \ H_z = \boldsymbol{a}_{hz}^T \boldsymbol{V}. \end{array} \tag{3.50}$$

For Johns matrix SCN, the weighting vectors in (3.50) is [5]

$$\begin{array}{l} \boldsymbol{a}_{ex} = q_e \begin{bmatrix} 1 & 1 & 0 & 0 & 0 & 0 & 0 & 0 & 1 & 0 & 0 & 1 \end{bmatrix}^T, \\ \boldsymbol{a}_{ey} = q_e \begin{bmatrix} 0 & 0 & 1 & 1 & 0 & 0 & 0 & 1 & 0 & 0 & 1 & 0 \end{bmatrix}^T, \\ \boldsymbol{a}_{ez} = q_e \begin{bmatrix} 0 & 0 & 0 & 0 & 1 & 1 & 1 & 0 & 0 & 1 & 0 & 0 \end{bmatrix}^T, \\ \boldsymbol{a}_{hx} = q_h \begin{bmatrix} 0 & 0 & 0 & 1 & -1 & 0 & 1 & -1 & 0 & 0 & 0 & 0 \end{bmatrix}^T, \\ \boldsymbol{a}_{hy} = q_h \begin{bmatrix} 0 & -1 & 0 & 0 & 0 & 1 & 0 & 0 & 1 & -1 & 0 & 0 \end{bmatrix}^T, \\ \boldsymbol{a}_{hz} = q_h \begin{bmatrix} 1 & 0 & -1 & 0 & 0 & 0 & 0 & 0 & 0 & 0 & 1 & -1 \end{bmatrix}^T, \end{array} \tag{3.51}$$

where $q_e = 0.5/\Delta l$ and $q_h = 0.5/\left(\Delta l \cdot Z_o\right)$. Z_o is the characteristic impedance of the SCN link. The vectors $\boldsymbol{a}_{ex}$, $\boldsymbol{a}_{ey}$, and $\boldsymbol{a}_{ez}$ are the eigenvectors of the matrix $\boldsymbol{S}^{(j)}$ with an eigenvalue of 1.0 and $\boldsymbol{a}_{hx}$, $\boldsymbol{a}_{hy}$, and $\boldsymbol{a}_{hz}$ are the eigenvectors with an eigenvalue of -1.0.

One of the weighting vectors in (3.51) is chosen as $\boldsymbol{a}$, then the q^{th} port of the original problem is excited by (3.52) [5]

$$\boldsymbol{V}_{k}^{s,j}=\frac{\boldsymbol{a}}{\|\boldsymbol{a}\|^{2}}E_{q}(j)h_{o}(k\Delta t),q=1,2,3,...,N_{p}. \tag{3.52}$$

According $\boldsymbol{V}_{k}^{s,r}=\boldsymbol{S}\boldsymbol{V}_{k}^{s}$,

$$\boldsymbol{V}_{k,j}^{s,r}=\boldsymbol{S}^{(j)}\frac{\boldsymbol{a}}{\|\boldsymbol{a}\|^{2}}E_{q}(j)h_{o}(k\Delta t)=\mu\frac{\boldsymbol{a}}{\|\boldsymbol{a}\|^{2}}E_{q}(j)h_{o}(k\Delta t) \tag{3.53}$$

where μ is the eigenvalue of selected $\boldsymbol{a}$, parameter μ is 1.0 or μ is -1.0 [5].

The adjoint excitation at the j^{th} node of the p^{th} port as a function of adjoint time variable τ is given by [14]

$$\boldsymbol{V}^{s,\lambda}(n\Delta\tau)=\frac{\boldsymbol{a}}{\|\boldsymbol{a}\|^{2}}E_{q}(j)h(n\Delta\tau). \tag{3.54}$$

If we set $h(n\Delta\tau)=h_{o}(k\Delta t)$, then

$$\lambda(\tau)=\frac{-1}{\mu}\boldsymbol{V}^{R}(t)\text{ or }\boldsymbol{\lambda}_{N_t-k}=\frac{-1}{\mu}\boldsymbol{V}_{k}^{R}. \tag{3.55}$$

We conclude that the adjoint impulses obtained by exciting the q^{th} port with excitation (3.54) can be derived from the vector $\boldsymbol{V}_{k}^{r}$ obtained by original simulation (3.48) excited at the same port by (3.53). Therefore, extra adjoint excitations are not necessary in this case. The *S*-parameter sensitivities are thus be computed using only the original N_{p} simulations.

3.6.2 Self-adjoint *S*-paramter Sensitivity for Lossless Nonhomogeneous Structure [6]

For a lossless nonhomogeneous TLM problem with Johns' SCN, the nodal scattering matrix satisfies the properties [15]

$$\boldsymbol{S}^{(j)T}\boldsymbol{Y}^{(j)}\boldsymbol{S}^{(j)}=\boldsymbol{Y}^{(j)} \text{ and } \boldsymbol{S}^{(j)}=\boldsymbol{S}^{(j)^{-1}} \tag{3.56}$$

where $\boldsymbol{Y}^{(j)}$ is a diagonal matrix whose elements are the normalized admittances of the links at the j^{th} node. Again the eigenvectors of $\boldsymbol{S}^{(j)}$ have only real eigenvalues with an absolute value of 1.0. Applying the property in (3.56) to the global scattering matrix [6], we get

$$\boldsymbol{S}^{T}\boldsymbol{Y}\boldsymbol{S}=\boldsymbol{Y} \text{ and } \boldsymbol{S}=\boldsymbol{S}^{-1} \tag{3.57}$$

where $\boldsymbol{Y}$ is a block diagonal matrix whose j^{th} diagonal component is $\boldsymbol{Y}^{(j)}$. From [6], we know that

$$\boldsymbol{CY}=\boldsymbol{YC},\ \boldsymbol{Y}^{-1}\boldsymbol{J}=y_o^{-1}\boldsymbol{J} \text{ and} \tag{3.58}$$

$$\boldsymbol{J}^{T}\boldsymbol{Y}=y_o\boldsymbol{J}^{T}, \tag{3.59}$$

where y_o is the normalized admittance of the SCN links.

Two cases are discussed in [6]: the generalized Johns' node and modified node with a symmetrical scattering matrix. We first address the generalized Johns' node.

For the generalized Johns' node, the adjoint system (3.35) is modified using (3.57), (3.58), and (3.59) [6],

$$\boldsymbol{\eta}_{k-1}=\boldsymbol{SC}\boldsymbol{\eta}_{k}+\boldsymbol{S}\sum_{k'=k}^{N_t}\boldsymbol{J}(k'-k)\boldsymbol{\eta}_{k'}-\boldsymbol{V}_{k}^{s,\eta} \tag{3.60}$$

where $\boldsymbol{\eta}_k=\boldsymbol{Y}^{-1}\boldsymbol{\lambda}_k$ is called transformed adjoint variable, and $\boldsymbol{V}_k^{s,\eta}=\boldsymbol{Y}^{-1}\boldsymbol{V}_k^{s,\lambda}$ is the excitation of the transformed adjoint problem.

For the original simulation, we multiply both sides of (3.26) by the scattering matrix $\boldsymbol{S}$, and we set $\boldsymbol{\gamma}_{k+1} = \boldsymbol{S}\boldsymbol{V}_k$ and $\boldsymbol{V}_k^{s,\gamma} = \boldsymbol{S}\boldsymbol{V}_k^{s}$ and therefore

$$\boldsymbol{\gamma}_{k+1} = \boldsymbol{S}\boldsymbol{C}\boldsymbol{\gamma}_k + \boldsymbol{S}\sum_{k'=0}^{k}\boldsymbol{J}(k-k')\boldsymbol{\gamma}_{k'} + \boldsymbol{V}_k^{s,\gamma}. \tag{3.61}$$

Equations (3.60) and (3.61) are in the same form except that (3.60) is running backward in time while (3.61) is running forward in time. Again, if the two excitations can be related, the adjoint vector can be predicted from the original vector.

Equation (3.51) is re-derived for the Johns' node in a lossless nonhomogeneous TLM [6],

$$\begin{aligned}
\boldsymbol{a}_{ex} &= q_e\begin{bmatrix}1 & 1 & 0 & 0 & 0 & 0 & 0 & 0 & 1 & 0 & 0 & 1 & Y & 0 & 0 & 0 & 0 & 0\end{bmatrix}^T, \\
\boldsymbol{a}_{ey} &= q_e\begin{bmatrix}0 & 0 & 1 & 1 & 0 & 0 & 0 & 1 & 0 & 0 & 1 & 0 & 0 & Y & 0 & 0 & 0 & 0\end{bmatrix}^T, \\
\boldsymbol{a}_{ez} &= q_e\begin{bmatrix}0 & 0 & 0 & 0 & 1 & 1 & 1 & 0 & 0 & 1 & 0 & 0 & 0 & 0 & Y & 0 & 0 & 0\end{bmatrix}^T, \\
\boldsymbol{a}_{hx} &= q_h\begin{bmatrix}0 & 0 & 0 & 1 & -1 & 0 & 1 & -1 & 0 & 0 & 0 & 0 & 0 & 0 & 0 & Z & 0 & 0\end{bmatrix}^T, \\
\boldsymbol{a}_{hy} &= q_h\begin{bmatrix}0 & -1 & 0 & 0 & 0 & 1 & 0 & 0 & 1 & -1 & 0 & 0 & 0 & 0 & 0 & 0 & Z & 0\end{bmatrix}^T, \\
\boldsymbol{a}_{hz} &= q_h\begin{bmatrix}1 & 0 & -1 & 0 & 0 & 0 & 0 & 0 & 0 & 0 & 1 & -1 & 0 & 0 & 0 & 0 & 0 & Z\end{bmatrix}^T,
\end{aligned} \tag{3.62}$$

where $Y = 4(\varepsilon_r - 1)$, $Z = 4(\mu_r - 1)$, $q_e = 2/(\Delta l(Y+4))$, and $q_h = 2/(\Delta l \cdot Z_o(Z+4))$.

The excitation of the transformed adjoint problem (3.60) is derived in [6]

$$\boldsymbol{V}_{k,j}^{s,\eta} = \boldsymbol{Y}^{(j)}\frac{\boldsymbol{a}}{\|\boldsymbol{a}\|^2}E_p(j)h_a(k\Delta\tau) = \frac{\alpha^{(j)}}{\|\boldsymbol{a}\|^2}\boldsymbol{e}E_p(j)h_a(k\Delta\tau) \tag{3.63}$$

where $\boldsymbol{e}$ is a eigenvector of the nodal scattering matrix, and its elements are 0 and 1 corresponding to the observed field component. On the other hand, the excitation of the transformed original problem at the p^{th} port is [6]

$$\boldsymbol{V}_{k,j}^{s,\gamma} = \boldsymbol{S}^{(j)}\boldsymbol{e}E_p(j)h_o(k\Delta t) = \mu\boldsymbol{e}E_p(j)h_o(k\Delta t). \tag{3.64}$$

If we set $h_a(k\Delta\tau) = h_o(k\Delta t)$, comparing (3.63) and (3.64), we have [6]

$$\eta(\tau) = \frac{\alpha\mu}{\|\boldsymbol{a}\|^2}\gamma(t) \text{ or } \eta_{N_t-k} = \frac{\alpha\mu}{\|\boldsymbol{a}\|^2}\gamma_k. \tag{3.65}$$

Because $\boldsymbol{\eta}_k = \boldsymbol{Y}^{-1}\boldsymbol{\lambda}_k$, (3.65) is simplified to

$$\lambda_{N_t-k} = \frac{\alpha\mu}{\|\boldsymbol{a}\|^2}\boldsymbol{Y}\gamma_k. \tag{3.66}$$

We conclude that for the generalized Johns' node, the adjoint impulses obtained from (3.60) with excitation (3.63) can be derived from the original simulation (3.61) excited with (3.64). Therefore, the *S*-parameter sensitivities are thus be computed by only N_{p} original simulations.

The modified node with a symmetrical scattering matrix has the properties of a symmetric and unitary nodal scattering matrix. Following similar derivation, the original simulation is the same as (3.61), and adjoint simulation has the same form of (3.46) [6]. Again, the adjoint simulation and original simulation are the same except that one is running backward while the other is running forward.

Equation (3.51) is re-derived for the modified SCN [6],

$$
\begin{aligned}
\boldsymbol{a}_{ex} &= q_e\begin{bmatrix}1 & 1 & 0 & 0 & 0 & 0 & 0 & 0 & 1 & 0 & 0 & 1 & \sqrt{Y} & 0 & 0 & 0 & 0 & 0\end{bmatrix}^T, \\
\boldsymbol{a}_{ey} &= q_e\begin{bmatrix}0 & 0 & 1 & 1 & 0 & 0 & 0 & 1 & 0 & 0 & 1 & 0 & 0 & \sqrt{Y} & 0 & 0 & 0 & 0\end{bmatrix}^T, \\
\boldsymbol{a}_{ez} &= q_e\begin{bmatrix}0 & 0 & 0 & 0 & 1 & 1 & 1 & 0 & 0 & 1 & 0 & 0 & 0 & 0 & \sqrt{Y} & 0 & 0 & 0\end{bmatrix}^T, \\
\boldsymbol{a}_{hx} &= q_h\begin{bmatrix}0 & 0 & 0 & 1 & -1 & 0 & 1 & -1 & 0 & 0 & 0 & 0 & 0 & 0 & 0 & \sqrt{Z} & 0 & 0\end{bmatrix}^T, \\
\boldsymbol{a}_{hy} &= q_h\begin{bmatrix}0 & -1 & 0 & 0 & 0 & 1 & 0 & 0 & 1 & -1 & 0 & 0 & 0 & 0 & 0 & 0 & \sqrt{Z} & 0\end{bmatrix}^T, \\
\boldsymbol{a}_{hz} &= q_h\begin{bmatrix}1 & 0 & -1 & 0 & 0 & 0 & 0 & 0 & 0 & 0 & 1 & -1 & 0 & 0 & 0 & 0 & 0 & \sqrt{Z}\end{bmatrix}^T,
\end{aligned}
\tag{3.69}
$$

where $Y = 4(\varepsilon_r - 1)$, $Z = 4(\mu_r - 1)$, $q_e = 2/(\Delta l(Y+4))$, and $q_h = 2/\left(\Delta l \cdot Z_o(Z+4)\right)$.

The original excitation is (3.52), so the transformed excitation is

$$
\boldsymbol{V}_{k,j}^{s,r} = \boldsymbol{S}^{(j)}\frac{\boldsymbol{a}}{\|\boldsymbol{a}\|^2}E_q(j)h_o(k\Delta t) = \mu\frac{\boldsymbol{a}}{\|\boldsymbol{a}\|^2}E_q(j)h_o(k\Delta t)
\tag{3.70}
$$

where μ is the eigenvalue of selected $\boldsymbol{a}$, and μ is 1.0 or μ is -1.0 [6]. Comparing with the excitation of the adjoint system (3.54), if we set $h_a(k\Delta\tau) = h_o(k\Delta t)$, the transformation between the adjoint impulses and the reflected impulses of the original simulation is given by [6]

$$
\lambda(\tau) = \frac{-1}{\mu}\gamma(t) \text{ or } \boldsymbol{\lambda}_{N_t-k} = \frac{-1}{\mu}\boldsymbol{\gamma}_k.
\tag{3.71}
$$

It follows that the adjoint impulses can be obtained from the transformation (3.71) and no adjoint simulations are needed for *S*-parameter sensitivities.

3.7 SENSITIVITIES ANALYSIS EXPLOITING RUBBER CELLS [8]

The TLM method simulates the EM fields by a network of transmission lines with

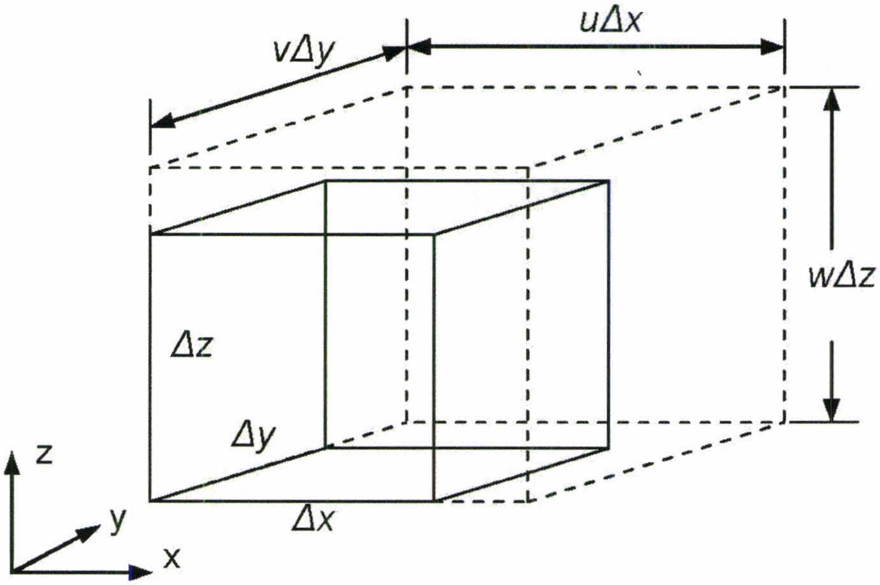

Figure 3.5: A TLM cell stretched by factors *u*, *v* and *w*.[11]

a discretized model in both space and time. The boundaries in SCN are placed half-way between nodes, so the dimensions can only be integer multiples of the mesh size. Huilian *et al.* [11] developed an approach to model boundaries at irregular locations with the TLM SCN. The truncated boundary cells are modeled through modifying local tensor properties rather than changing the cell size and shape.

Consider a TLM cell with size $\Delta x \times \Delta y \times \Delta z$, the material properties of the cell is characterized by diagonal permittivity and permeability tensors [11]:

$$\vec{\varepsilon} = \begin{vmatrix} \varepsilon_{xx} & 0 & 0 \\ 0 & \varepsilon_{yy} & 0 \\ 0 & 0 & \varepsilon_{zz} \end{vmatrix} \text{ and } \vec{\mu} = \begin{vmatrix} \mu_{xx} & 0 & 0 \\ 0 & \mu_{yy} & 0 \\ 0 & 0 & \mu_{zz} \end{vmatrix}. \tag{3.72}$$

Figure 3.5 shows a deformed cell with small stretch factors u, v, and w in x, y, and z directions, respectively. Without changing the cell capacitance and inductance, the modified permittivity and permeability tensors of such a cell are [11]

$$\begin{aligned}&\varepsilon_{xx}^{'}=\frac{vw}{u}\varepsilon_{xx},\ \varepsilon_{yy}^{'}=\frac{uw}{v}\varepsilon_{yy},\ \varepsilon_{zz}^{'}=\frac{uv}{w}\varepsilon_{zz},\\&\mu_{xx}^{'}=\frac{vw}{u}\mu_{xx},\ \mu_{yy}^{'}=\frac{uw}{v}\mu_{yy},\ \mu_{zz}^{'}=\frac{uv}{w}\mu_{zz}.\end{aligned}\tag{3.73}$$

Now we have the modified permittivity and permeability tensors ready. The overall scattering matrix is obtained using the general formula in [12]. According to the above approach, any off-grid discontinuity can be modeled by on-grid discontinuity and surrounding rubber cells with modified tensors. Hence, the small perturbation of a discontinuity is actually the perturbation in the surrounding rubber cells. This perturbation can be modeled by analytical derivative of the global system matrix $\boldsymbol{A}$ with respect to the tensor properties [8]

$$\frac{\partial \boldsymbol{A}}{\partial x_i}=\frac{\partial \boldsymbol{A}}{\partial u}\frac{\Delta u}{\Delta x_i}+\frac{\partial \boldsymbol{A}}{\partial v}\frac{\Delta v}{\Delta x_i}+\frac{\partial \boldsymbol{A}}{\partial w}\frac{\Delta w}{\Delta x_i}.\tag{3.72}$$

Using the chain rule, the derivative of the system matrix $\boldsymbol{A}$ with respect to the scaling factors is obtained [8]

$$\begin{aligned}
\frac{\partial \boldsymbol{A}}{\partial u} &= \frac{\partial \boldsymbol{A}}{\partial \varepsilon_{xx}}\frac{\partial \varepsilon_{xx}}{\partial u} + \frac{\partial \boldsymbol{A}}{\partial \varepsilon_{yy}}\frac{\partial \varepsilon_{yy}}{\partial u} + \frac{\partial \boldsymbol{A}}{\partial \varepsilon_{zz}}\frac{\partial \varepsilon_{zz}}{\partial u} + \frac{\partial \boldsymbol{A}}{\partial \mu_{xx}}\frac{\partial \mu_{xx}}{\partial u} + \frac{\partial \boldsymbol{A}}{\partial \mu_{yy}}\frac{\partial \mu_{yy}}{\partial u} + \frac{\partial \boldsymbol{A}}{\partial \mu_{zz}}\frac{\partial \mu_{zz}}{\partial u},\\
\frac{\partial \boldsymbol{A}}{\partial v} &= \frac{\partial \boldsymbol{A}}{\partial \varepsilon_{xx}}\frac{\partial \varepsilon_{xx}}{\partial v} + \frac{\partial \boldsymbol{A}}{\partial \varepsilon_{yy}}\frac{\partial \varepsilon_{yy}}{\partial v} + \frac{\partial \boldsymbol{A}}{\partial \varepsilon_{zz}}\frac{\partial \varepsilon_{zz}}{\partial v} + \frac{\partial \boldsymbol{A}}{\partial \mu_{xx}}\frac{\partial \mu_{xx}}{\partial v} + \frac{\partial \boldsymbol{A}}{\partial \mu_{yy}}\frac{\partial \mu_{yy}}{\partial v} + \frac{\partial \boldsymbol{A}}{\partial \mu_{zz}}\frac{\partial \mu_{zz}}{\partial v},\\
\frac{\partial \boldsymbol{A}}{\partial w} &= \frac{\partial \boldsymbol{A}}{\partial \varepsilon_{xx}}\frac{\partial \varepsilon_{xx}}{\partial w} + \frac{\partial \boldsymbol{A}}{\partial \varepsilon_{yy}}\frac{\partial \varepsilon_{yy}}{\partial w} + \frac{\partial \boldsymbol{A}}{\partial \varepsilon_{zz}}\frac{\partial \varepsilon_{zz}}{\partial w} + \frac{\partial \boldsymbol{A}}{\partial \mu_{xx}}\frac{\partial \mu_{xx}}{\partial w} + \frac{\partial \boldsymbol{A}}{\partial \mu_{yy}}\frac{\partial \mu_{yy}}{\partial w} + \frac{\partial \boldsymbol{A}}{\partial \mu_{zz}}\frac{\partial \mu_{zz}}{\partial w}.
\end{aligned} \tag{3.73}$$

The system matrix $\boldsymbol{A}$ is an analytical function of scattering matrix $\boldsymbol{S}$ while $\boldsymbol{S}$ is an analytical function of tensor permittivities, and permeabilities and the tensors are analytical functions of the stretch factors (3.71). Therefore, the derivatives of the system matrix $\boldsymbol{A}$ with respect to stretch factors (3.73) can be analytical calculated. Equation (3.72) can be thus computed using (3.73). Then, the sensitivity of the objective function $\boldsymbol{F}$ is obtained using (3.74)

$$\frac{\partial F}{\partial x_i} \approx \frac{\partial^e F}{\partial x_i} - \Delta t \sum_k \boldsymbol{\lambda}_k^T \frac{\Delta \boldsymbol{A}_i}{\Delta x_i} \boldsymbol{V}_k. \tag{3.74}$$

The implementation of this approach is the same as the analytical approach of dielectric discontinuities discussed in section 3.2.2. The advantages of this technique are the ability to model the off-grid discontinuities and accurately calculate its sensitivities.

3.8 CONCLUSIONS

In this chapter, an up-to-date review of AVM applications for different time-domain TLM problems is presented. The AVM algorithm of metallic discontinuities and dielectric discontinuities in both 2-D and 3-D cases are introduced separately. The

AVM for waveguide problems with wide-band Johns matrix boundaries, self-adjoint *S*-parameter sensitivities for lossless homogeneous and lossless nonhomogeneous TLM problems, the AVM for planar structures using first-order one-way wave equation boundaries, and conformal TLM based on the rubber cell implementation are all presented. The AVM accurately estimates the sensitivities of all discussed problems using at most two simulations of the original system and the adjoint system regardless the number of optimizable parameters.

REFERENCES

[1] M.H. Bakr and N.K. Nikolova, "An adjoint variable method for time-domain transmission-line modeling with fixed structured grids," *IEEE Trans. Microwave Theory Tech.*, vol. 52, NO. 2, pp554-559, Feb. 2004.

[2] M.H. Bakr and N.K. Nikolova, "An adjoint variable method for time-domain TLM with wide-band Johns matrix boundaries," *IEEE Transactions on Microwave Theory and Techniques*, vol. 52, pp. 678-685, 2004.

[3] P.A.W. Basl, M.H. Bakr, and N.K. Nikolova, "Efficient estimation of sensitivities in TLM with dielectric discontinuities," *IEEE Trans. Microwave Wireless Comp.,* vol. 15, pp.89-91, Feb. 2005.

[4] P.A.W. Basl, M.H. Bakr, and N.K. Nikolova, "An AVM technique for 3-D TLM with symmetric condensed nodes," *IEEE Trans. Microwave Wireless Componnets letters.,* vol. 15, pp.618-620, 2005.

[5] M.H. Bakr, N.K. Nikolova, and P.A.W. Basl, "Self-adjoint S-parameter sensitivities for lossless homogeneous TLM problems,"*International Journal of Numerical Modelling: Electric Networks, Devices and Fields,* vol. 18, pp. 441-455, 2005.

[6] P.A.W. Basl, M.H. Bakr, and N.K. Nikolova, "The theory of self-adjoint S-parameter sensitivities for lossless nonhomogeneous TLM problems," *IEEE Transactions on Microwave Theory and Techniques*, 2006.

[7] P.A.W. Basl, M.H. Bakr, and N.K. Nikolova, "Time-domain sensitivity analysis of planar structures using first-order one-way wave equation boundaries," in *International Journal of Numerical Modelling: Electric Networks, Devices and Fields:* John Wiley and Sons Ltd, Chichester, West Sussex, PO 19 8SQ, United Kingdom, 2006.

[8] P.A.W. Basl, M.H. Bakr, and N.K. Nikolova, "Efficient TLM sensitivity analysis exploiting rubber cells," *Computational Electromagnetics Research Laboratory*, McMaster Univ., Canada, 2008.

[9] Y.S. Chung, C. Cheon, I.H. Park, and S.Y. Hahn, "Optimal design method for microwave device using time domain method and design sensitivity analysis-Part II: FDTD case," *IEEE Trans. Magn.*, vol. 37, pp. 3255-3259, Sept. 2001.

[10] N. K. Eswarappa, G. I. Costache, and W. J. R. Hoefer, "Transmission line matrix modeling of dispersive wide-band absorbing boundaries with time-domain diakoptics for S-parameter extraction," *IEEE Trans. Microwave Theory Tech.*, vol. 38, pp. 379–386, Apr. 1990.

[11] D. Huilian, S. Poman, and W. J. R. Hoefer, "Cells with tensor properties for conformal TLM boundary modeling," *2006 IEEE MTT-S International Microwave Symposium*, San Francisco, CA, USA, 2006, vol. 11, pp. 157-160.

[12] P.B. Johns, "A symmetrical condensed node for the TLM method," *IEEE Trans. Microwaves Theory Tech.*, vol. 35, no. 4, pp. 370-377, April 1987.

[13] C. Eswarappa and W.J.R. Hoefer, "One-way equation absorbing boundary conditions for 3-D TLM analysis of planar and quasi-planar structures," *IEEE Trans. Microw. Theory and Tech.*, vol. 42, pp. 1669-1677, 1994.

[14] M.H. Bakr and N.K. Nikolova, "Efficient estimation of adjoint-variable S-parameter sensitivities with time domain TLM," *International Journal of Numerical Modelling: Electronic Networks, Device and Fields*, vol. 18, pp. 171-187, 2005.

[15] C. Christopoulos, *The transmission-line modeling method: TLM.* Oxford: Oxford University Press, 1995.

CHAPTER 4

SENSITIVITIES OF TIME-DOMAIN RESPONSES USING THE AVM

4.1 INTRODUCTION

As explained in previous chapters, the AVM approach efficiently estimates the response sensitivities with respect to all the design parameters. This approach was already utilized for estimating the sensitivity of scalar objective functions [1]-[6] and frequency domain responses [7], [8]. However, the gradient of time-domain responses using AVM was not addressed. This type of derivatives may have applications in many fields. Nowadays, microwave imaging is an efficient method for tumor detection. The derivative information of time domain responses is appropriate for this kind of problems.

We develop a new adjoint-based algorithm to estimate the sensitivities of time domain response. These sensitivities can then be used in solving inverse problems [9]-[11] where the dielectric properties, dimensions, and location of objects/tumors are estimated.

In this chapter, we derive the mathematical expression for our new AVM approach. This approach will be illustrated through the estimation of the sensitivities of objective function with respect to dimensions, position, and the dielectric properties of the discontinuities in a number of examples.

4.2 SENSITIVITIES OF TIME-DOMAIN RESPONSE USING AVM [12],[13]

Our approach aims at extending the AVM algorithm in [1] to estimate the sensitivities of complete time domain responses. The problem can be formulated as a convolution of the objective function's kernal in (3.2) with a discrete time delta function. The discrete delta function is defined as:

$$\delta[k]=\begin{cases}1, & k=0\\ 0, & k\neq 0\end{cases}. \tag{4.1}$$

The objective function, which may be any field component, at the m^{th} time step F_m can thus be expressed by:

$$\begin{aligned}F_m &= \sum_k F(\boldsymbol{x},\boldsymbol{V},k)\delta[m-k]\\ &= F(\boldsymbol{x},\boldsymbol{V},m)\\ &= \frac{1}{\Delta t}\int_0^{T_{\max}} F(\boldsymbol{x},\boldsymbol{V},\tau)\delta(t-\tau)d\tau\end{aligned} \tag{4.2}$$

where F is the kernel, and $T_{\max}$ is the maximum simulation time. The function (4.2) is the continuous time equivalent of the discrete delta function. The index m is the time step index at which the objective function is calculated. The objective function (4.2) gives the field of interest at the m^{th} time step. The analytical derivative of this time-dependent objective function with respect to the i^{th} parameter is given by

$$\begin{aligned}\frac{\partial F_m}{\partial x_i} &= \frac{1}{\Delta t}\frac{\partial^e F_m}{\partial x_i} + \frac{1}{\Delta t}\int_0^{T_{\max}} \frac{\partial F(\boldsymbol{x},\boldsymbol{V},\tau)}{\partial x_i}\delta(t-\tau)d\tau \\ &= \frac{1}{\Delta t}\frac{\partial^e F_m}{\partial x_i} + \frac{1}{\Delta t}\int_0^{T_{\max}} \left(\frac{\partial F(\boldsymbol{x},\boldsymbol{V},\tau)}{\partial \boldsymbol{V}}\delta(t-\tau)\right)^T \frac{\partial \boldsymbol{V}}{\partial x_i}d\tau.\end{aligned} \tag{4.3}$$

Alternatively, the AVM approach can be applied to estimate the sensitivities in (4.3). Following the same steps of (3.4) to (3.11), the adjoint vector $\boldsymbol{\lambda}$ is introduced and we get

$$\frac{\partial \boldsymbol{\lambda}^T}{\partial t} + \boldsymbol{\lambda}^T\left(\boldsymbol{A}+\Delta\boldsymbol{A}_i\right) = \frac{\partial F^T(\boldsymbol{x},\boldsymbol{V},\tau)}{\partial \boldsymbol{V}}\delta(t-\tau). \tag{4.4}$$

After expanding the system matrix (4.4), we have the backward running discrete time adjoint simulation

$$\boldsymbol{\lambda}_{m,k-1} = \boldsymbol{S}^T(\boldsymbol{x}+\Delta x_i e_i)\boldsymbol{C}^T(\boldsymbol{x}+\Delta x_i e_i)\boldsymbol{\lambda}_{m,k} - \boldsymbol{V}_{m,k}^{s,\lambda},\ \boldsymbol{\lambda}(T_{\max}) = \boldsymbol{0} \tag{4.5}$$

where $\boldsymbol{V}_{m,k}^{s,\lambda} = \Delta t(\partial F[k]/\partial \boldsymbol{V})\delta[m-k]$ is the adjoint excitation at the k^{th} time step for the sensitivity of the field at the m^{th} time step $\partial F_m/\partial x_i$. Since the perturbation of each parameter is small and does not affect the incident impulses significantly, the adjoint impulses are approximated by the values of the corresponding incident impulses for the unperturbed adjoint problem [1]

$$\boldsymbol{\lambda}_{m,k-1} = \boldsymbol{S}^T(\boldsymbol{x})\boldsymbol{C}^T(\boldsymbol{x})\boldsymbol{\lambda}_{m,k} - \boldsymbol{V}_{m,k}^{s,\lambda},\ \boldsymbol{\lambda}(T_{\max}) = \boldsymbol{0}. \tag{4.6}$$

Combining (4.2), (3.11), and (4.3), the sensitivity of F_m with respect to i^{th} parameter can be expressed as

$$\begin{aligned} \frac{\partial F_m}{\partial x_i} &= \frac{1}{\Delta t}\frac{\partial^e F_m}{\partial x_i} - \frac{1}{\Delta t}\int_0^{T_{\max}} \lambda_m^T \frac{\Delta A_i}{\Delta x_i} V_m dt \\ &\approx \frac{1}{\Delta t}\frac{\partial^e F_m}{\partial x_i} - \sum_k \lambda_{m,k}^T \frac{\Delta A_i}{\Delta x_i} V_{m,k} \\ &= \frac{1}{\Delta t}\frac{\partial^e F_m}{\partial x_i} - \sum_m \lambda_{m,k}^T \eta_{m,k} \end{aligned} \tag{4.7}$$

where $\lambda_{m,k}$ and $\eta_{m,k} = (\Delta A_i/\Delta x_i)V_{m,k}$ are the vectors of adjoint impulses and original impulses at the k^{th} time step for the sensitivity at the m^{th} time step, respectively.

Comparing (4.7) with (3.15), the expression are different in two main aspects. The first aspect is that (4.7) gives a different sensitivity value at different times by changing the value of m while (3.15) returns only one sensitivity value. The second difference is related to the adjoint excitation. The adjoint excitation in this algorithm is equal to $V_{m,k}^{s,\lambda} = \Delta t(\partial F[k]/\partial V)\delta[m-k]$ while the adjoint excitation of (3.15) is $V_k^{s,\lambda} = \Delta t(\partial G(k\Delta t)/\partial V)$. Therefore, the vector of $\lambda_{m,k}$ here is different for each value of m as the excitation is shifted. The vector of η is the same in both (3.15) and (4.7).

4.3 ALGORITHM FOR DETERMINATION OF VECTOR OF λ

In this algorithm, the adjoint excitation is the multiplication of $\partial G(t)/\partial V$ and the discrete time delta function:

$$V_{m,k}^{s,\lambda} = \Delta t \frac{\partial F[k]}{\partial V}\delta[m-k]. \tag{4.8}$$

Equation (4.8) has a value of zero everywhere except at $k = m$. To clearly show the relationship among the adjoint excitations for different values of m, we demonstrate the equations for $m = n_1$ and $m = n_2$,

$$\begin{aligned} &for\ m = n_1,\ \ V_{m,k}^{s,\lambda} = \Delta t \frac{\partial F[k]}{\partial \boldsymbol{V}} \delta[n_1 - k] \neq \mathbf{0} \text{ only at } k = n_1, \\ &for\ m = n_2,\ \ V_{m,k}^{s,\lambda} = \Delta t \frac{\partial F[k]}{\partial \boldsymbol{V}} \delta[n_2 - k] \neq \mathbf{0} \text{ only at } k = n_2. \end{aligned} \tag{4.9}$$

Equation (4.9) shows that the adjoint excitation (4.8) is excited only at *k*=*m* and the magnitude of (4.9) is different for different *m*. Therefore, the relationship between the adjoint responses λ_m involves both a scaling in magnitude and a shifting in time. The scaling is because of different magnitude of $\partial F[k]/\partial \boldsymbol{V}$ for different values of *k*. The time shift is due to the adjoint excitation is only nonzero at $k = m$.

If the vector λ_m is different at each *m*, then the memory requirement for storage would be extremely large if we were to estimate the sensitivities of the complete time response. To solve this problem we define $F(t) = E(t)$, the desired field component. This field is observed at only one node in the computational domain. Utilizing (2.15) and (2.26), we get for both the 2-D and 3-D cases

$$\begin{aligned} &\text{2-D:}\ \ \frac{\partial F(k\Delta t)}{\partial \boldsymbol{V}} = \frac{\partial E(t)}{\partial \boldsymbol{V}} = \frac{2}{y}\begin{bmatrix} 1 & 1 & 1 & 1 & y_o \end{bmatrix}, \\ &\text{3-D:}\ \ \frac{\partial F(k\Delta t)}{\partial \boldsymbol{V}} = \frac{\partial E(t)}{\partial \boldsymbol{V}} = -\frac{2}{\Delta l(4+\hat{Y})}\begin{bmatrix} 1 & 1 & 1 & 1 & \hat{Y} \end{bmatrix}. \end{aligned} \tag{4.10}$$

We notice that (4.10) is not dependent on time. It's a constant vector for any *k*. It follows that there is no need of scaling in magnitude to calculate the field response at different time instants. We just need to simulate the adjoint system only once for a specific time step *m* and obtain the corresponding adjoint response λ through (4.6). The adjoint vector

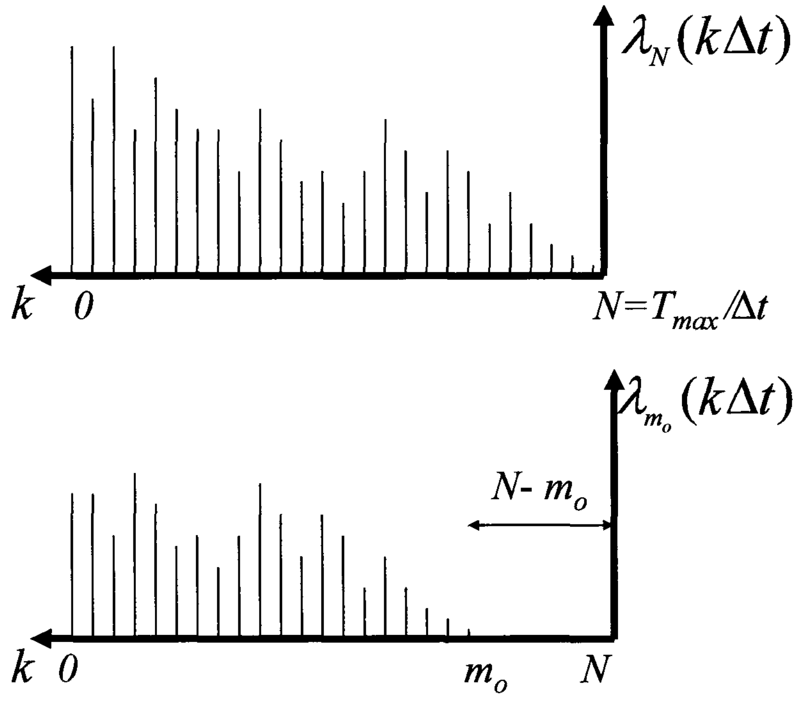

Figure 4.1: Illustration of determination of vector of λ. Parameter λ_N is the adjoint vector for the sensitivity at the N^{th} time step, and λ_{m_o} is for sensitivity at the m_o^{th} time step which can be obtained from λ_N by shifting left by $N-m_o$ time steps.

λ_m for any other m can be obtained by simply shifting the obtained λ by the proper time shift. We choose to carry out the adjoint simulation at $N=T_{\max}/\Delta t$. This simulation gives us λ_m for the sensitivities at the N^{th} time step, λ_N. λ_m for any other time step m_o can be obtained by shifting λ_N by $N-m_o$ time steps in the backward running simulation (See Figure 4.1)

$$\lambda_{m_o}[k]=\lambda_N[k+(N-m_o)]. \tag{4.11}$$

Figure 4.1 shows how the adjoint impulses are shifted in the backward running simulation.

This time shift eliminates the need for extra adjoint simulations and allows us to use only one adjoint simulation.

4.4 PRACTICAL IMPLEMENTATION

Our approach is implemented in a very similar way to the AVM approach in Chapter 3. The only difference is in the determination of the adjoint impulses for different time steps. Thus, our approach can be summarized as the following steps.

Step 1) *Parameterization*: Determine the sets of link indexes L_i whose connection and scattering matrices are affected by the perturbations Δx_i, 1, 2,…, *n*.

Step 2) *Original Analysis*: Carry out the original TLM analysis (2.2) and store the set of corresponding η values $\forall m \in L_i$, $i = 1, 2, ..., n$ at each time step. The values of the incident impulses in the observation point are also stored to determine the adjoint excitation in (4.8).

Step 3) *Adjoint Analysis*: Carry out the backward adjoint analysis and simulate the adjoint system with excitation of $\delta[k\text{-}N]$. Store the adjoint impulses λ_N for the links with indexes L_i, $i = 1, 2, ..., n$ with their corresponding adjoint impulses of the unperturbed structure for all time steps.

Step 4) *Sensitivities Estimation:* Evaluate (4.7) for all *m* and for all the parameters. The vector of λ_m used in (4.7) can be obtained using the obtained adjoint response λ_N in step 3) and property of (4.11) while η is the same all *m*.

4.4.1 Metallic Discontinuities

The variation of the system matrix due to a perturbation in a metallic discontinuity is caused by associated changes in the connection matrix. This was explained earlier in Section 3.2.1. Equation (3.20) is used to calculate the original impulses.

Figure 3.1 illustrates the link storages for different parameter perturbations in 2-D metallic discontinuities. The same method is applied to the 3-D case.

4.4.2 Dielectric Discontinuities

The variation of the system matrix due to a perturbation in a dielectric discontinuity is caused by associated changes in the scattering matrix, while the connection matrix remains the same. This was explained earlier in Section 3.2.2.

Figure 4.2 illustrates the link storages for different parameter perturbations in 2-D dielectric discontinuities. For perturbations of dielectric properties, all the links in the area where dielectric properties are changed should be stored in the original system (Figure 4.2(a)). For the size, only the links in dimension perturbed area should be stored in the original system (Figure 4.2(b)). As Figure 4.2(c) shows, if the dielectric moves to the right by $1\Delta l$, then the system matrix of the links on two "columns" (bold links in original system) are changed. The actuall effects on these two "columns" are opposite. This is because the left-column links (see Figure 4.2(c)) are moving out the object and becoming a part of the surrouding medium while the right-column links are becoming a part of the object and away from the surrounding medium. This action causes opposite changes of dielectric properties on these two column links. The corresponding links which should be stored in the adjoint system are also shown in Figure 4.2. The same approach for links storage is applied to the 3-D case.

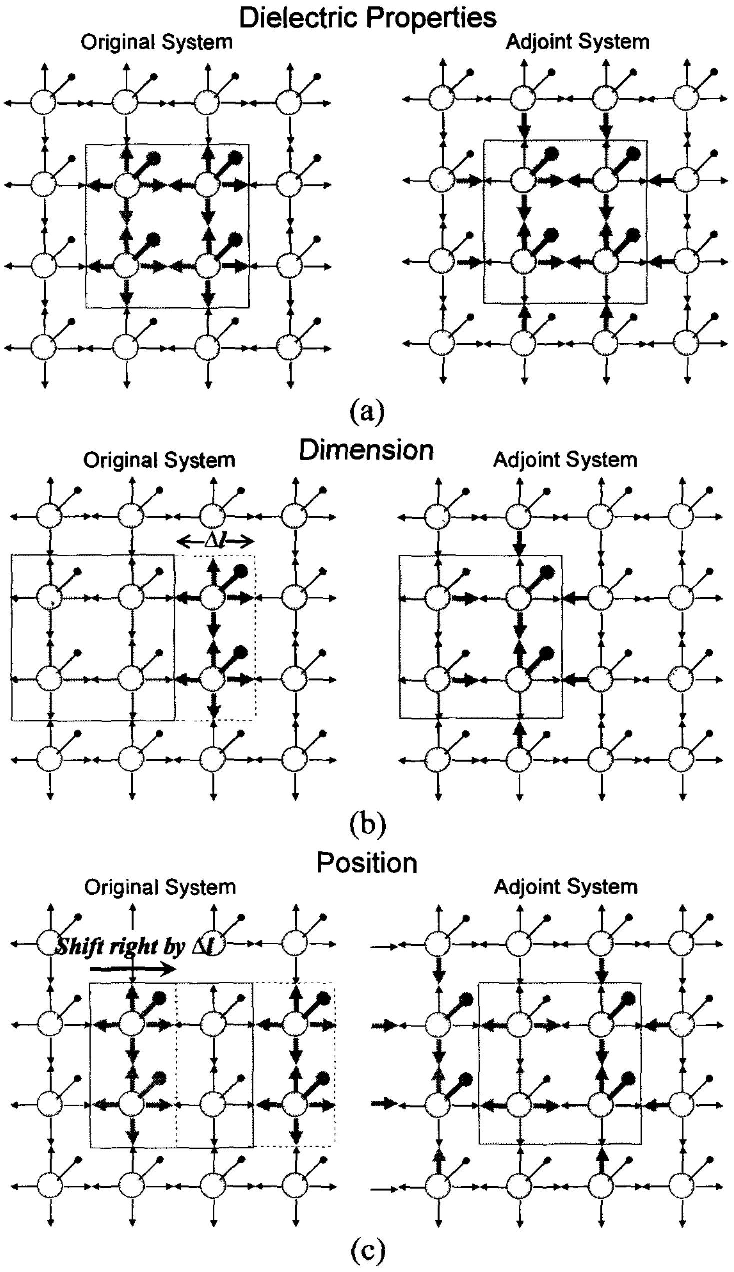

Figure 4.2: Illustration of the links storage. The bold arrowed links in the original system are the ones for which the matrix ΔA has nonzero components for a perturbation. The bold arrowed links in the adjoint system are the corresponding links for the nonzero original impulses. (a) The dielectric properties in grey region are perturbed. (b) The length of grey region is perturbed by Δl. (c) The position of grey region shifts right by Δl. The new positioned region is labelled by dash lines.

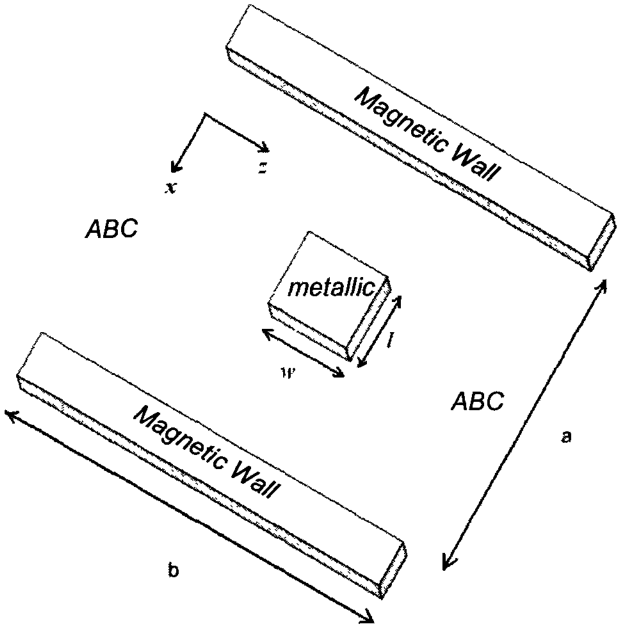

Figure 4.3: Structure of the 2-D metallic example: $a = 14.0$ mm and $b = 30.0$ mm.

4.5 EXAMPLES

We illustrate the new approach through estimation of the sensitivities of objective functions with respect to the dimensions of the discontinuities, relative dielectric constant, conductivity, and position. Our results are compared with the accurate and time-intensive central difference (CD) approximation (4.12)

$$\frac{\partial F}{\partial x_i} = \frac{F(\boldsymbol{x}+\Delta x_i \boldsymbol{e}_i) - F(\boldsymbol{x}-\Delta x_i \boldsymbol{e}_i)}{2\Delta x_i}, \text{ where } i = 1,\ 2, \dots,\ n. \tag{4.12}$$

The objective function for all the examples in this section is taken as

$$F = \int_0^{T_m} E(x_o, y_o, z_o, \tau)\delta(t-\tau)d\tau \tag{4.13}$$

where (x_o, y_o, z_o) is the selected observation point.

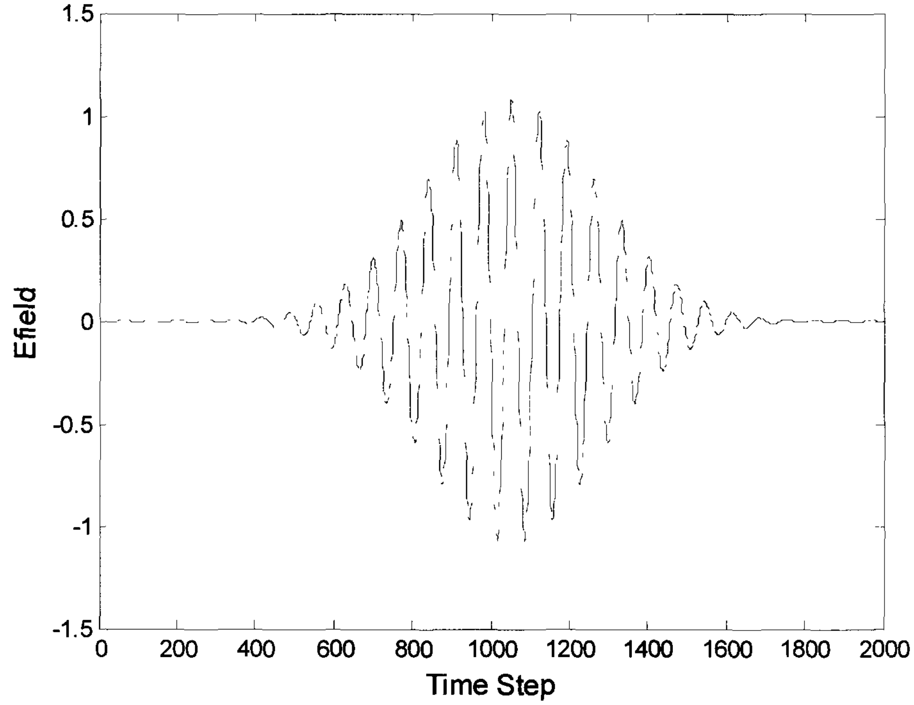

Figure 4.4: Original E-field response of metallic discontinuity.

4.5.1 2-D Metallic Discontinuities

We estimate the sensitivities of the objective function (4.13) for the rectangular metallic discontinuity shown in Figure 4.3. The width is a = 14.0 mm. The length is b = 30.0 mm. The dimension of the discontinuity is w = 3.0 mm and l = 2.0 mm. A square cell of mesh size $\Delta l = 1.0$ mm is utilized. The boundaries are magnetic walls and absorbing boundary conditions (ABC). This problem is simulated as a 2-D problem with a Gaussian modulated sinusoidal excitation of center frequency f = 3.0 GHz and a bandwidth BW=1.0 GHz. The excitation domain includes all the nodes at the first column

z=1. The observation point is the mid-point at the last column $z=N_z$. Figure 4.4 shows the original E-field response.

The perturbation of dimension enlarges the object by one cell in the $+z$ and $+x$ direction. The comparison between the AVM results and the CD derivatives is shown in Figure 4.5. We notice that the error is acceptable for optimization purposes.

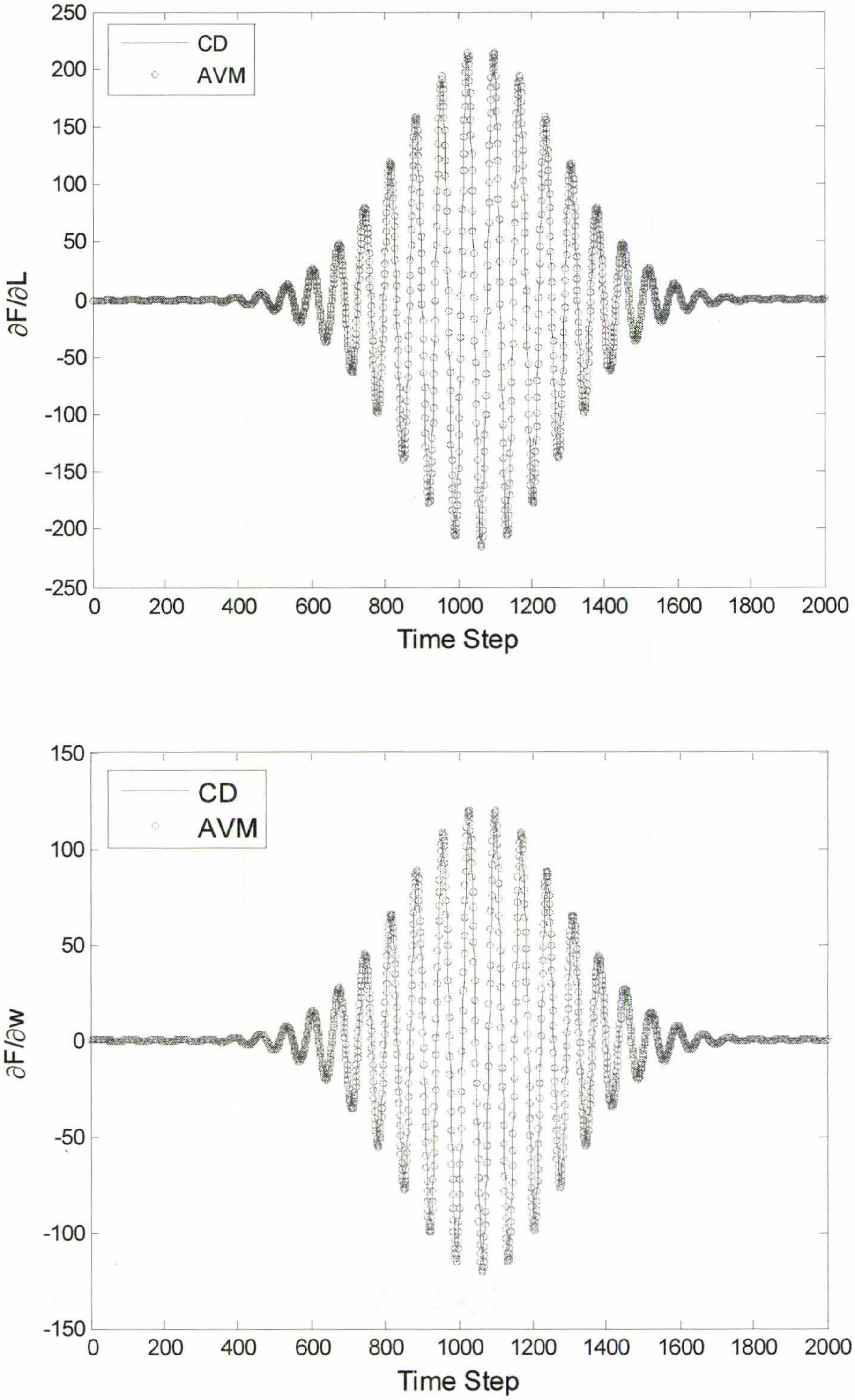

Figure 4.5: The objective function sensitivities, $\partial F/\partial l$ and $\partial F/\partial w$.

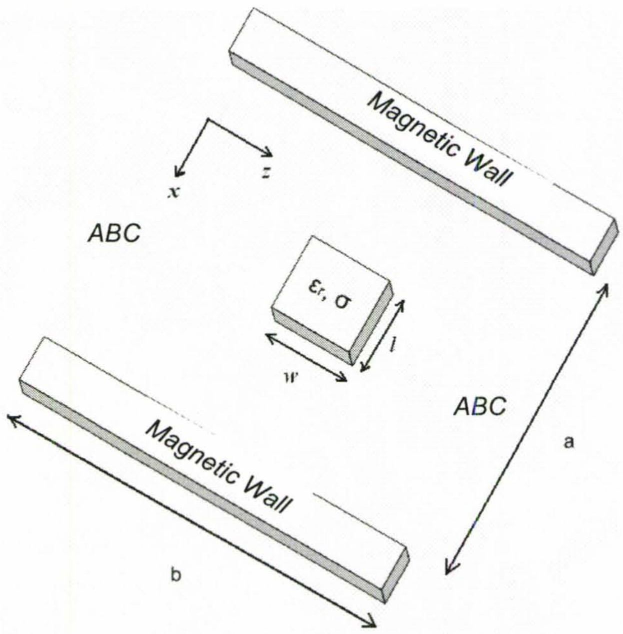

Figure 4.6: Structure of the 2-D dielectric example: a = 15.0 mm and b = 31.0 mm.

4.5.2 2-D Lossy Dielectric Discontinuities

We estimate the objective function sensitivities for the rectangular dielectric discontinuity shown in Figure 4.6. The width is a = 15.0 mm and the length is b = 31.0 mm. The dimension of the discontinuity is w = 2.0 mm and l = 2.0 mm. The same settings as those in 4.5.1 are utilized for the boundaries and excitation. The dielectric properties of the object are $\varepsilon_r = 8.0$ and $\sigma = 1.0$, and the surrounding area has $\varepsilon'_r = 3.0$ and $\sigma' = 0.5$. Figure 4.7 shows the original E-field response at these settings.

The perturbation of dimension enlarges the object by one cell in the +z and +x directions. The perturbation of discontinuity's ε_r and σ is 3%. When estimating

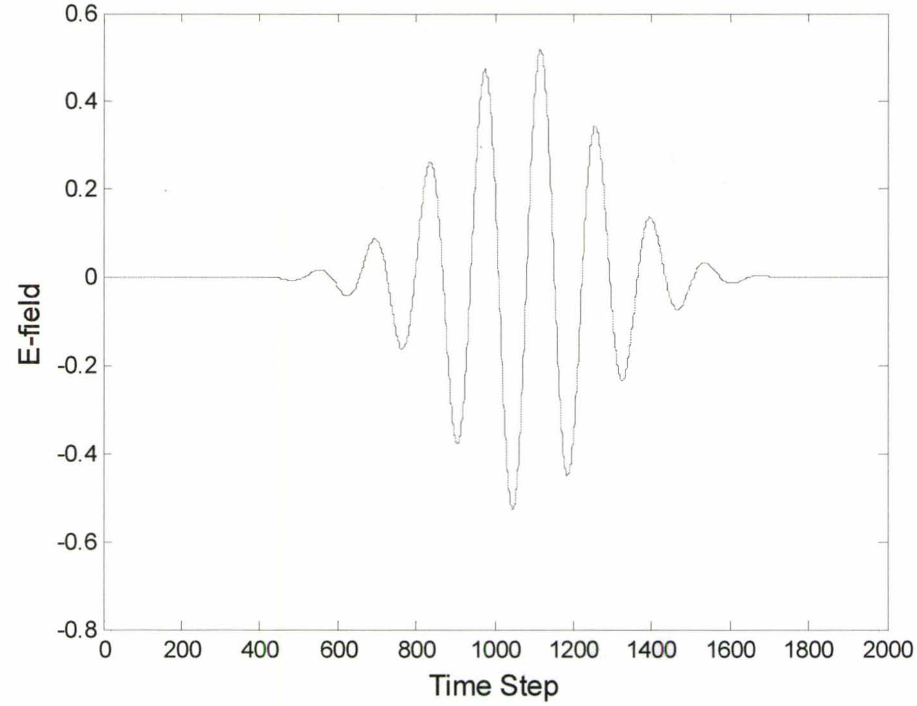

Figure 4.7: Original E-field response of dielectric discontinuity.

sensitivities with respect to ε_r, we use (3.24). A similar analytical approach is also utilized in estimating the sensitivities with respect to the conductivity σ:

$$\frac{\partial F}{\partial x_i} \approx \frac{\partial^e F}{\partial x_i} - \Delta t \sum_{n=l}^{l+m} \sum_k \left(\lambda_k^T \frac{\partial \boldsymbol{A}_i}{\partial \sigma_n} \boldsymbol{V}_k \cdot \frac{\Delta \sigma_n}{\Delta x_i} \right). \tag{4.14}$$

The perturbation of position is increasing the coordinate of object's top left corner by one cell in the +*z* and +*x* direction. If the coordinate of top left corner is (z_o, x_o), then the position after perturbation becomes (z_o+1, x_o) or (z_o, x_o+1), depending on the perturbation direction.

The comparison between the AVM results and the CD derivatives is shown in Figures 4.8 - 4.10. Very good match is observed between the two techniques. Only the sensitivity of position x has small difference at the response peaks where the sensitivity is highly nonlinear.

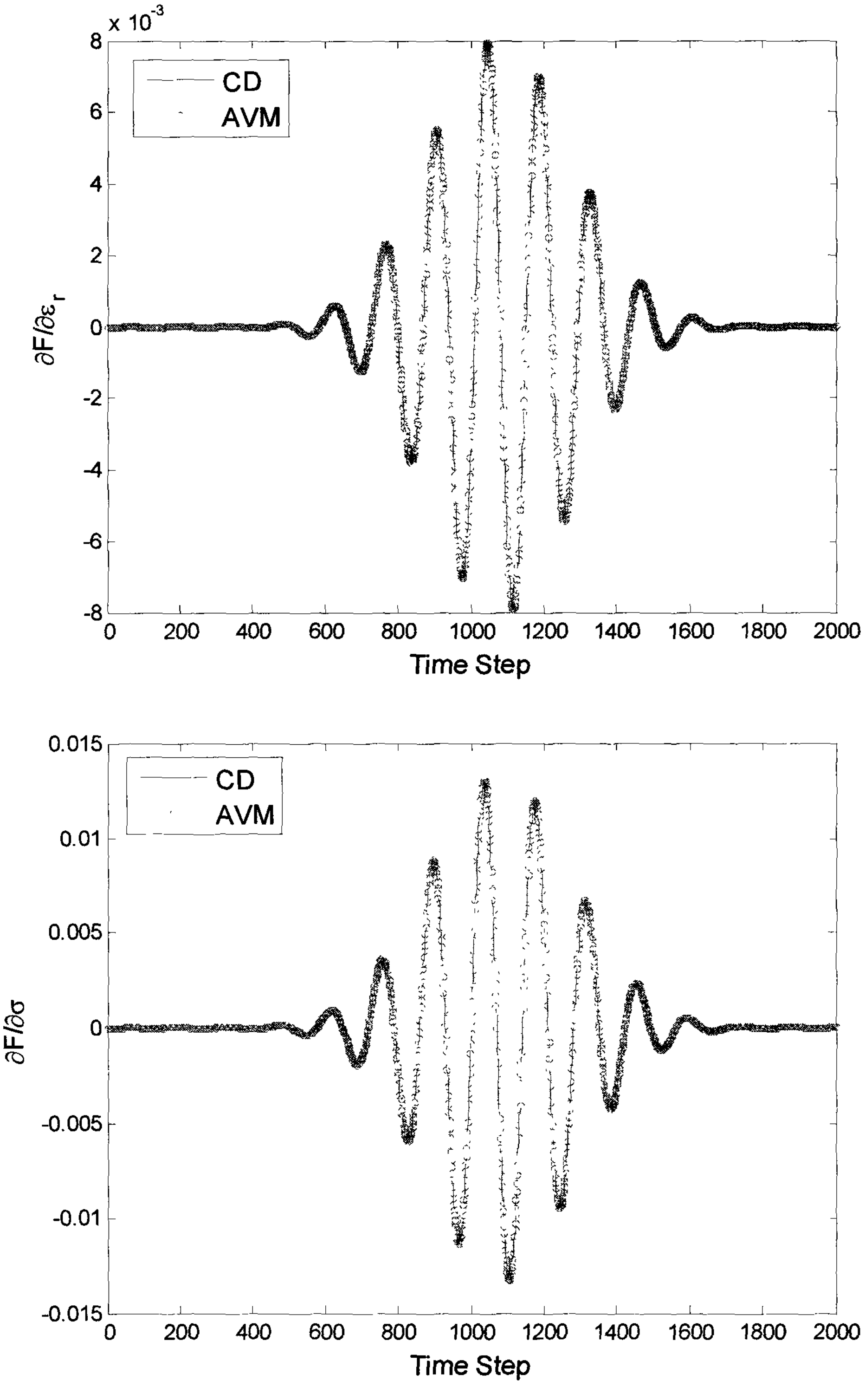

Figure 4.8: The objective function sensitivities $\partial F / \partial \varepsilon_r$ and $\partial F / \partial \sigma$.

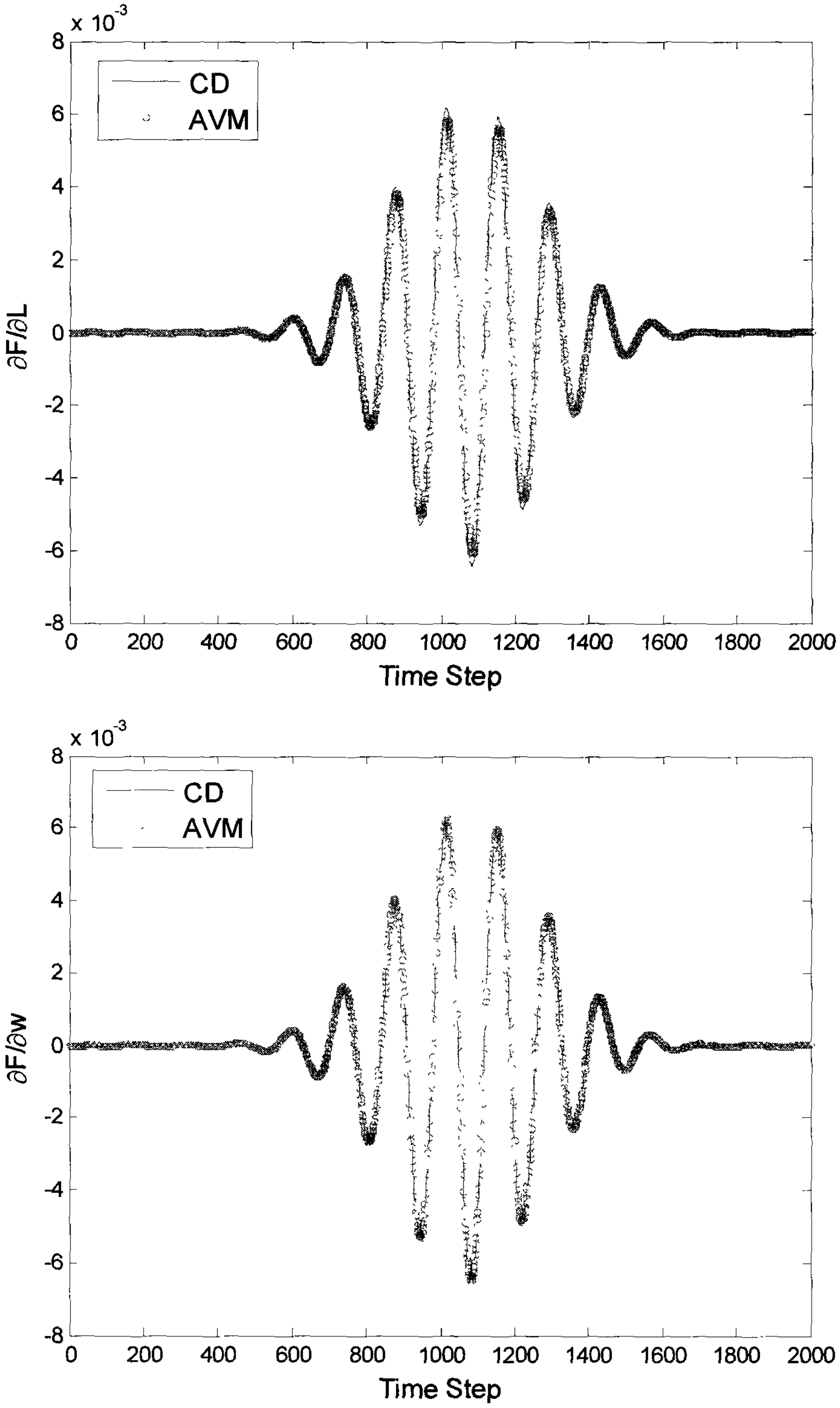

Figure 4.9: The objective function sensitivities $\partial F / \partial l$ and $\partial F / \partial w$.

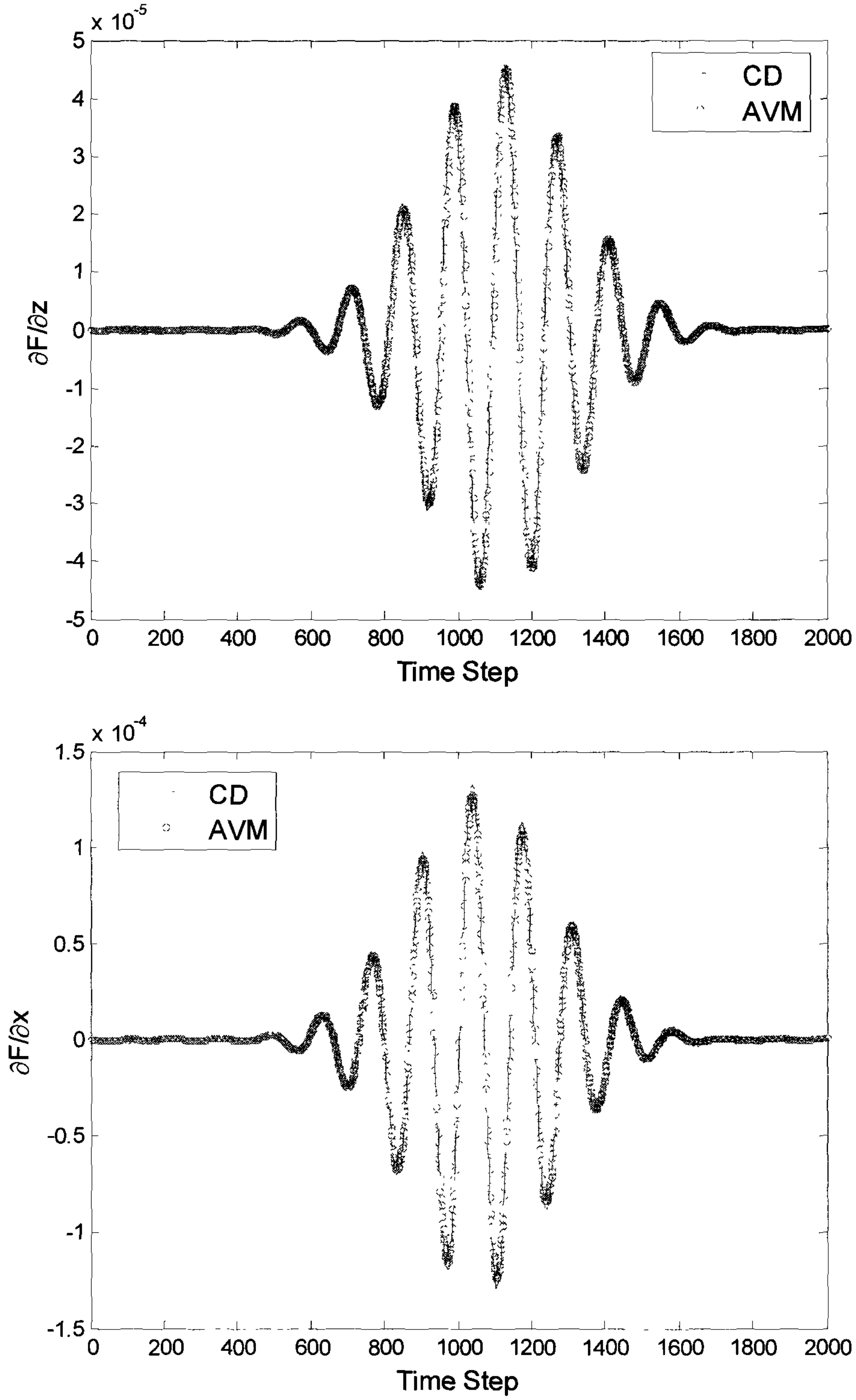

Figure 4.10: The objective function sensitivities with respect to the position z and position x, i.e., $\partial F / \partial z$, and $\partial F / \partial x$.

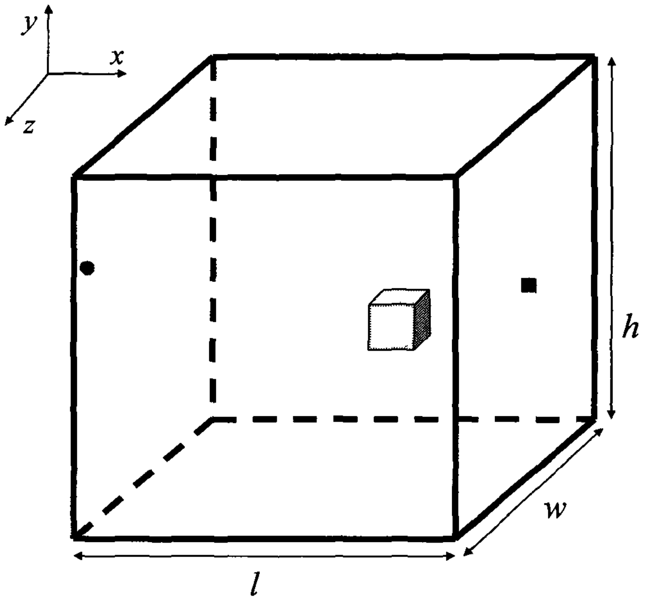

Figure 4.11: Structure of the 3-D dielectric discontinuity. The circle is the excitation point and the square is the observation point.

4.5.3 3-D Lossy Dielectric Discontinuities

We estimate the objective function sensitivities for the rectangular dielectric discontinuity shown in Figure 4.11. The discontinuity is cubic of size 2.0 mm. The length l is 20.0 mm, the width w is 20.0 mm, and the height h is 10.0 mm. The boundaries are all Absorbing Boundary Conditions (ABCs). This problem is simulated with a Gaussian modulated sinusoidal excitation of center frequency f = 3.0 GHz and a bandwidth BW=1.0 GHz. The excitation point is $(x_e, y_e, z_e) = (1,14,20)$ and the observation is the E_x at $(x_o, y_o, z_o) = (20,10,20)$. Figure 4.12 shows the field response E_x under these settings.

The perturbation of discontinuity's ε_r and σ is 3.0%. The nominal discontinuity's dielectric constant is $\varepsilon_r = 57.2$ and $\sigma = 1.08$, and the surrounding area has dielectric

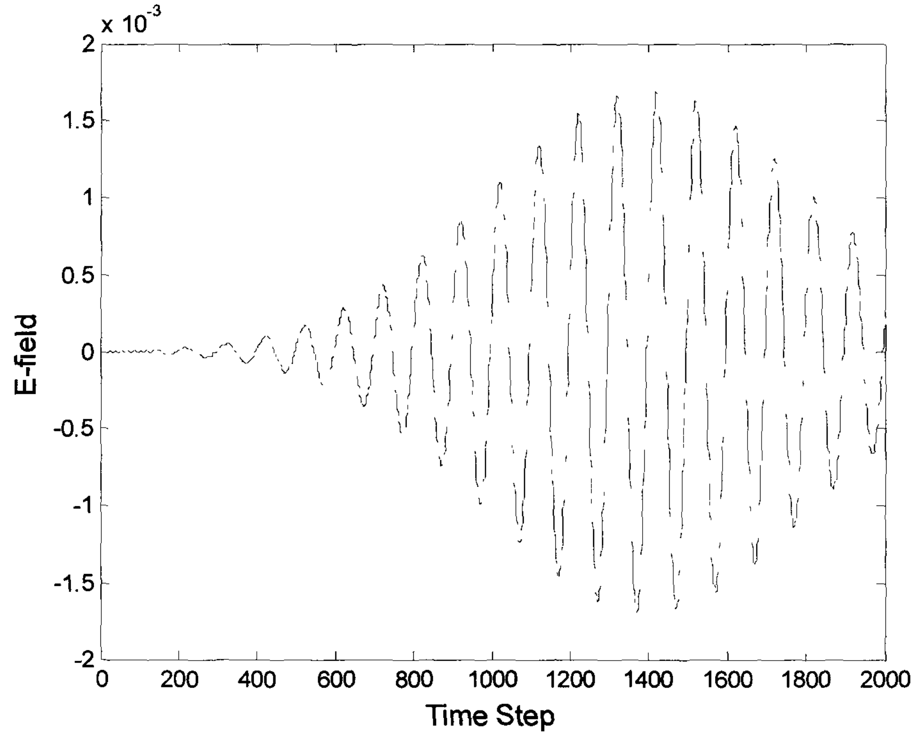

Figure 4.12: Original E-field response of the 3-D example with a Gaussian modulated sinusoidal excitation.

properties of $\varepsilon_r = 16$ and $\sigma = 0.16$. The perturbation at the position is $1\Delta l$ and the nominal discontinuity's top-left corner is located at $(10,5,4)$.

The comparison between the AVM results and the CD derivatives is shown in Figures 4.13 - 4.16. Very good match is observed between the two techniques.

We also do the simulation with an excitation of Equation (4.14)

$$V_s = \begin{cases} e^{-\frac{(t-\mu)^2}{2\sigma^2}} \cdot \sin(2\pi f_c t), & t \le \mu \\ \sin(2\pi f_c t), & t > \mu \end{cases} \tag{4.14}$$

where $f_c = 3.0$ GHz, μ is the mean value, and σ is the variance. The original E-field response of this excitation is shown in Figure 4.17 and the comparison between the AVM results and the CD derivatives is shown in Figures 4.18 - 4.21. Good match is obtained between the two techniques.

4.6 CONCLUSION

For the first time, an adjoint variable method is presented for efficient estimation of sensitivities of complete time-domain responses utilizing the time-domain TLM method. Regardless of the number of design parameters, the sensitivities at each time step with respect to all of them are obtained using only two analyses of the original and adjoint systems. Our approach is illustrated through the estimation of the sensitivities with respect to the dimensions, dielectric properties, and the position of the discontinuities in both 2-D and 3-D cases. Very good match is obtained between our approach and CD derivative.

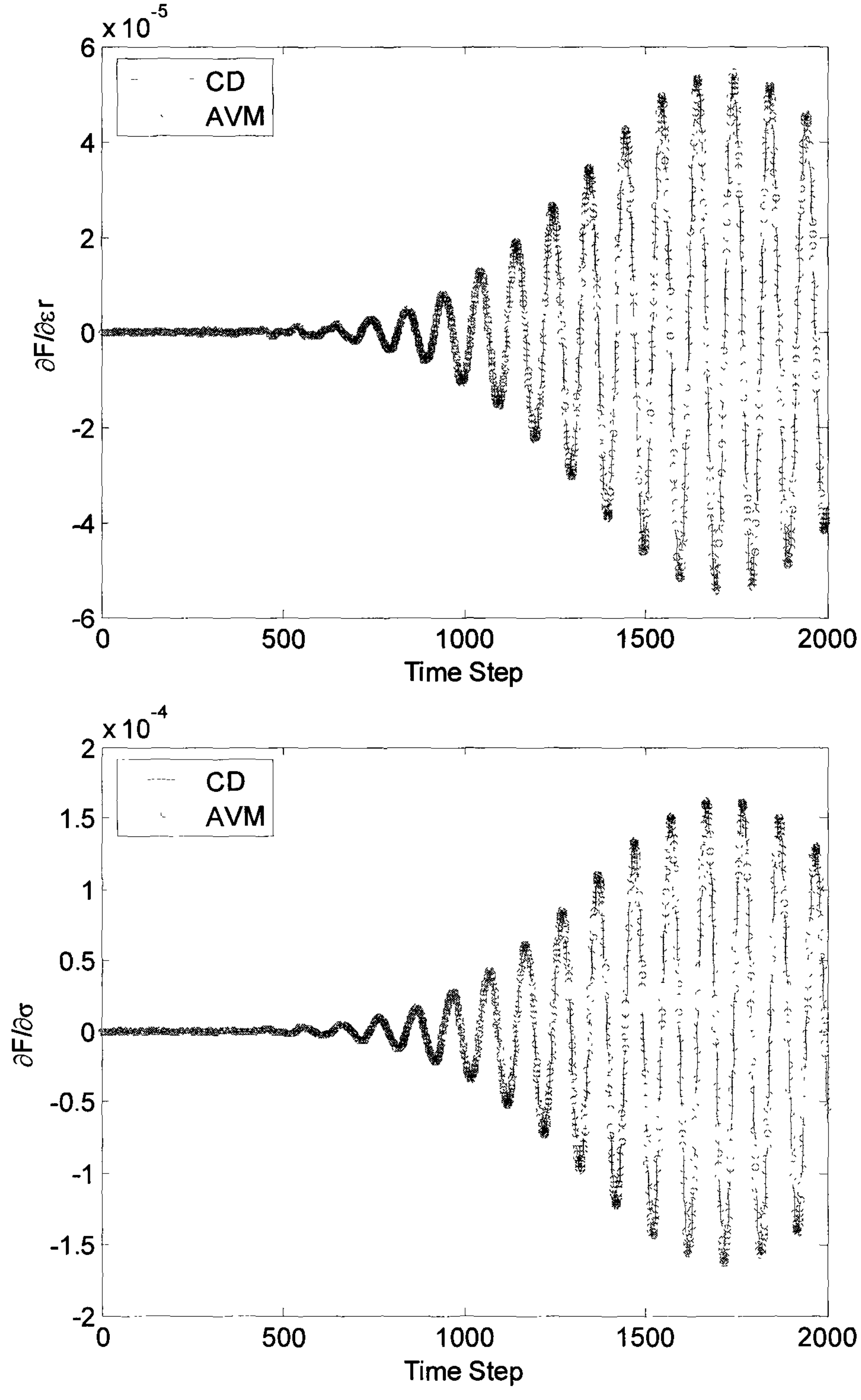

Figure 4.13: The objective function sensitivity with respect to discontnuity's dielectric constants $\partial F/\partial \varepsilon_r$ and $\partial F/\partial \sigma$.

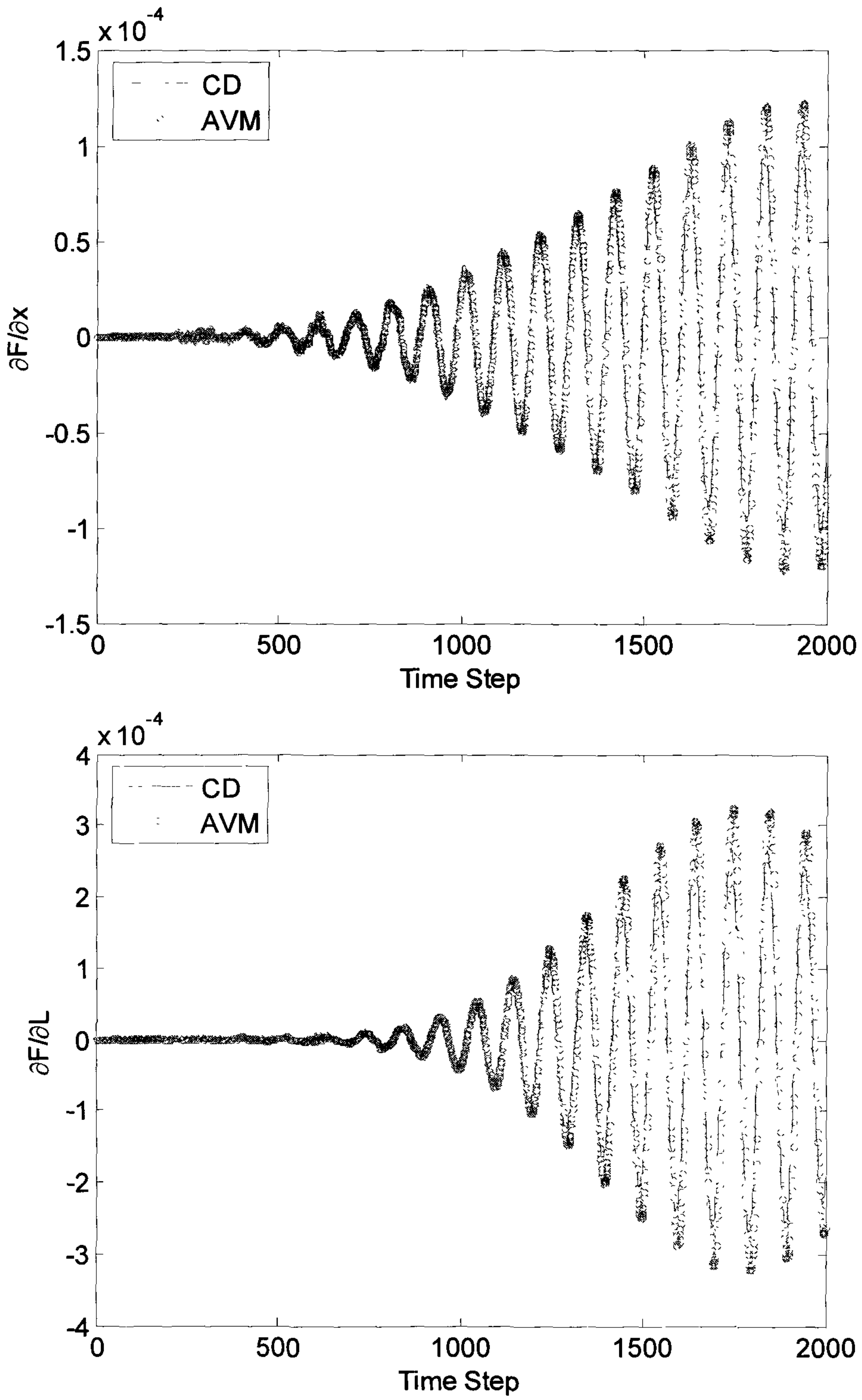

Figure 4.14: The objective function sensitivities with respect to position x, $\partial F/\partial x$ and the dimension in x direction, $\partial F/\partial L$.

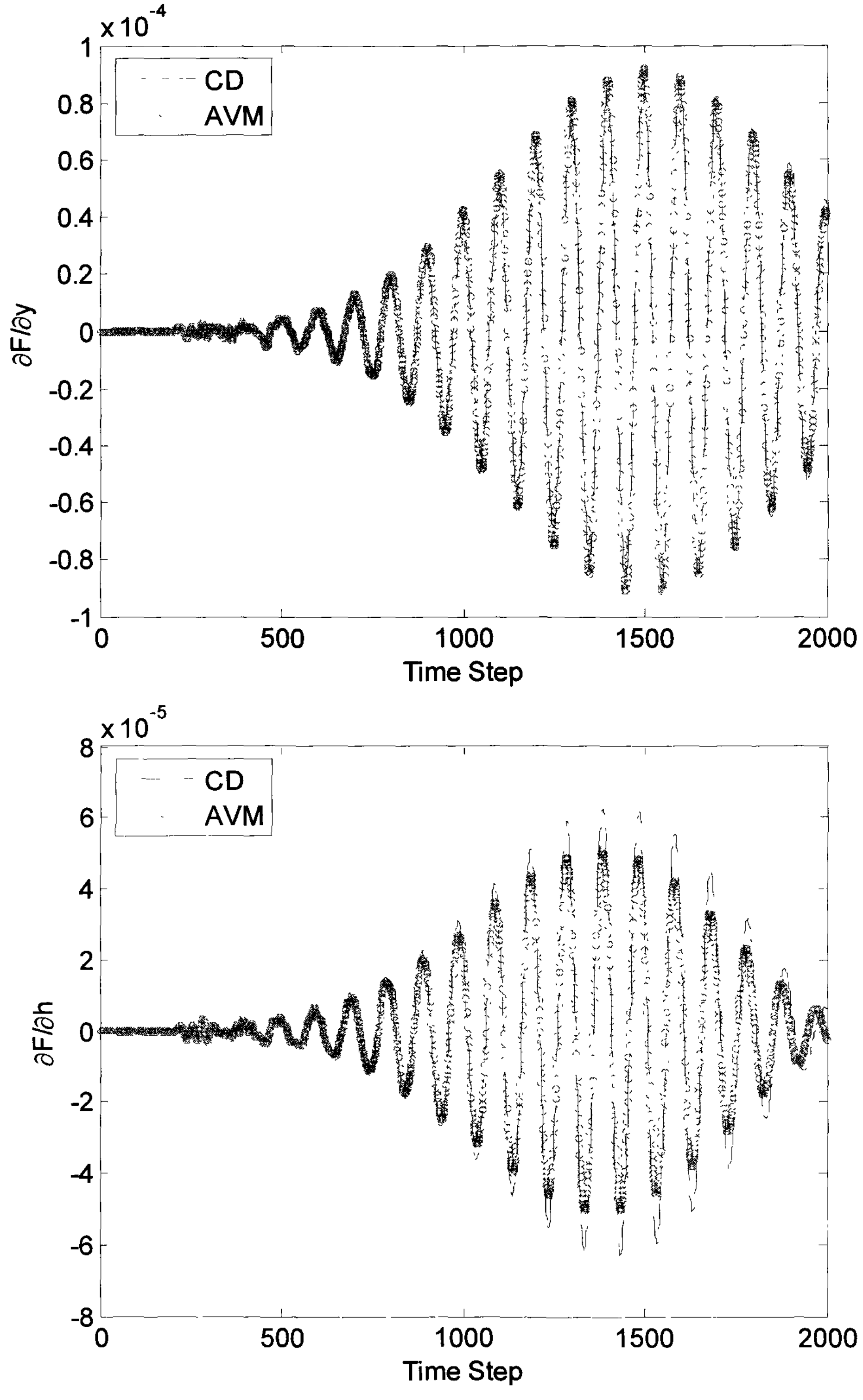

Figure 4.15: The objective function sensitivities with respect to position y, $\partial F / \partial y$ and the dimension in y direction, $\partial F / \partial h$.

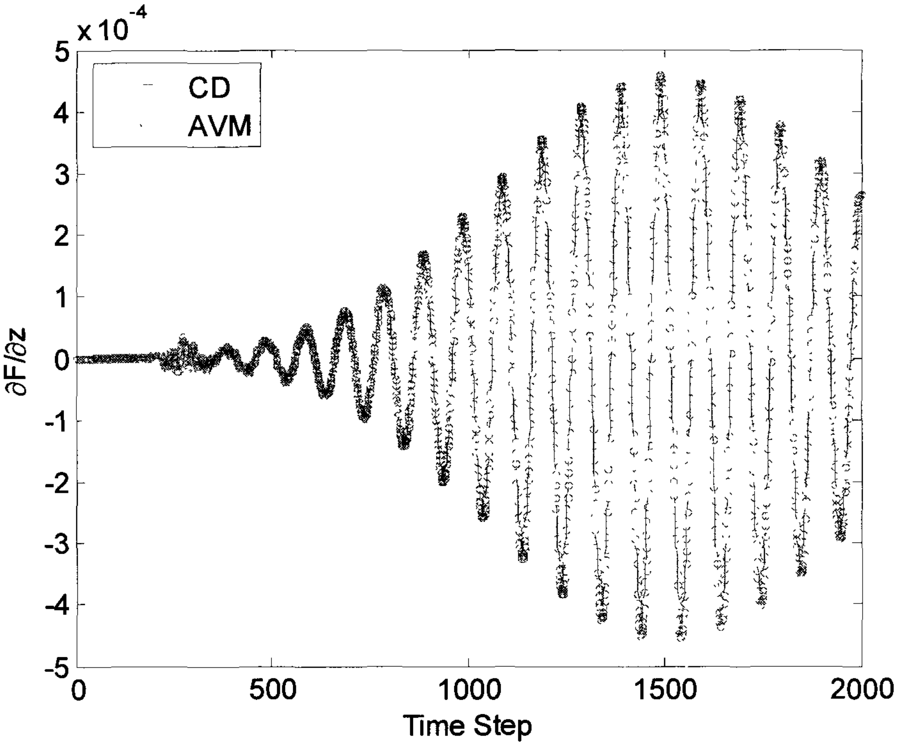

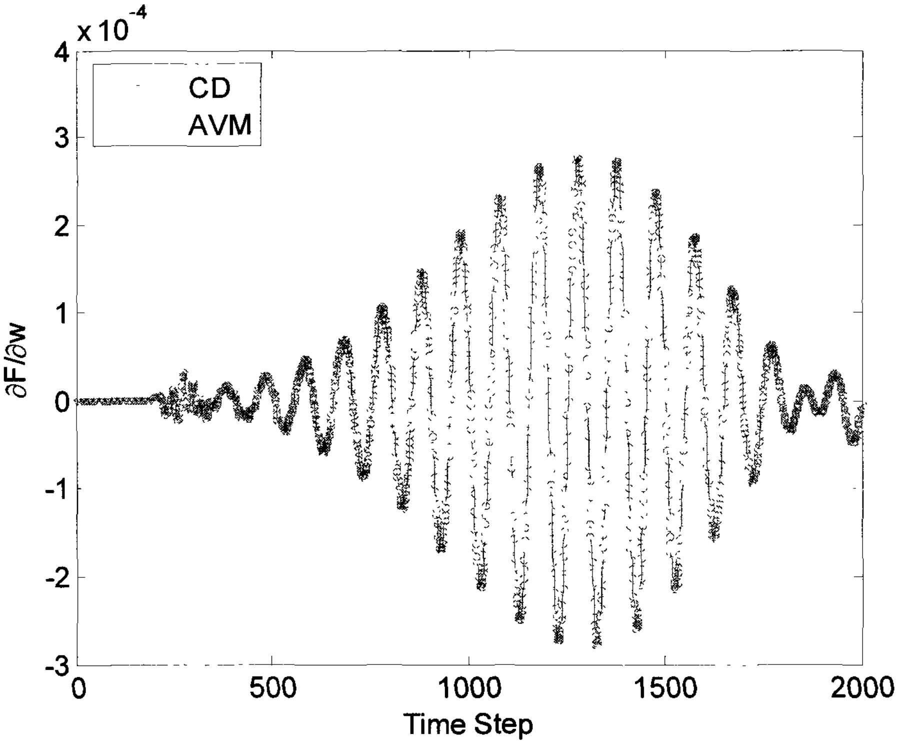

Figure 4.16: The objective function sensitivities with respect to position z, $\partial F / \partial z$ and the dimension in z direction, $\partial F / \partial w$.

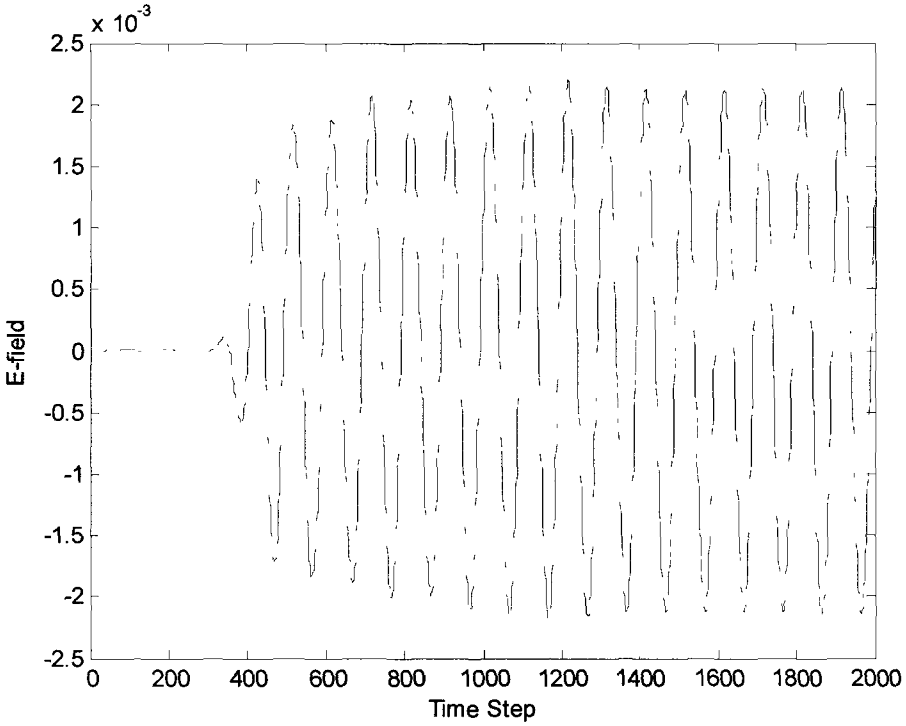

Figure 4.17: Original E-field response of the 3-D example with a sinusoidal excitation.

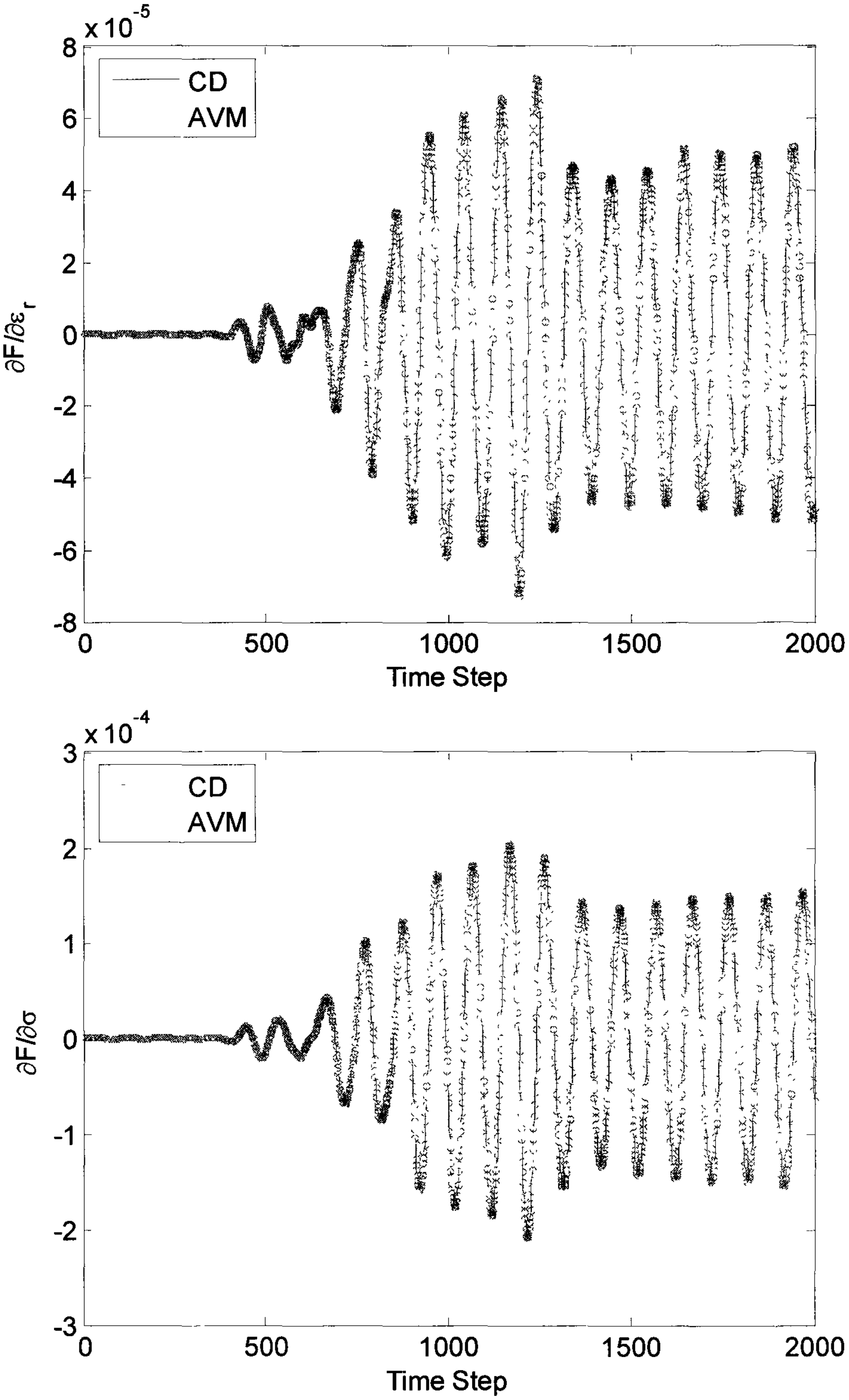

Figure 4.18: The objective function sensitivity with respect to discontinuity's dielectric constants $\partial F/\partial \varepsilon_r$ and $\partial F/\partial \sigma$.

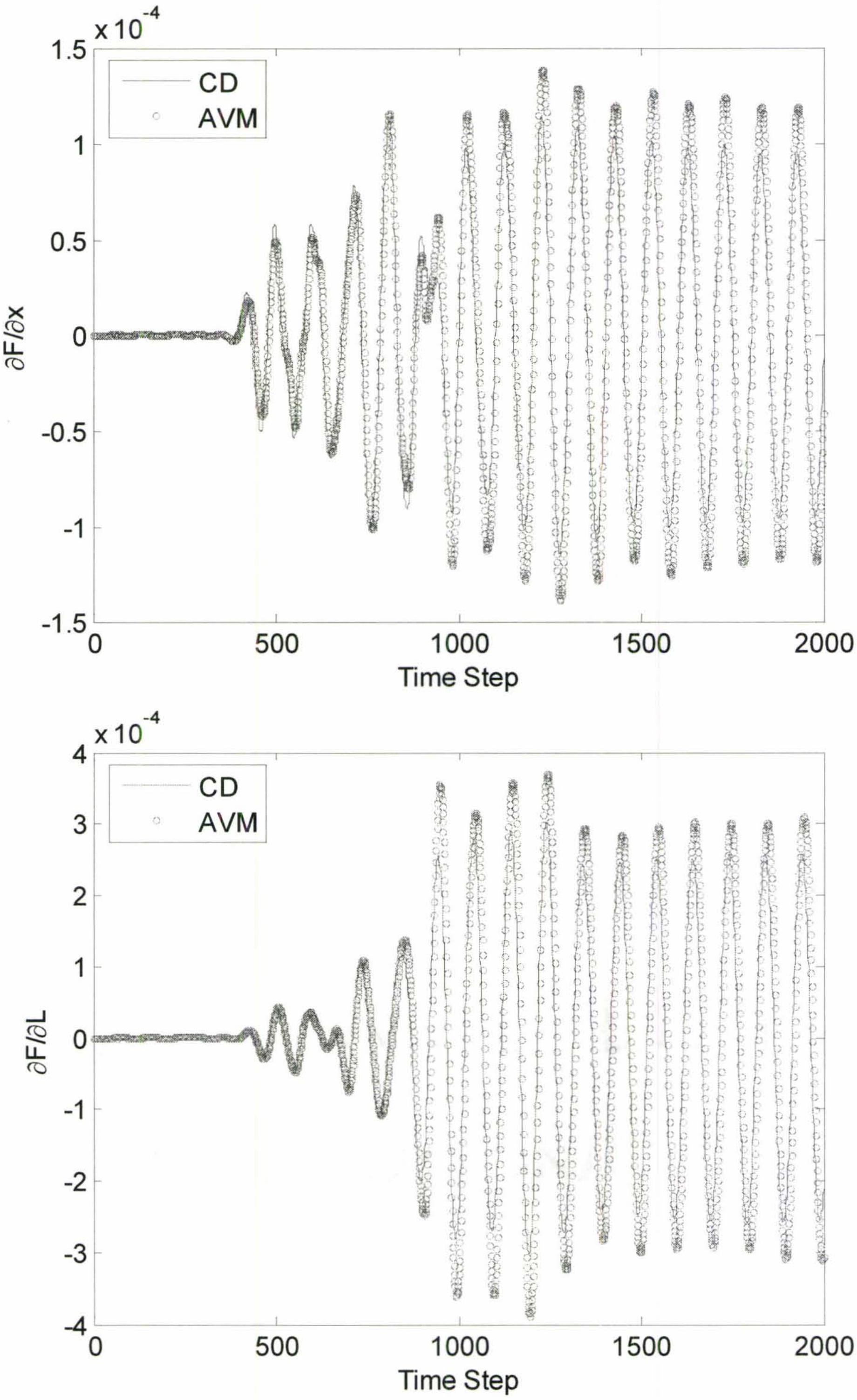

Figure 4.19: The objective function sensitivities with respect to position x, $\partial F/\partial x$ and the dimension in x direction, $\partial F/\partial L$.

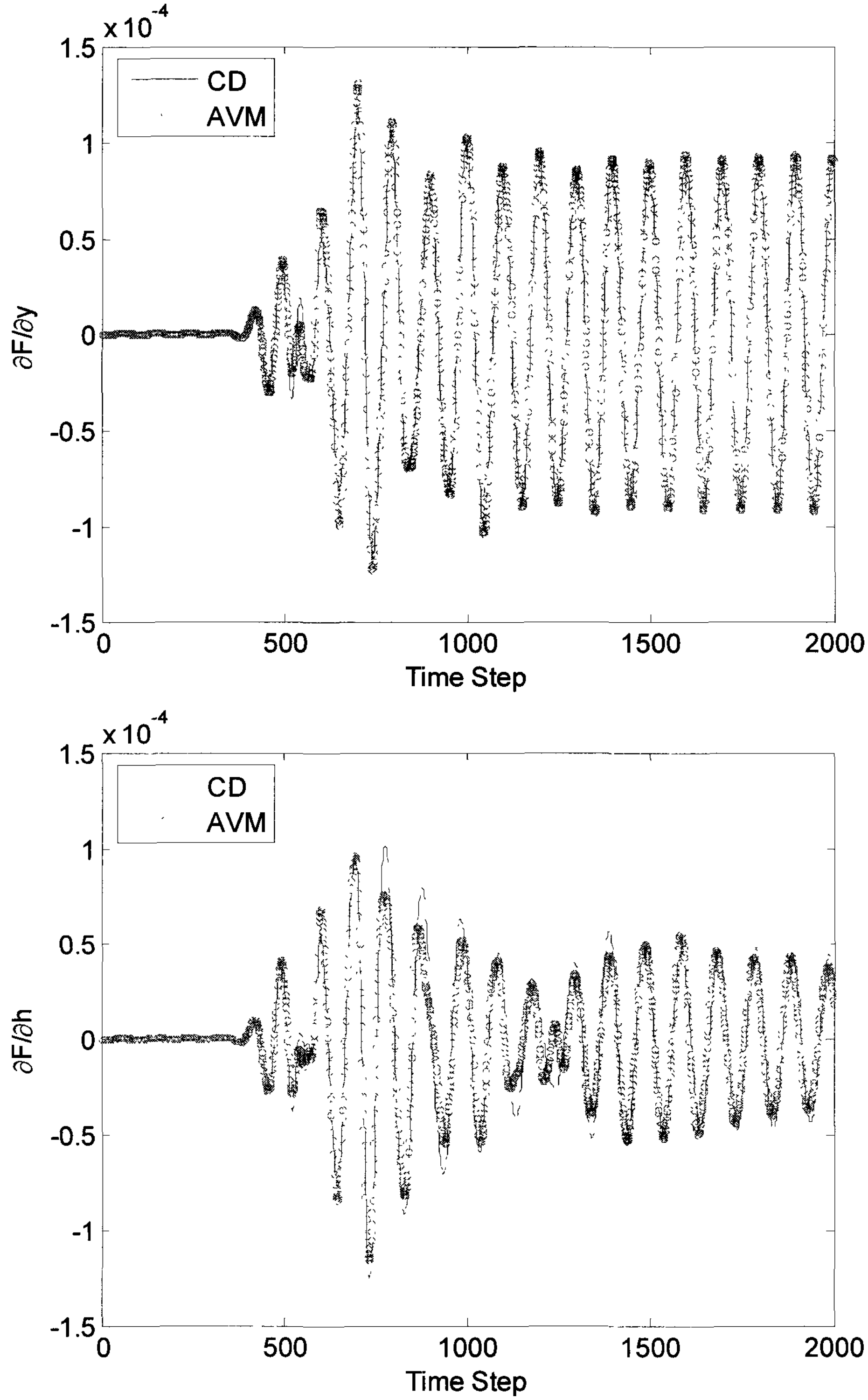

Figure 4.20: The objective function sensitivities with respect to position y, $\partial F/\partial y$ and the dimension in y direction, $\partial F/\partial h$.

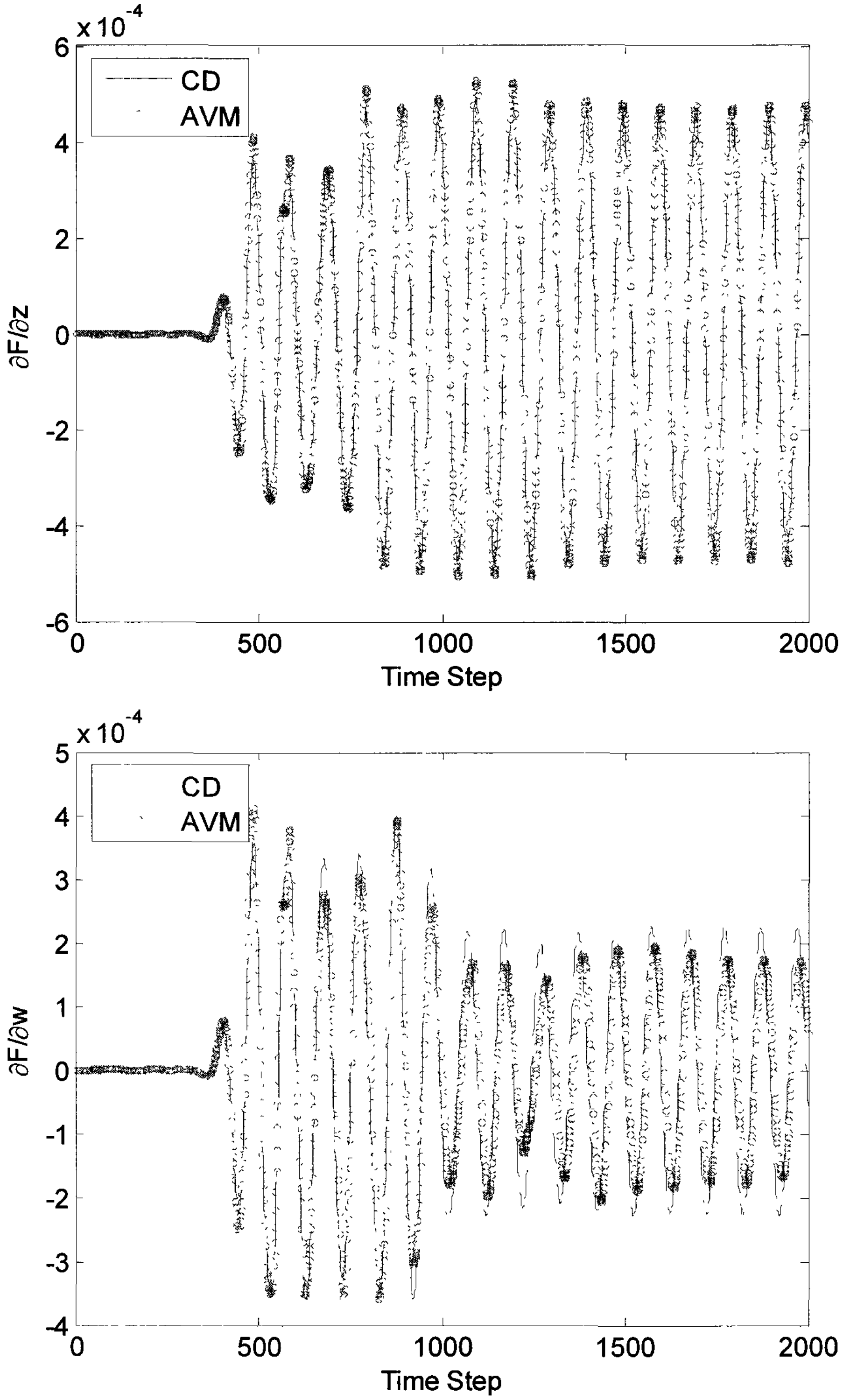

Figure 4.21: The objective function sensitivities with respect to position z, $\partial F / \partial z$ and the dimension in z direction, $\partial F / \partial w$.

REFERENCES

[1] M.H. Bakr and N.K. Nikolova, “An adjoint variable method for time-domain transmission-line modeling with fixed structured grids,” *IEEE Trans. Microwave Theory Tech.*, vol. 52, NO. 2, pp554-559, Feb. 2004.

[2] M.H. Bakr and N.K. Nikolova, “An adjoint variable method for time-domain TLM with wide-band Johns matrix boundaries,” *IEEE Transactions on Microwave Theory and Techniques*, vol. 52, pp. 678-685, 2004.

[3] P.A.W. Basl, M.H. Bakr, and N.K. Nikolova, “Efficient estimation of sensitivities in TLM with dielectric discontinuities,” *IEEE Trans. Microwave Wireless Comp.*, vol. 15, pp.89-91, Feb. 2005.

[4] P.A.W. Basl, M.H. Bakr, and N.K. Nikolova, “An AVM technique for 3-D TLM with Symmetric Condensed Nodes,” *IEEE Trans. Microwave Wireless Componnets letters.*, vol. 15, pp.618-620, 2005.

[5] P.A.W. Basl, M.H. Bakr, and N.K. Nikolova, “Time-domain sensitivity analysis of planar structures using first-order one-way wave equation boundaries,” in *International Journal of Numerical Modelling: Electric Networks, Devices and Fields:* John Wiley and Sons Ltd, Chichester, West Sussex, PO 19 8SQ, United Kingdom, 2006.

[6] P.A.W. Basl, M.H. Bakr, and N.K. Nikolova, “Efficient TLM sensitivity analysis exploiting rubber cells,” *Computational Electromagnetics Research Laboratory*, McMaster University, Canada, 2008.

[7] M.H. Bakr, N.K. Nikolova, and P.A.W. Basl, “Self-adjoint S-parameter sensitivities for lossless homogeneous TLM problems,”*International Journal of Numerical Modelling: Electric Networks, Devices and Fields,* vol. 18, pp. 441-455, 2005.

[8] P.A.W. Basl, M.H. Bakr, and N.K. Nikolova, “The theory of self-adjoint S-parameter sensitivities for lossless nonhomogeneous TLM problems,” *IEEE Transactions on Microwave Theory and Techniques*, 2006.

[9] F. Trevisan, M. Guanieri, and A. Stella, “A methodological analysis of different formulations for solving inverse electromagnetic problems,” *IEEE Transactions on Magnectics*, MAG-26(2), 1990.

[10] W.M. Boerner, *et al*, eds, "Inverse methods in electromagnetic imaging," *Math. & Phys. Sci.*, vol. 143.D, Holland, 1985.

[11] N. Joachimowicz, C. Pichot, and J. P. Hugonin, "Inverse scattering: An iterative numerical method for electromagnetic imaging," *IEEE Trans. Antennas Propag.*, vol. 39, pp. 1742-1752, 1991.

[12] M.H. Bakr, P. Zhao, and N.K. Nikolova, "Microwave imaging exploiting adjoint based surrogate models," *ACES International Conference on Wireless Communications and Applied Computational Electromagnetics*, Niagara Falls, ON, Canada, 2008.

[13] M.H. Bakr, P. Zhao, and N.K. Nikolova, "Adjoint First Order sensitivities of time domain responses and their applications in the solution of inverse problems," *IEEE Trans. AP*, submitted.

[14] MEFiSTO-2D and MEFiSTO Nova, Faustus Scientific Corporation, 1998-2001.

CHAPTER 5

EFFICIENT OPTIMIZATION EXPLOITING THE AVM

5.1 INTRODUCTION

The new technique presented in chapter 4 provides us accurate sensitivities of the complete time-domain response in an efficient way. This response may be any electric or magnetic field component. These sensitivities are useful in gradient-based optimization which requires not only the objective function value but its gradients as well. A gradient-based optimization technique normally converges to a local optimal solution much faster than non-gradient-based optimization technique. Therefore, a fast and accurate approach for sensitivity estimation is crucial.

In gradient-based optimization, there are two factors to determine its efficiency. The first factor is the number of iterations which is determined by the combinations of the nature of the optimization algorithm, the formulation of the objective function, and the accuracy of the objective function gradient. The second factor is the number of the evaluations per iteration which mainly depends on how the gradients are computed. Therefore, efficient gradient estimation algorithms are important for optimization efficiency. The sensitivities obtained using Finite Differences (FD) approximations are time-intensive even for simple problems. This involves perturbing each design parameter in the forward and/or backward directions and simulating the perturbed structures. The AVM algorithms discussed in Chapters 3 and 4 generate the field response and its gradients using at most two analyses of the original and the adjoint simulations regardless of the number of design parameters. Therefore, the optimization efficiency can be significantly improved if our AVM is used through the optimization process.

Gradient-based optimization, however, does not guarantee that a global minimum is found. The quality of the initial design is also an important factor to the optimization performance. With a good initial solution, gradient-based optimization technique is more preferred than other optimization techniques for EM problems.

The sensitivities of time-domain response can be used for object identification [1]. Transmitting and receiving antennas are put in the neighborhood of the object. They are utilized for sending incident waves and receiving reflected waves, respectively. An object function can be optimized using the measured time-domain field and the time-domain sensitivities to determine the unknown object parameters.

For over a decade, microwave engineers have been carrying out research in the area of breast imaging. According to Wikipedia [2], it is said that "*Worldwide, breast cancer is the second most common type of cancer after lung cancer (10.4% of all cancer* *incidence, both sexes counted) and the fifth most common cause of cancer death. However, among women worldwide, breast cancer is by far the most common cause of cancer, both in incidence and death. In 2005, breast cancer caused 502,000 deaths worldwide (7% of cancer deaths; almost 1% of all deaths). A U.S. study conducted in 2005 by the Society for Women's Health Research indicated that breast cancer remains the most feared disease, even though heart disease is a much more common cause of death among women.*" Many techniques [3]-[14] have been developed and applied to 2-D and 3-D breast tumor detection problems. All these techniques are based on the fact that breast tumors have dielectric properties at microwave frequencies that are different from those of normal breast tissue. In this Chapter, we will discuss tumor detection not only for the tumors with very different dielectric discontinuities [15] but also for tumors with not very different dielectric properties. Such a case exists in certain types of tissues [1].

We make use of the sensitivities of time-domain response obtained from our novel algorithm introduced in Chapter 4 to estimate the dielectric properties, shape and location of breast tumors. Section 5.2 briefly reviews some developments of microwave imaging and Section 5.3 presents general idea of the solution of inverse problems. In Section 5.4, our approach is applied to a 2-D tumor detection utilizing gradient-based surrogate models. The examples of the 2-D tumor detection using direct optimization are presented in Section 5.5. Finally, the conclusions are discussed in Section 5.6.

5.2 BREAST CANCER DETECTION

Microwave imaging is becoming a popular method for breast cancer detection in recent decades. It utilizes the contrast in dielectric properties of normal tissues and cancer tissues to obtain an image of internal body structures. The transmitting and receiving antennas in the neighborhood of the breast are utilized for sending the incident waves and receiving reflected waves, respectively. The reflected waves are induced by the contrast in the dielectric properties at microwave frequencies between normal breast tissue and malignant lesion [16], [17].

There are three main features for breast cancer detection: active, passive, and hybrid. Passive methods (microwave radiometry) detect tumors based on measuring temperature differences [3]-[6]. The cancerous breast tissue has an increased tumor temperature compared with healthy breast tissue. The breast image is obtained by measuring the temperature over the breast. Hybrid methods use ultrasound transducers to detect pressure waves generated by the heated tissues [7]-[10]. Active methods use microwaves to illuminate the breast. The reflected signals are then measured. The shape and location of tumors are estimated using both the incident and scattered fields. In general, inverse scattering approaches are involved. There are two categories of active microwave breast imaging: microwave tomography and ultra-wide band (UWB) radar techniques. Microwave tomography [11] recovers shape, location and dielectric properties. Its reconstruction approaches involve iteratively matching computed and measured data, where computed data are computed using numerical techniques and a model of the object of interest. UWB techniques [12], [13] seek to identify the existence and location of significant tumors in the breast, rather than to recover the dielectric properties of the breast. In an UWB microwave imaging system, an array of antennas placed near the breast transmits UWB pulses. Reflected microwave signals from the breast are recorded and used to identify the existence and location of tumors. Both these techniques are essentially expensive optimization problems.

5.3 THE SOLUTION OF INVERSE PROBLEMS [18]

Inverse problems involve finding unknown properties of objects or mediums from observed response. For electric circuits, the inverse problem may be used to determine the circuit topology, time-dependent variations of source and the values of circuit elements parameters to achieve a specified circuit response [19]. For electromagnetic problems, the solution of the inverse problem is the spatial distribution of sources and material properties required to achieve a specified field distribution [20]. In inverse problems, the parameters may have some conditions which describe the optimal behaviour of the problem.

A general equation of inverse problem is defined as following equation [18]

$$\boldsymbol{A}(\boldsymbol{p})\boldsymbol{x} = \boldsymbol{b} \tag{5.1}$$

where $\boldsymbol{x}$ is a $M \times 1$ vector of actual source, $\boldsymbol{b}$ is a $N \times 1$ vector of existing field, and $\boldsymbol{p}$ is an unknown vector of the problem's optimized parameters. Matrix $\boldsymbol{A}$ is a $N \times M$ matrix representing the source-effect functional relationship.

In practice, the search of $\boldsymbol{p}$ in electromagnetic problems is referred to as an optimization problem. The optimized parameters $\boldsymbol{p}$ normally includes dielectric properties and dimensions of the discontinuity. In our examples, the solution of inverse problem includes permittivity, permeability, location and dimensions of the discontinuities.

5.4 MICROWAVE IMAGING EXPLOITING ADJOINT BASED SURROGATE MODELS [1]

5.4.1 Surrogate Model [21]-[24]

Most real life electromagnetic problems are solved using numerical models. These numerical models may be time and memory intensive based on the grid used and the size of the computational domain. Applying optimization to such expensive models significantly reduces the optimization problems' efficiency in terms of time and memory requirements. Surrogate modeling [21]-[24] was introduced to solve this problem. The direct optimization of an accurate but expensive model is replaced by the iterative optimization of a cheaper but only locally accurate surrogate model. This model may be a physically or mathematically derived model. It may also be updated during the optimization problems.

In this work, we choose an adjoint-based surrogate model in microwave imaging to estimate tumor's dielectric properties. The model is utilized to predict the time-domain response for linear dielectric property values. The surrogate model we propose has the form [1]

$$F_i(t,\varepsilon+\Delta\varepsilon,\sigma+\Delta\sigma)=F_i(t,\varepsilon,\sigma)+\frac{\partial F_i(t)}{\partial\varepsilon}\Delta\varepsilon+\frac{\partial F_i(t)}{\partial\sigma}\Delta\sigma \tag{5.2}$$

where $F_i(t,\varepsilon,\sigma)$ is the observed field component at the nominal values of ε and σ, and $\Delta\varepsilon$ and $\Delta\sigma$ are the perturbation in the permittivity and conductivity in the considered space region, respectively. Equation (5.2) is a simple linearized model that can be used in predicting the EM response of human tissues where relatively small changes of permittivity and conductivity take place from the normal tissues to cancerous tissues. A recent study [25] confirmed that such a small contrast indeed exists in some breast tissues.

To utilize the surrogate model (5.2), two things should be done before the optimization process. The first one is to obtain the initial field response. In a microwave imaging problem, the initial response should be the field component simulated from a structure without any cancerous tissue. We assume here that such a response is known through a good model of the healthy breast. The second thing is tumor's location and shape. This is because the derivative terms in (5.2) are changing along with location and shape. The dependency on the position and location is thus modeled through our estimated adjoint sensitivities.

5.4.2 Algorithm

Microwave imaging involves an optimization problem of the form [1]:

$$\boldsymbol{x}^*=\arg\left\{\min_{\boldsymbol{x}}\left\|\boldsymbol{F}_m-\boldsymbol{F}(\boldsymbol{x})\right\|\right\} \tag{5.3}$$

where $\boldsymbol{x}$ is the vector of optimizable parameters, $\boldsymbol{F}$ is the vector of the simulated field components, and $\boldsymbol{F_m}$ is the vector of measured field components from the receiving antennas. In the optimization process, $\boldsymbol{F}$ is normally obtained at each $\boldsymbol{x}$ using time intensive EM simulator. The optimization process will be significantly accelerated if we use the cheap but locally accurate surrogate model (5.2). The derivative terms in (5.2) is obtained using our AVM algorithm [15] as explained in Chapter 4 which can further improve the optimization efficiency. The optimization process is thus given by:

$$\boldsymbol{x}^* = \arg\left\{\min_{\boldsymbol{x}} \left\| \boldsymbol{F}(\boldsymbol{x},t) - \boldsymbol{F}_m(\boldsymbol{x},t) \right\| \right\} = \arg\left\{ \min_{\boldsymbol{x}} \sqrt{\sum_{k=1}^{N} \left(F(\boldsymbol{x},k\Delta t) - F_m(\boldsymbol{x},k\Delta t) \right)^2} \right\} \qquad (5.4)$$

where N is the maximum number of time steps and k is the index of time.

We assume that there exists an EM model of the structure (here the human breast). to use and receiving and transmitting antennas are used to transmit and receive the signals. Our algorithm of microwave imaging exploiting adjoint based surrogate models can be summarized by the following steps.

Step 1) Run TLM simulation of nominal structure (healthy breast) to get an initial field components $\boldsymbol{F_o}$.

Step 2) Run original simulation and adjont simulation of the AVM and store all the incident impulses $\boldsymbol{V}$ in (4.7) and adjoint impulses $\boldsymbol{\lambda}$ in (4.6) in the region of interest where a tumor is suspected (See Figure 5.1).

Step 3) According to the current position and shape of the tumor, the corresponding $\boldsymbol{V}$ are extracted from step 2) and the sensitivities of permittivity and conductivity are computed using (4.7). Our surrogate model is ready to use now.

Step 4) Carry out the optimization process (5.4). Stop when the termination criterion is reached.

Step 5) Go to Step 3 to estimate the gradient at the new set of parameters.

The above algorithm only optimizes the dielectric properties with known location and shape of the tumor. Now, we present another algorithm to optimize both the location and dielectric properties. Because the region where a tumor could arise is assumed to be known, we can do iteration for the location in this region. The above steps are repeated for each location and the optimized dielectric properties are stored. After all the possible locations are implemented, the one with the least objective function value will be the final optimized solution. The detailed algorithm can be summarized by the following steps.

Step 1) Run the TLM simulation of nominal structure (healthy breast) to get an initial field components $\boldsymbol{F_0}$.

Step 2) Run original simulation and adjont simulation of the AVM and store all the incident impulses $\boldsymbol{V}$ in (4.7) and adjoint impulses $\boldsymbol{\lambda}$ in (4.6) in the region of interest where a tumor is suspected (See Figure 4.2(a)).

Step 3) Repeat for all the possible N locations in the region from where the tumor could arise. According to the current position, the corresponding $\boldsymbol{V}$ are extracted from step 2 and the sensitivities with respect to permittivity and conductivity are computed using (4.7). The optimization process (5.4) is then carried out. The optimized dielectric properties at the current location are recorded. A number of N objective function values are thus obtained for different locations.

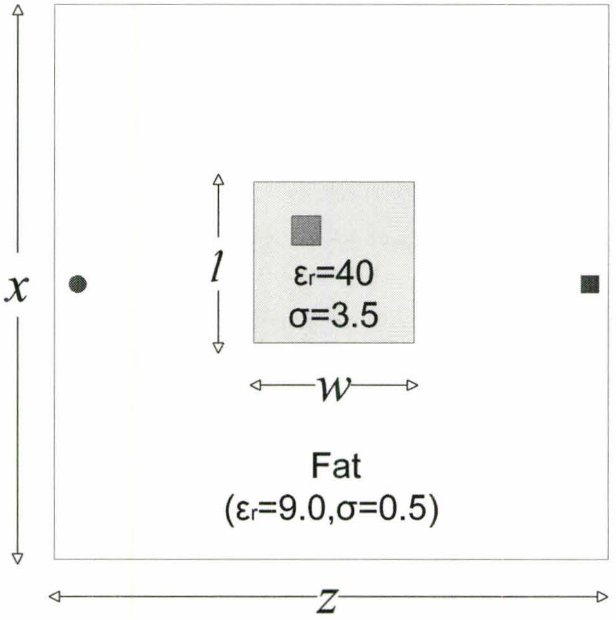

Figure 5.1: A surrogate model of human breast: the dark grey shaded area is tumor tissue; the light grey shaded area is the region of interest where a tumor could arise. The dielectric property in the region of interest is fixed $(\varepsilon_r = 40.0, \sigma = 3.5)$; the non shaded area is the fat equivalent with properties $\varepsilon_r = 9.0$ and $\sigma = 0.5$. The red circle is the excitation point and the blue square is the observation point.

Step 4) Find the pair of location and dielectric properties which gives the least objective function value among all *N* objective values. This is the final optimized solution.

5.4.3 Examples

We consider optimization of the human breast EM model shown in Figure 5.1. This structure coarsely models the human breast. The computational domain dimensions *x* and *z* are both equal to 68.0 mm. The boundaries of the computational domain are all

ABCs. The light grey shaded area is the region from which a tumor could arise and its dimensions l and w are both equal to 23.0 mm. The cell size Δl is 1.0 mm. The dielectric properties in this region are $\varepsilon_r = 40.0$ and $\sigma = 3.5$ and these properties are expected to have a relative small difference as compared with the tumor properties. The dark grey shaded area is the tumor. The unshaded area is composed of fat with dielectric properties $\varepsilon_r = 9.0$ and $\sigma = 0.5$.

The excitation is a Gaussian modulated sinusoid with a bandwidth 7.0 GHz and a center frequency f = 6.5 GHz. The maximum simulation time step is 1200. The excitation point is located at the middle point of the leftmost column and the observation point is at the middle point of the rightmost column.

5.4.3.1 Optimization of dielectric properties

Here, we first solve for only the dielectric properties of the tumor. The derivatives of the nominal structure's dielectric properties are computed. A 3% perturbation is used for the central difference (CD) approximation (4.12). The comparison between the AVM sensitivities and the CD sensitivities is shown in Figure 5.2 and Figure 5.3. Very good match is observed between the two techniques.

The optimization results are shown in TABLE 5.1. We assume that the position and shape are known. For all the positions, the size of the tumor is 6.0 mm by 6.0 mm. The permittivity and conductivity for different positioned tumors are optimized to make the simulated response match the measured response. The position listed in TABLE 5.1 is

TABLE 5.1:
OPTIMIZATION RESULTS FOR DIELECTRIC PROPERTIES

Position	Expected (ε_r, σ)	Optimized (ε_r, σ)	objective
(27 , 27)	(46 , 4.2)	(45.9 , 4.51)	0.1228
	(45 , 4.0)	(44.5 , 4.29)	0.1331
	(44 , 3.8)	(44.2 , 3.92)	0.0627
	(42 , 3.6)	(42.1 , 3.60)	0.0392
	(38 , 3.2)	(37.7 , 3.30)	0.0876
	(36 , 3.0)	(35.7 , 3.22)	0.1183
(30 , 33)	(46 , 4.2)	(45.3 , 4.54)	0.2269
	(45 , 4.0)	(44.6 , 4.25)	0.1588
	(44 , 3.8)	(43.8 , 3.97)	0.1012
	(42 , 3.6)	(42.0 , 3.64)	0.0249
	(38 , 3.2)	(37.9 , 3.24)	0.0289
	(36 , 3.0)	(35.8 , 3.18)	0.1127
(38 , 23)	(46 , 4.2)	(45.2 , 4.57)	0.2130
	(45 , 4.0)	(44.5 , 4.27)	0.1543
	(44 , 3.8)	(43.8 , 3.99)	0.1028
	(42 , 3.6)	(42.0 , 3.65)	0.0268
	(38 , 3.2)	(37.9 , 3.25)	0.0292
	(36 , 3.0)	(35.7 , 3.21)	0.1200

the coordinate of the top-left node of the tumor. The starting point for all cases is $\varepsilon_r = 42.0$ and $\sigma = 2.2$.

The optimized ε_r and expected ε_r are very close. The largest percentage error is 1.74% . For the conductivity, the largest percentage error is 8.81% .

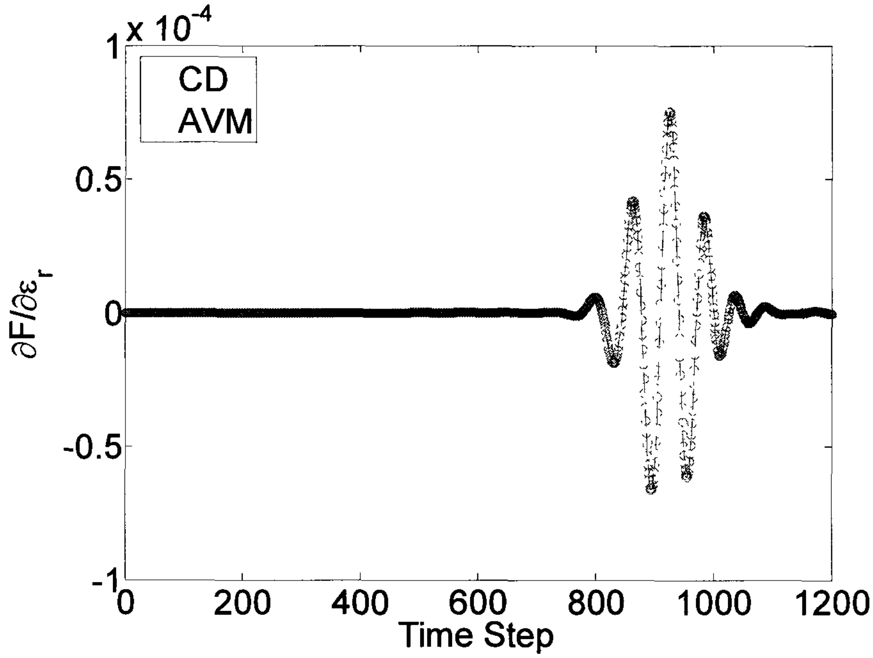

Figure 5.2: The objective function sensitivity, $\partial \boldsymbol{F} / \partial \varepsilon_r$.

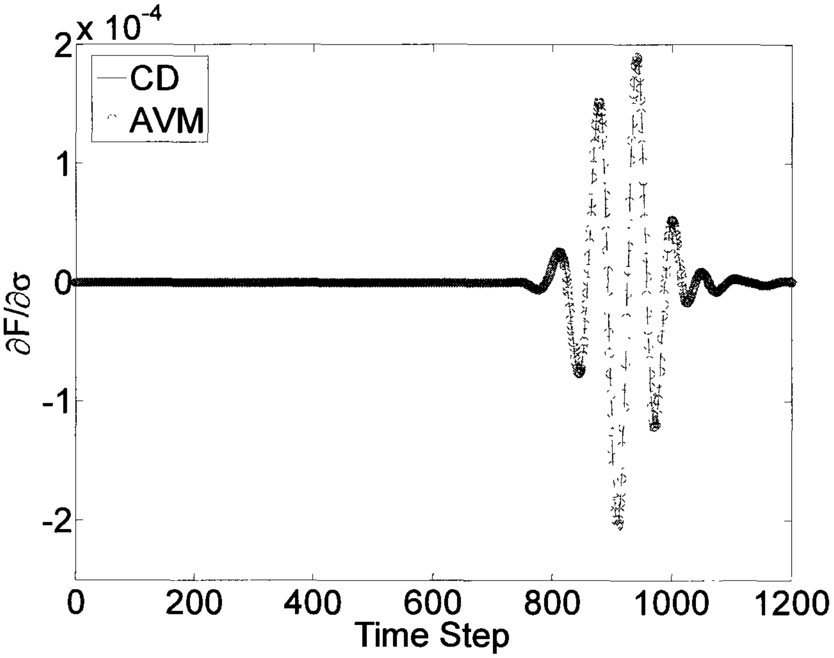

Figure 5.3: The objective function sensitivity, $\partial \boldsymbol{F} / \partial \sigma$.

TABLE 5.2:
OPTIMIZATION RESULTS FOR DIELECTRIC PROPERTIES AND LOCATION

Expected			Optimized			
ε_r	σ	Position	ε_r	σ	Position	Objetive
45.0	4.00	(27, 27)	43.8	4.36	(39, 27)	0.0950
43.5	3.75	(27, 27)	42.9	3.97	(25, 27)	0.0627
42.0	3.60	(27, 27)	41.9	3.68	(26, 27)	0.0231
40.5	3.55	(27, 27)	40.5	3.55	(27, 27)	0.0015
38.0	3.20	(27, 27)	38.4	3.15	(27, 34)	0.0182

5.4.3.2 Optimization of dielectric properties and location

The optimization parameters include the dielectric properties and location of the tumor. The iteration step of the location is 1.0 mm. Because the region of interest is 23.0 mm by 23.0 mm and the dimensions of tumor are 6.0 mm by 6.0 mm, there are $(23-6)\times(23-6)=289$ possible tumor locations. The utilized derivatives with respect to tumor's dielectric properties at each location are computed the same way as the previous example.

The optimization results are shown in TABLE 5.2. The starting point of dielectric properties at each location is $\varepsilon_r = 42.0$ and $\sigma = 2.2$. The optimized ε_r and expected ε_r are very close. The largest percentage error is 2.67%. For the conductivity, the largest percentage error is 9.0%. There are two cases that the positions are estimated wrong. For the rest of three cases, the positions are estimated within 2.0 mm error.

5.5 TUMOR DETECTION USING DIRECT OPTIMIZATION [16]

5.5.1 Introduction

Section 5.4 presented a novel approach for efficient microwave imaging exploiting adjoint based surrogate models. However, this approach has some limitations: (1) a locally linear relation between normal tissue's dielectric properties and cancerous tissue's dielectric properties, and (2) assumption of the known shape of the tumor. In this section, we will realize 2-D and 3-D tumor detection using gradient-based optimization where the time-domain response gradients are obtained using the AVM in [15]. Although we use direct optimization of the expensive actual EM models of human breast, the way we compute the response derivatives is much faster and the optimization efficiency is improved a lot.

5.5.2 Algorithm

Microwave imaging uses measured data to determine the dielectric properties, location and size of tumors within the human breast. Therefore, the optimization process can be expressed in the form of

$$\boldsymbol{x}^* = \arg\left\{ \min_{\boldsymbol{x}} \max_{f} \left(\boldsymbol{f}(\boldsymbol{x}) \right) \right\}, f_k(\boldsymbol{x}) = \left(F_{m,k} - F_k(\boldsymbol{x}) \right)^2 \tag{5.5}$$

where $\boldsymbol{x}$ is the vector of dielectric properties, shape and position parameters and $\boldsymbol{f}(\boldsymbol{x})$ is the objective function. The function $\boldsymbol{f}(\boldsymbol{x})$ is a vector with k^{th} element $f_k(\boldsymbol{x})$ equal to the squared difference between measured field $F_{m,k}$ and simulated field F_k at k^{th} time step. (5.5) is an optimization problem which finds values of $\boldsymbol{x}$ that minimize the maximum value of $\boldsymbol{f}(\boldsymbol{x})$ and stops the simulation when the maximum of the function values evaluated at the solution $\boldsymbol{x}$ reaches user-defined criteria.

The optimizable parameters for tumor detection normally include dielectric properties, dimensions and location. The dielectric properties are continuous parameters, so there is no problem for optimizing these parameters using (5.5) in a MATLAB optimization toolbox [26]. However, this is not the case for position and dimensions. It is because we simulate the structure using TLM [27], [28] which discretizes computation domain into a network of transmission lines. A square cell of mesh size $\Delta l = 1.0$ mm is utilized in our examples, so the position coordinates and dimensions must be integer multiples of the cell size. To address this issue, we introduce interpolation into the optimization process [15]. We round the optimizer's solutions and pass those to the EM simulator. The actual response at the current optimization iteration is approximated using the linear model (5.6). The derivatives sent to the optimizer are also generated at rounded parameters. The optimization process is shown in Figure 5.4.

$$\boldsymbol{f}(\boldsymbol{p}) = \boldsymbol{f}(\boldsymbol{p}') + \frac{\partial \boldsymbol{f}}{\partial \boldsymbol{p}'}^{T}(\boldsymbol{p} - \boldsymbol{p}'), \boldsymbol{p}' = round(\boldsymbol{p}) \tag{5.6}$$

where $\boldsymbol{p}$ is the vector of dimension and position parameters.

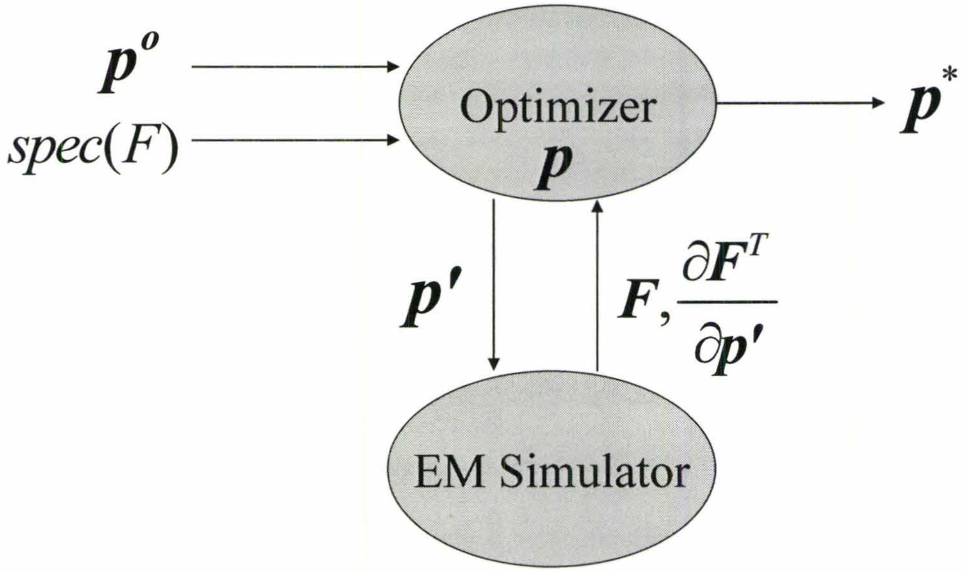

$$\boldsymbol{p}' = \left[\varepsilon_r, \sigma, round(z), round(x), round(a), round(b)\right]$$

$$\boldsymbol{F} = \boldsymbol{F}(p') + (z - round(z))\left.\frac{\partial \boldsymbol{F}^{T}}{\partial z}\right|_{round(z)} + (x - round(x))\left.\frac{\partial \boldsymbol{F}^{T}}{\partial x}\right|_{round(x)} \cdots$$
$$+ (a - round(a))\left.\frac{\partial \boldsymbol{F}^{T}}{\partial a}\right|_{round(a)} + (b - round(b))\left.\frac{\partial \boldsymbol{F}^{T}}{\partial b}\right|_{round(b)}$$

Figure 5.4: The optimization process involving interpolation. $\boldsymbol{p}$ is the actual optimizer solution, $\boldsymbol{p}'$ is the rounded $\boldsymbol{p}$ and $\boldsymbol{F}$ is the approximated response at $\boldsymbol{p}$. The derivatives sent to the optimizer $\partial \boldsymbol{F}^{T} / \partial \boldsymbol{p}'$ are the sensitivities at rounded parameters $\boldsymbol{p}'$.

5.5.3 Example: 2-D Tumor Detection

We consider the optimization of the human breast EM model shown in Figure 5.5. The computational domain is a 76 mm by 76 mm square. The boundaries of the computational domain are all Absorbing Boundary Conditions (ABC). The non shaded

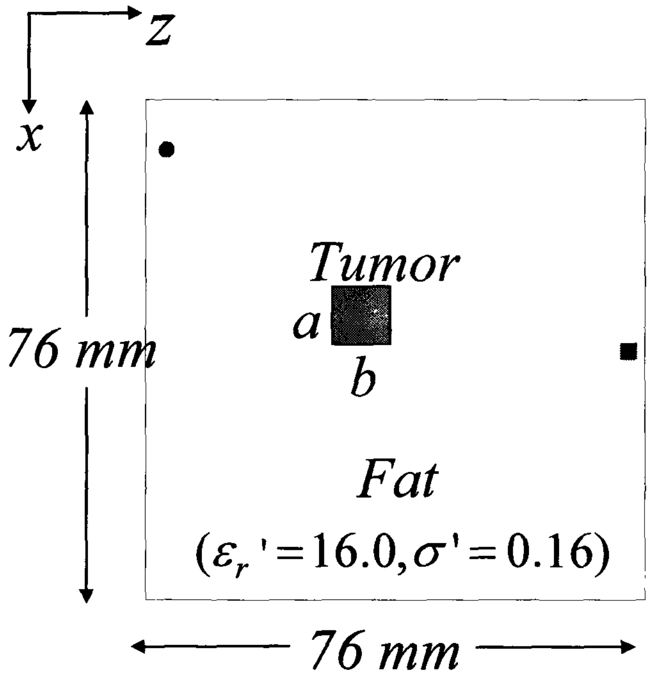

Figure 5.5: A model of human breast: the dark grey shaded area is tumor tissue; the non shaded area is the fat equivalent with properties $\varepsilon_r^{'}=16.0, \sigma^{'}=0.16$. The red circle is the excitation point (1, 5) and the blue square is the observation point (76, 38).

region is composed of fat with $\varepsilon_r=16.0$ and $\sigma=0.16$. The dark grey shaded area is the tumor. The excitation is a Gaussian modulated sinusoidal wave with a bandwidth 7.0 GHz and a center frequency f = 6.5 GHz. The excitation point is $(z,x)=(1,5)$ which is the middle point on the leftmost column and the observation point is $(z,x)=(76,38)$ the middle point on the rightmost column.

We optimize the parameter in three cases (1) optimization of location only, (2) optimization of dielectric properties and location, and (3) optimization of dielectric properties, location and dimensions. In case (1), the dimensions and dielectric properties of the tumor are assumed as 10 mm by 10 mm, and $\varepsilon_r = 57.2$ and $\sigma = 1.08$, respectively. In case (2), only the dimensions of the tumor are assumed to be known and are equal to 10 mm by 10 mm. Every parameter is unknown in the last case.

The optimization results are shown in TABLE 5.3. The position we listed in TABLE III is the coordinate of the top-left node of the tumor. The starting point of parameters is $(\varepsilon_r, \sigma, z, x, a, b) = (50, 1.5, 30, 30, 15, 15)$. The optimized dielectric properties and expected dielectric properties are very close. The largest error of position is 1.9 mm. For dimension, the largest error is 0.75mm. The dielectric properties have relative large error and it is because this structure is less sensitivity to them.

TABLE 5.3:
OPTIMIZATION RESULTS OF DIRECT OPTIMIZATION

Case #	Expected	Optimized
1-position	$(z,x)=(15,35)$	$(z,x)=(14.5,34.1)$
2-position and dielectric properties	$(z,x)=(15,35)$ $(\varepsilon_r,\sigma)=(57.2,1.08)$	$(z,x)=(15.50,35.07)$ $(\varepsilon_r,\sigma)=(57.20,1.47)$
3-position, dielectric properties and dimensions	$(z,x)=(15,35)$ $(a,b)=(10,10)$ $(\varepsilon_r,\sigma)=(57.2,1.08)$	$(z,x)=(13.1,33.4)$ $(a,b)=(9.25,9.52)$ $(\varepsilon_r,\sigma)=(68,1.51)$

5.6 CONCLUSIONS

In this chapter, the applications of the AVM technique for inverse problems were demonstrated. Gradient-based algorithm was chosen for EM optimization problems. The optimization process speeds up by using our AVM to calculate the gradients. The 2-D breast tumor detection using surrogate models was first presented. Direct optimization of the 2-D breast structure was implemented as well. Good results were obtained for all the optimized parameters of dielectric properties, dimensions and location.

REFERENCES

[1] M.H. Bakr, P. Zhao, and N.K. Nikolova, "Microwave imaging exploiting adjoint based surrogate models," *IEEE Trans. ACES*, 2008.

[2] Wikipedia (March 14, 2008). Networks. [online]. Available: http://en.wikipedia.org/wiki/Breast_cancer.

[3] B. Bocquet, J.C. van de Velde, A. Mamouni, Y. Leroy, G. Giaux, J. Delannoy, and D. Del Valee, "Microwave radiometric imaging at 3 GHz for the exploration of breast tumors," *IEEE Trans. Microwave Theory Tech.*, vol. 38, pp. 791-793, June 1990.

[4] S. Mouty, B. Bocquet, R. Ringot, N. Rocourt, and P. Devos, "Microwave radiometric imaging for the characterisation of breast tumors," *Eur. Phys. J.: Appl. Phys.*, vol. 10, pp. 73-78, 2000.

[5] K.L. Carr, "Microwave radiometry: its importance to the detection of cancer," *IEEE Trans. Microwave Theory Tech.*, vol. 37, pp. 1862-1869, Dec. 1989.

[6] K.L. Carr, P. Cevasco, P. Dunlea, and J. Shaeffer, "Radiometric sensing: An adjuvant to mammography to determine breast biopsy," in *IEEE MTT-S Int. Microwave Symp. Dig.*, vol. 2, pp. 929-932, 2000.

[7] R.A. Kruger, K.K. Kopecky, A.M Aisen, D.R. Reinecke, G.A. Kruger, and W.L. Kiser, Jr., "Thermoacoustic CT with radio waves: A medical imaging paradigm," *Radiology*, vol. 211, pp. 275-278, 1999.

[8] R.A. Kruger, W.L. Kiser, Jr., D.R. Reinecke, G.A Kruger, and R.L. Eisenhart, "Thermoacoustic computed tomography of the breast at 434 MHz", in *IEEE MTT-S Int. Microwave Symp. Dig.*, vol. 2, pp. 591-594, 1999.

[9] L.V. Wang, X. Zho, H. Sun, and G. Ku, "Microwave-induced acoustic imaging of biological tissues," *Rev. Sci. Instrum.*, vol. 70, pp. 3744-3748, 1999.

[10] G. Ku and L.V. Wang, "Scanning thermoacoustic tomography in biological tissue," *Med. Phys.*, vol. 27, pp. 1195-1202, 2000.

[11] E.C. Fear, S.C. Hagness, P.M. Meaney, M. Okoniewski, and M.A. Stuchly, "Enhancing breast tumor detection with near-field imaging," *IEEE Microwave Magazine.*, pp. 48-56, March 2002.

[12] S. P. Poplack, P. M. Meaney, A. Hartov, K. D. Paulsen, T. D. Torsteson, M. R. Grove, S. K. Soho, and W.A. Wells, "Electromagnetic breast imaging: Average tissue property value in women with negative clinical findings," *Radiol.*, vol. 231, no. 2, pp. 571-580, May 2004.

[13] X. Li, S. K. Davis, S. C. Hagness, D. W. Weide, and B. D. Van Veen, "Microwave imaging via space–time beamforming: experimental investigation of tumor detection in multilayer breast phantoms," *IEEE Trans. Microwave Theory Tech.*, vol. 52, pp. 1856-1865, Aug. 2004.

[14] E. C. Fear and M. A. Stuchly, "Microwave detection of breast cancer," *IEEE Trans. Microwave Theory Tech.*, vol. 48, no. 11, pp. 1854-1863, 2000.

[15] M.H. Bakr, P. Zhao, and N.K. Nikolova, "Adjoint First Order sensitivities of time domain responses and their applications in the solution of inverse problems," *IEEE Trans. AP*, submitted.

[16] S. S. Chaudhary, R. K. Mishra, A. Swarup, and J. M. Thomas, "Dielectric properties of normal and malignant human breast tissues at radiowave and microwave frequencies," *Indian J. Biochem. Biophys.*, vol. 21, pp. 76–79, Feb. 1984.

[17] S. Gabriel, R. W. Lau, and C. Gabriel, "The dielectric properties of biological tissues: II. Measurements on the frequency range 10 Hz to 20 GHz," *Phys. Med., Biol.*, vol. 41, no. 11, pp. 2251-2269, Nov. 1996.

[18] N.V. Korovkin, V.L. Chechurin, and M. Hayakawa, *Inverse Problems in Electric Circuits and Electromagnetics*. Springer US, ISBN: 978-0-387-46047-5, 2007.

[19] E.B. Curtis and J.A. Morrow, "Inverse problems for electrical networks," *NY: World Scientific Publishing Co.*, Singapore, 2000.

[20] P. Neittaanmaki, M. Rudnicki, and A. Savini, "Inverse problems and optimal design in electricity and magnetism," *Oxford: Claredon Press*, 1996.

[21] M.H. Bakr, J.W. Bandler, K. Madsen, J.E. Rayas-Sánchez, and J. Søndergaard, "Space mapping optimization of microwave circuits exploiting surrogate models," *IEEE Trans. Microwave Theory Tech.*, vol. 48, pp. 2297-2306, 2000.

[22] J.W. Bandler and K. Madsen, "Use of surrogate models in engineering design," Workshop on Numerical Optimization and Approximation, Institute of Mathematics, Lulea Technical University, Sweden, Sept. 1999.

[23] J.W. Bandler, Q.S. Cheng, D.H. Gebre-Mariam, K. Madsen, F. Pedersen, and J. Søndergaard, "EM-based surrogate modeling and design exploiting implicit, frequency and output space mappings," *IEEE MTT-S Int. Microwave Symp. Digest* (Philadelphia, PA, June 2003), pp. 1003-1006.

[24] J.W. Bandler, Q.S. Cheng, S.A. Dakroury, D.M. Hailu, K. Madsen, A.S. Mohamed, and F. Pedersen, "Space mapping interpolating surrogates for highly optimized EM-based design of microwave devices," *IEEE MTT-S Int. Microwave Symp. Dig.*, (Fort Worth, TX), pp. 1565-1568, 2004.

[25] M. Lazebnik, C.B. Watkins, S.C. Hagness, J.H. Booske, D. Popovic, L. McCartney, M. Okoniewski, M.J. Lindstrom, T.M. Breslin, J. Harter, S. Sewall, W. Temple, D. Mew, A. Magliocco, and T. Ogilvie, "The dielectric properties of normal and malignant breast tissue at microwave frequencies: analysis, conclusions, and implications from the Wisconsin/Calgary study," *IEEE Antennas Propagat. Symposium Digest*, pp. 2172-2175, 2007.

[26] Matlab^{TM}, 2004, Version 7.0.1

[27] P.B. Johns and R.L. Beurle, "Numerical modeling of 2-dimensional scattering problems using a transmission line matrix," *Proceedings of IEE*, vol. 118, no. 9, pp. 1203-1208, Sept. 1971.

[28] W.J.R. Hoefer, "The transmission-line matrix method-theory and applications," *IEEE Trans. Microwave Theory Tech.*, vol. MTT-33, pp.882-893, Oct. 1985.

CHAPTER 6

CONCLUSIONS

This literature mainly discussed the novel algorithm for sensitivity estimation of time-domain response using the Adjoint Variable Method (AVM) with time-domain transmission-line modeling (TLM). This algorithm efficiently estimates the objective function sensitivities with respect to all the parameters using only two simulations.

Chapter 2 reviewed the basic theory of the time-domain TLM method for both the 2-D TLM and the 3-D TLM with symmetric condensed nodes (SCN). In each case, we discussed how the variations of dielectric properties and lossy materials are modeled. The boundary modeling of the non-dispersive case and the dispersive case were briefly introduced. For dispersive boundaries, Johns matrix and absorbing boundary conditions implemented by one-way wave equations were presented.

Chapter 3 reviewed up-to-date AVM developments for EM numerical method: time-domain TLM. We presented the AVM algorithm for both 2-D time-domain TLM and 3-D TLM with SCN. The sensitivity analysis for perfectly conducting discontinuities and dielectric discontinuities were demonstrated. In all the cases, an original simulation and an adjoint simulation are implemented. Only a few links related to optimized parameters are stored in both the original and adjoint system. The sensitivities with respect to all the optimized parameters are calculated using these two simulations. We also reviewed some further developments of the AVM, such as the adjoint-free S-parameter sensitivity analysis for lossless homogeneous and nonhomogeneous TLM problems, sensitivities of planar structures using first-order one-way wave equation boundaries, and AVM for conformal TLM based on the rubber cell implementation.

Chapter 4 addressed our novel AVM algorithm for estimating the sensitivities of time-domain response with respect to all designable parameters. The algorithm of both 2-D TLM and 3-D TLM was presented. The sensitivities with respect to all the optimized parameters are calculated using two simulations of original system and adjoint system. Only a few links related to optimized parameters are stored in each system. A special algorithm was developed for determination of adjonit impulses and it induces a lot saving of time and memory space requirement. The approach was illustrated through metallic discontinuities and dielectric discontinuities. The results were compared to the expensive center difference approximation. The performance of good accuracy and high efficiency was obtained.

Chapter 5 demonstrated the applications of the AVM technique for inverse problems. Gradient-based algorithm is chosen for EM optimization problems. The optimization process speeds up by using our AVM to calculate the gradient. 2-D breast tumor detection using surrogate models was first presented. Direct optimization of 2-D breast structure was implemented as well. The optimized parameters for all the cases included dielectric properties, dimensions and location.

Further research will lead to the following future developments:

1. Developing adjoint sensitivities of time-domain response for structures with dispersive boundaries.
2. Developing adjoint sensitivities of time-domain response for resonant structures.
3. Developing adjoint sensitivities of time-domain response for metamaterials.
4. Developing an AVM algorithm for higher order sensitivities of time domain responses.